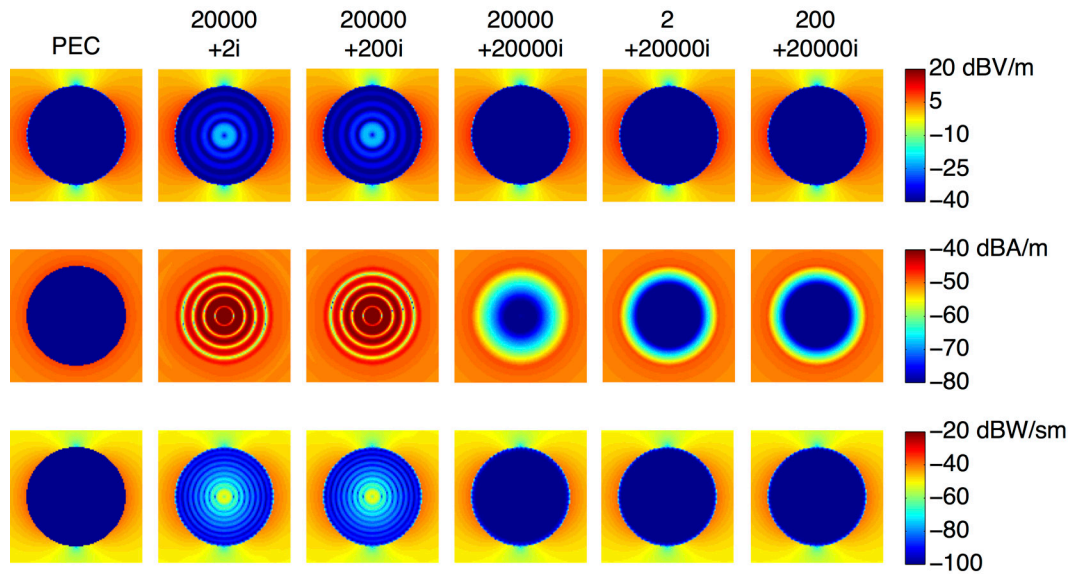
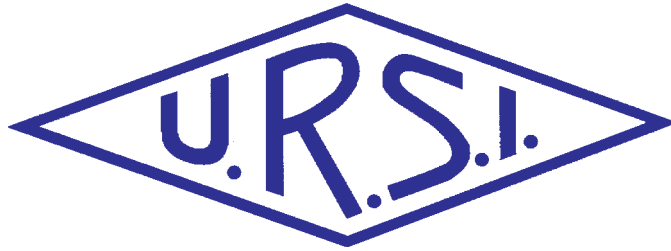


INTERNATIONAL
UNION OF
RADIO SCIENCE

UNION
RADIO-SCIENTIFIQUE
INTERNATIONALE



Vol. 2018, No. 365
June 2018

Contents

Radio Science Bulletin Staff	3
URSI Officers and Secretariat.....	6
Editor's Comments	8
Mitigation of Non-Narrowband Radio-Frequency Interference	10
Determining All Ambiguities in Direction of Arrival Measured By Radar Systems	20
Design of a Narrow-band Single-Layer Chipless RFID Tag	29
Metamaterials 2019.....	36
Et Cetera	37
Book Review	38
Correction	40
Ethically Speaking	41
Solution Box.....	43
European School of Antennas	48
Telecommunications Health and Safety	49
Women in Radio Science	52
EMTS 2019	54
URSI Conference Calendar.....	55
Information for Authors.....	57
Become An Individual Member of URSI.....	58

Cover Picture: The solutions of the scattering problems (SOLBOX-12) involving spheres with positive values for the real part of the relative permittivity (values are shown on the top) at 10 THz. The electric-field intensity (first row), the magnetic-field intensity (second row), and the power density (third row) were plotted in the vicinity of the spheres. See the article in the Solution Box column by Hande İbili, Barışcan Karaosmanoğlu, and Özgür Ergül (pp. 44-48)

The International Union of Radio Science (URSI) is a foundation Union (1919) of the International Council of Scientific Unions as direct and immediate successor of the Commission Internationale de Télégraphie Sans Fil which dates from 1914.

Unless marked otherwise, all material in this issue is under copyright © 2017 by Radio Science Press, Belgium, acting as agent and trustee for the International Union of Radio Science (URSI). All rights reserved. Radio science researchers and instructors are permitted to copy, for non-commercial use without fee and with credit to the source, material covered by such (URSI) copyright. Permission to use author-copyrighted material must be obtained from the authors concerned.

The articles published in the Radio Science Bulletin reflect the authors' opinions and are published as presented. Their inclusion in this publication does not necessarily constitute endorsement by the publisher.

Neither URSI, nor Radio Science Press, nor its contributors accept liability for errors or consequential damages.

Radio Science Bulletin Staff

Editor

W. R. Stone
Stoneware Limited
840 Armada Terrace
San Diego, CA 92106, USA
Tel: +1-619 222 1915, Fax: +1-619 222 1606
E-mail: r.stone@ieee.org

Editor-in-Chief

P. Van Daele
URSI Secretariat
Ghent University - INTEC
Technologiepark - Zwijnaarde 15
B-9052 Gent
BELGIUM
Tel: +32 9-264 33 20, Fax: +32 9-264 42 88
E-mail: Pet.VanDaele@UGent.be

Production Editor

I. Lievens
URSI Secretariat / Ghent University - INTEC
Technologiepark - Zwijnaarde 15
B-9052 Gent, BELGIUM
Tel: +32 9-264.33.20, Fax: +32 9-264.42.88
E-mail: ingeursi@ugent.be, info@ursi.org

Senior Associate Editors

A. Pellinen-Wannberg
Department of Physics
Umea University
BOX 812
SE-90187 Umea, SWEDEN
Tel: +46 90 786 74 92, Fax: +46 90 786 66 76
E-mail: asta.pellinen-wannberg@umu.se

O. Santolik
Institute of Atmospheric Physics
Academy of Sciences of the Czech Republic
Bocni II
1401, 141 31 Prague 4, CZECH REPUBLIC
Tel: +420 267 103 083, Fax +420 272 762 528
E-mail os@ufa.cas.cz, santolik@gmail.com

Associate Editors, Commissions

Commission A

Nuno Borges Carvalho
Instituto de Telecomunicações
Universidade de Aveiro, Campus Universitario
3810-193 Aveiro, Portugal
Tel: +351 234377900, Fax: +351 234377901
E-mail: nbcarvalho@ua.pt

Tian Hong Loh
National Physical Laboratory
Hampton Road
Teddington TW11 0LW, United Kingdom
Tel: +44 020 8943 6508
E-mail: tian.loh@npl.co.uk

Pedro Miguel Cruz
Rua Sao Sebastiao
n34 Hab 33
4520-250 Santa Maria da Feira, Aveiro, PORTUGAL
Tel: +351 225898410
E-mail: pedro.cruz@controlar.pt

Nosherwan Shoaib
School of Electrical Engineering and Computer Science (SEECS)
National University of Sciences and Technology (NUST)
NUST Campus H-12, Islamabad, Pakistan
Tel: 051 90852561
E-mail: nosherwan.shoaib@seecs.edu.pk

Commission B

Andrea Michel

Department of Information Engineering
Università di Pisa
Pisa, Italy
E-mail: andrea.michel@iet.unipi.it

John Volakis

College of Engineering and Computing
Florida International University
10555 W. Flagler Street, EC2477
Miami, FL 33174, USA
Tel: +1 305 348 2807
E-mail: jvolakis@fiu.edu

Commission C

Yves Louet

CS 47601, SUPELEC
Avenue de Boulaie
F-35576 Cesson-Sévigné, France
Tel: +33 2 99 84 45 34, Fax: +33 2 99 84 45 99
E-mail: yves.louet@supelec.fr

Commission D

Naoki Shinohara

RISH
Kyoto University
Uji 611-0011, Japan
Tel: +81 774 38 3807 Fax: +81 774 31 8463
E-mail: shino@rish.kyoto-u.ac.jp

Commission E

Virginie Deniau

IFSTTAR
20. rue Elisée Reclus BP 70317
F-59666 Villeneuve d'Ascq Cedex, France
Tel: +33 03 20438991
E-mail: virginie.deniau@ifsttar.fr

Commission F

Haonan Chen

Earth System Research lab, Physical Sciences Division
NOAA
325 Broadway, Boulder, CO 80305, USA
Tel: +1 303 497 4616
E-mail: haonan.chen@noaa.gov

Tullio Tanzi

Télécom ParisTech - LabSoC, c/o EURECOM
Campus SophiaTech Les Templiers
450 route des Chappes 06410 Biot, FRANCE
Tel: +33 0 4 93008411, Fax: 33 0 493008200
E-mail: tullio.tanzi@telecom-paristech.fr

Commission G

Giorgiana De Franceschi

Dept. Arenonomy, Istituto Nazionale di Geofisica e
Vulcanology
Via di Vigna, Murata 605
00 143 Roma, Italy
Tel: +39 06 51860307, Fax: +39 06 51860397
E-mail: giorgiana.defranceschi@ingv.it

Commission H

Jyrki Manninen

Sodankylä Geophysical Observatory
Tähteläntie 62
FIN-99600 Sodankylä, Finland
Tel: +358 400 151503, Fax +358 16 610248
E-mail: Jyrki.Manninen@oulo.fi

Commission J

Jacob W. Baars

Max Planck Institute for Radio Astronomy
Auf dem Hügel 69
53121 Bonn, Germany
Tel: +49 228 525303
E-mail: jacobbaars@arcor.de

Commission K

Kensuke Sasaki

Applied EM Research Institute
NICT
Koganei, Tokyo, Japan
E-mail: k_sasaki@nict.go.jp

Associate Editors, Columns

Book Reviews

G. Trichopoulos

Electrical, Computer & Energy Engineering ISTB4 555D
Arizona State University
781 E Terrace Road, Tempe, AZ, 85287 USA
Tel: +1 (614) 364-2090
E-mail: gtrichop@asu.edu

Solution Box

Ö. Ergül

Department of Electrical and Electronics Engineering
Middle East Technical University
TR-06800, Ankara, Turkey
E-mail: ozgur.ergul@eee.metu.edu.tr

Historical Papers

J. D. Mathews

Communications and Space Sciences Lab (CSSL)
The Pennsylvania State University
323A, EE East
University Park, PA 16802-2707, USA
Tel: +1(814) 777-5875, Fax: +1 814 863 8457
E-mail: JDMathews@psu.edu

Telecommunications Health & Safety

J. C. Lin

University of Illinois at Chicago
851 South Morgan Street, M/C 154
Chicago, IL 60607-7053 USA
Tel: +1 312 413 1052, Fax: +1 312 996 6465
E-mail: lin@uic.edu

Et Cetera

T. Akgül

Dept. of Electronics and Communications Engineering
Telecommunications Division
Istanbul Technical University
80626 Maslak Istanbul, TURKEY
Tel: +90 212 285 3605, Fax: +90 212 285 3565
E-mail: tayfunakgul@itu.edu.tr

Historical Column

G. Pelosi

Department of Information Engineering
University of Florence
Via di S. Marta, 3, 50139 Florence, Italy
E-mail: giuseppe.pelosi@unifi.it

Women in Radio Science

A. Pellinen-Wannberg

Department of Physics and Swedish Institute of Space
Physics
Umeå University
S-90187 Umeå, Sweden
Tel: +46 90 786 7492
E-mail: asta.pellinen-wannberg@umu.se

Early Career Representative Column

S. J. Wijnholds

Netherlands Institute for Radio Astronomy
Oude Hoogeveensedijk 4
7991 PD Dwingeloo, The Netherlands
E-mail: wijnholds@astron.nl

Ethically Speaking

R. L. Haupt

Colorado School of Mines
Brown Building 249
1510 Illinois Street, Golden, CO 80401 USA
Tel: +1 (303) 273 3721
E-mail: rhaupt@mines.edu

Education Column

Madhu Chandra

Microwave Engineering and Electromagnetic Theory
Technische Universität Chemnitz
Reichenhainerstrasse 70
09126 Germany
E-mail: madhu.chandra@etit.tu-chemnitz.de

A. J. Shockley

E-mail: aj4317@gmail.com

URSI Officers and Secretariat

Current Officers triennium 2017-2020



President

M. Ando

Senior Executive Director
National Institute of Technology
701-2, Higashi Asakawa, Hachioji,
Tokyo 193-0834, Japan
Tel: +81-42-662-3123,
Fax: +81-42-662-3131
E-mail: ando@kosen-k.go.jp,
mando@antenna.ee.titech.ac.jp



Vice President

O. Santolik

Institute of Atmospheric Physics
Electrical Eng. Dept
Academy of Sciences of the Czech Republic
Bocni II, 1401
141 31 Prague 4, CZECH REPUBLIC
Tel: +420 267 103 083
Fax: 420 272 762 528
E-mail: os@ufa.cas.cz, santolik@gmail.com



Past President

P. S. Cannon

Gisbert Kapp Building
University of Birmingham
Edgbaston, Birmingham, B15 2TT,
UNITED KINGDOM
Tel: +44 (0) 7990 564772
Fax: +44 (0)121 414 4323
E-mail: p.cannon@bham.ac.uk



Vice President

A. Sihvola

Electronic Science Department
Aalto University
School of Electrical Engineering
PO Box 13000
FI-00076 AALTO
FINLAND
Tel: +358 50 5871286
E-mail: Ari.Sihvola@aalto.fi



Secretary General

P. Van Daele

URSI Secretariat
Ghent University - INTEC
Technologiepark - Zwijnaarde 15
B-9052 Gent
BELGIUM
Tel: +32 9-264 33 20
Fax: +32 9-264 42 88
E-mail: Pet.VanDaele@UGent.be



Vice President

P. L. E. Uslenghi

Dept. of ECE (MC 154)
University of Illinois at Chicago 851
S. Morgan Street
Chicago, IL 60607-7053
USA
Tel: +1 312 996-6059
Fax: +1 312 996 8664
E-mail: uslenghi@uic.edu



Vice President

W. Baan

Astron
Asserweg 45
9411 LP Beilen
THE NETHERLANDS
Tel: +31 521-595 773/100
Fax: +31 521-595 101
E-mail: baan@astron.nl

URSI Secretariat



Secretary General

P. Van Daele
URSI Secretariat
Ghent University - INTEC
Technologiepark - Zwijnaarde 15
B-9052 Gent
BELGIUM
Tel: +32 9-264 33 20
Fax: +32 9-264 42 88
E-mail: Pet.VanDaele@UGent.be



Assistant Secretary General AP-RASC

K. Kobayashi
Dept. of Electr and Commun. Eng.,
Chuo University
1-13-27 Kasuga, Bunkyo-ku
Tokyo, 112-8551, JAPAN
Tel: +81 3 3817 1846/69
Fax: +81 3 3817 1847
E-mail: kazuya@tamacc.chuo-u.ac.jp



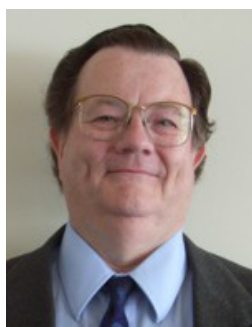
Assistant Secretary General

Stefan J. Wijnholds
Netherlands Institute for
Radio Astronomy
Oude Hoogeveensedijk 4
7991 PD Dwingeloo
The Netherlands
E-mail: wijnholds@astron.nl



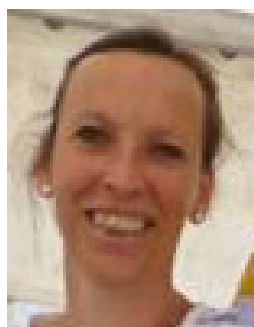
Executive Secretary

I. Heleu
URSI Secretariat
Ghent University - INTEC
Technologiepark - Zwijnaarde 15
B-9052 Gent
BELGIUM
Tel. +32 9-264.33.20
Fax +32 9-264.42.88
E-mail info@ursi.org



Assistant Secretary General Publications & GASS

W. R. Stone
840 Armada Terrace
San Diego, CA 92106
USA
Tel: +1-619 222 1915
Fax: +1-619 222 1606
E-mail: r.stone@iecc.org



Administrative Secretary

I. Lievens
URSI Secretariat
Ghent University - INTEC
Technologiepark - Zwijnaarde 15
B-9052 Gent
BELGIUM
Tel: +32 9-264.33.20
Fax: +32 9-264.42.88
E-mail: ingeursi@ugent.be



W. Ross Stone

Stoneware Limited
840 Armada Terrace
San Diego, CA 92106, USA
Tel: +1-619 222 1915, Fax: +1-619 222 1606
E-mail: r.stone@ieee.org

Special Issue: Papers From the AT-RASC Student Paper Competition

In this issue, we have three papers from the Student Paper Competition that was part of the 2nd URSI Atlantic Radio Science Conference (AT-RASC 2018), held May 28-June 1, 2018, in Gran Canaria, Spain.

Jan-Willem Steeb won first place in the Student Paper Contest. His paper, by Jan-Willem Steeb, David Davidson, and Stefan Wijnholds, presents two methods for mitigating the effects of non-narrowband radio-frequency interference on radio-astronomy observations. Both methods involve algorithms for doing subspace subtraction of the interference based on models that take into account the non-narrowband characteristics of the interference. The first model is a flat-frequency-response model, while the second uses Zatman's approximation (based on two frequency-shifted monochromatic sources). The algorithms were evaluated using data from the Low-Frequency Array (LOFAR). The results showed significant mitigation with both algorithms, although one was computationally faster than the other.

Daniel Kastinen won third place in the Student Paper Contest. His paper presents a solution to resolving the ambiguity problem that occurs when a radar system is used to determine the position and motion of objects. The ambiguity occurs in determining the direction of arrival of the electromagnetic wave from the target, which can produce the same response in the radar system for waves arriving from different directions. The author develops a mathematical framework and a practical method for finding all ambiguities in any multi-channel radar. This led to the discovery of noise-induced ambiguities in theoretically ambiguity-free radars. It is shown how to use the gain patterns of the radar sensors to resolve ambiguities. The original motivation for this work was to resolve ambiguous meteor trajectories in data from the Middle and Upper

Atmosphere Radar in Shigaraki, Japan. That radar is used in examples throughout the paper. However, the results are quite general and should apply to any radar system.

Ricardo Figueiredo was one of the finalists in the Student Paper Contest. His paper, by Ricardo Figueiredo, João Louro, Samuel Pereira, João Gonçalves, and Nuno Borges Carvalho, presents a design for a single-layer chipless RFID (radio-frequency identification) tag that operates in a narrow bandwidth. The device uses a coplanar stripline design and has the ability to encode three bits of information. The paper begins with an overview of RFID device design and operation. The detailed design and simulation of the chipless device is presented. The design uses multiple C-shaped sections of stripline on a single-layer device to produce multiple resonances. Designs for one-, two-, and three-bit tags are presented for operation centered around 950 MHz. Several devices were built and tested, demonstrating the efficacy of the design.

Our Other Contributions

In his book review column, George Trichopoulos brings us a review by Jacob Baars. The book, *Four Pillars of Radio Astronomy: Mills, Christiansen, Wild, Bracewell*, traces the careers of four leaders in radio astronomy from Australia. I think you'll find the review fascinating, and it definitely made me want to read the book.

You need to take a look at Tayfun Akgül's Et Cetera column. It will brighten your day. Tayfun had an exhibition of "Cartoons on Wood" in Istanbul, Turkey, October 17 - November 4, 2018, at the Schneidertempel Arts Center.

In their Ethically Speaking column, Randy Haupt and Amy Shockley use an experience with a baby owl to illustrate the importance of following through on actions. We think of owls as being wise. In this case, it was the humans helping the owl who displayed the wisdom.

Özgür Ergül has brought us another fascinating computational electromagnetics problem in his Solution Box. Solution Box 12, by Hande İbili, Barışcan Karaosmanoğlu, and Özgür Ergül, considers three-dimensional frequency-domain scattering problems. Rather than the geometry or the size in terms of a wavelength causing challenges, in these problems it is the extreme values of the permittivity that result in computational issues. As always, Özgür is looking for alternative approaches to solving the problems, or other challenging computational electromagnetics problems to share with our readers.

In his Telecommunications Health and Safety column, Jim Lin takes a critical look at the US DARPA (Defense Advanced Research Projects Agency) RadioBio research program. The stated goal of this project was to “determine if purposeful signaling via electromagnetic waves between biological systems exists, and, if it does, determine what information is being transferred.” The implications are fascinating.

Asta Pellinen-Wannberg has brought us a story about the career of Dr. Ivana Kolmasova, who works at the Institute of Atmospheric Physics of the Czech Academy of Sciences, as well as at the Charles University in Prague.

Dr. Kolmasova shares some interesting perspectives on how she has combined engineering and physics. She also has a suggestion for enlarging the scope of this column.

Plan to Attend URSI AP-RASC 2019!

The URSI Asia-Pacific Radio Science Conference (AP-RASC 2019) will be held March 9-15, 2019, in New Delhi, India. Information is available at <http://aprasc2019.com/>. Over 952 papers were submitted from 40 countries. This is going to be an outstanding conference! This is one of URSI's three flagship conferences: You should make your plans now to attend. Note that if you require a visa to attend the conference, you may wish to apply for the visa well in advance. Some people have been able to get a visa using the online application system in as little as one day; for others, it has taken as long as two months. The Web site is open now for registration and hotel reservations. I hope I will see you there!



Mitigation of Non-Narrowband Radio-Frequency Interference

*Jan-Willem W. Steeb¹,
David B. Davidson^{2,1}, and
Stefan J. Wijnholds^{3,1}*

¹Department of Electrical & Electronic Engineering Stellenbosch University
South Africa

²International Centre for Radio Astronomy Research (ICRAR)
Curtin University
Australia

³Netherlands Institute for Radio Astronomy (ASTRON)
The Netherlands
E-mail: jwsteeb@gmail.com

Abstract

The rapid development and implementation of wireless communication standards put increasing pressure on spectrum allocation, and therefore threaten the efficacy of radio astronomy. For example, digital audio broadcasting (DAB) is a wide-bandwidth broadcast technology that is now being implemented and has spectrum allocated in the L band. We demonstrate that standard narrowband subspace subtraction methods may provide insufficient suppression of such signals. We therefore propose two algorithms that take into account the non-narrowband nature of these signals. The first proposed algorithm is based on a flat-frequency-response model. The second is an approximation of the first that makes use of two frequency-shifted monochromatic sources (Zatman's model). An experimental demonstration of both proposed algorithms yielded an increase of approximately a factor six in bandwidth per channel that can be processed when compared to conventional narrowband techniques (for the same attenuation of the RFI signal). The performance of the two methods was identical for LOFAR station configurations with bandwidths between 763 Hz and 195 kHz. However, the model based on Zatman's algorithm required fewer operations (a speed-up of 1.3 was achieved). An equation is derived that gives the direction of arrival for a far-field non-narrowband signal that causes the greatest distortion of the visibilities. Another equation is derived for the appropriate frequency channel bandwidth at which to implement the proposed non-narrowband RFI mitigation algorithms.

1. Introduction

In the development of radio-frequency-interference (RFI) mitigation methods, the assumption that the RFI is narrowband is usually made. If this is the case, spatial RFI mitigation methods, such as orthogonal projection, orthogonal projection with subspace bias correction, oblique projection, and subspace subtraction [1-3] can be applied. When the signal is not narrowband, the model for the array-response vector becomes a function of bandwidth. The result is that the RFI will appear as an extended source that can be modeled as multiple sources, albeit with rapidly decreasing power. To evaluate the proposed RFI mitigation methods, the layout of high-band antenna (HBA) station RS407 in the Low-Frequency Array (LOFAR) [4] was used. The high-band antenna stations in LOFAR have an operating band from 110 MHz to 240 MHz that contains many digital audio broadcasts.

To demonstrate the effect of bandwidth on a sky image, a simulation was done using the layout of a LOFAR high-band antenna station. In Figure 1a, the sky map was dominated by the RFI source. When a first-order orthogonal-projection filter was applied, the sky map in Figure 1b was obtained. The orthogonal projector reduced the power of the RFI source by 40 dB, and revealed two sources that were separated along the radial direction. These two sources were not real physical sources, but were caused by frequency smearing [5].

Two signal models will be used: a flat-frequency-response model and Zatman's approximation [6].

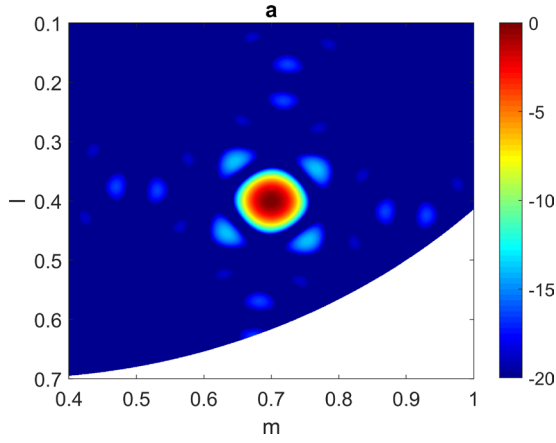


Figure 1a. A sky map with a non-narrowband RFI source visible, in dB (the RFI source is the 0 dB point).

Furthermore, equations will be derived for the RFI covariance matrix's eigenvalues, as well as for the direction of arrival that causes the largest deviation from the narrowband point-source model, the appropriate bandwidth at which to apply spatial filtering, and the RFI covariance matrix's vector space. Two new subspace-subtraction algorithms that make use of the two models developed for the RFI covariance matrix's vector space are subsequently presented and evaluated.

2. Notation

A	Bold upper-case letters are matrices. The jk^{th} element is indicated by \mathbf{A}_{jk} .
a	Bold lower-case letters are column vectors. The j^{th} element is indicated by \mathbf{a}_j .
I	Identity matrix.
\odot	Hadamard product.
$ \cdot $	Absolute value of a scalar.
$\text{Tr}(\cdot)$	Trace of a matrix.
$\text{diag}(\cdot)$	Converts a vector into a diagonal matrix.
\angle	Phase of a complex number.
i	Square root of -1 .
c	Speed of light.
$\{\cdot\}^H$	Hermitian transpose of a matrix.
$\{\cdot\}^T$	Transpose of a matrix.
$\{\cdot\}^*$	Complex conjugate of a scalar.
$\text{sinc}(x)$	$= \sin(\pi x)/(\pi x)$, normalized sinc function.
$\delta(x)$	Dirac delta function.

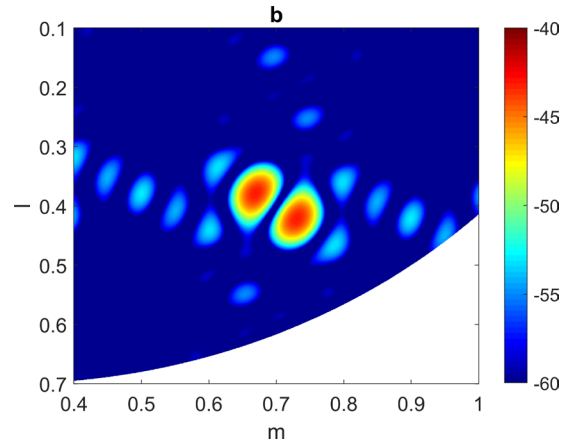


Figure 1b. A sky map with the non-narrowband RFI source removed, using a first-order orthogonal projection filter. Two weaker sources adjacent to the location of the RFI are now visible, and were caused by the bandwidth of the RFI source.

3. Narrowband Signal Model

If omnidirectional antennas are used, then the normalized array response vector for an array with N_e elements and a continuous wave source with frequency ν is given by

$$\mathbf{a} = \begin{bmatrix} b_1 e^{-i2\pi\nu\tau_1} \\ \vdots \\ b_{N_e} e^{-i2\pi\nu\tau_{N_e}} \end{bmatrix}. \quad (1)$$

If the source lies in the far field, then the geometrical delays and normalization constants are

$$\tau_j = -\left(l_s x_j + m_s y_j + n_s z_j \right) / c, \quad (2)$$

$$b_j = 1/\sqrt{N_e}, \quad (3)$$

where x_j, y_j, z_j are the Cartesian coordinates of the j^{th} antenna, and the directional cosines are defined as

$$l_s = \sin(\theta_s) \cos(\phi_s), \quad (4)$$

$$m_s = \sin(\theta_s) \sin(\phi_s), \quad (5)$$

$$n_s = \cos(\theta_s), \quad (6)$$

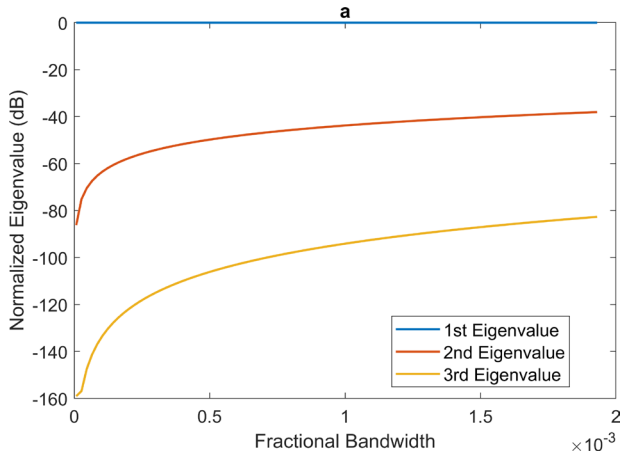


Figure 2a. A plot (assuming a flat frequency response) of the simulated three largest normalized eigenvalues as a function of fractional bandwidth using the layout of the LOFAR high-band antenna station RS407 and an RFI source on the horizon. The center frequency was 183 MHz and the bandwidth was varied from 763 Hz to 195 kHz.

where θ_s and ϕ_s are, respectively, the polar and azimuthal angles of the spherical coordinates of the source (ISO convention). The array covariance matrix for a single source without noise is given by

$$\mathbf{R} = \sigma_s^2 \mathbf{a} \mathbf{a}^H, \quad (7)$$

$$\mathbf{R}_{jk} = b_j b_k \sigma_s^2 e^{-i2\pi\tau_{jk} \nu}, \quad (8)$$

where σ_s^2 is the signal power, \mathbf{R}_{jk} is the jk^{th} element in the covariance matrix, and $\tau_{jk} = \tau_j - \tau_k$.

All examples in this paper make use of sources in the far field. However, any of the presented methods can be used for near-field sources by setting $\tau_j = r_{sj}/c$ and

$$b_j = 1 / \left(r_{sj} \sqrt{\sum_{n=1}^N 1/r_{sn}^2} \right),$$

where the distance between the j^{th} antenna and the source is denoted by r_{sj} [7, pp. 113-115].

4. Non-Narrowband Signal Model

If the channel bandwidth is not sufficiently narrow, the dependence of the array response vector on frequency becomes significant. The frequency-dependent covariance matrix, $\mathbf{R}(\nu)$, with only a single interferer (no noise or cosmic sources) that is modeled as a point source can be written as

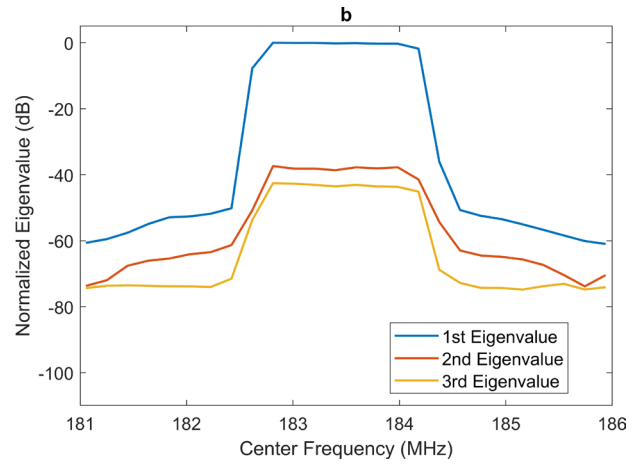


Figure 2b. The three largest normalized eigenvalues as a function of center frequency calculated from the covariance matrices obtained from an observation using LOFAR station RS407 with a bandwidth of 195 kHz. The elevated flat spectrum of a digital audio broadcasting signal can clearly be seen between 182.9 MHz to 184.4 MHz.

$$\mathbf{R}(\nu) = \sigma_s^2(\nu) \mathbf{a}(\nu) \mathbf{a}^H(\nu), \quad (9)$$

where $\mathbf{a}(\nu)$ is the normalized frequency-dependent array-response vector. When the different frequency components are uncorrelated, the total covariance matrix is found by integrating over the entire bandwidth

$$\mathbf{R} = \frac{1}{\Delta\nu} \int_{\nu_0 - \Delta\nu/2}^{\nu_0 + \Delta\nu/2} \sigma_s^2(\nu) \mathbf{a}(\nu) \mathbf{a}^H(\nu) d\nu, \quad (10)$$

where $\Delta\nu$ is the bandwidth and ν_0 is the center frequency. For a flat frequency response, the integral in Equation (10) can be calculated and the jk^{th} element is given by

$$\begin{aligned} \mathbf{R}_{jk} &= \frac{\sigma_s^2 b_j b_k}{\Delta\nu} \int_{\nu_0 - \Delta\nu/2}^{\nu_0 + \Delta\nu/2} e^{-i2\pi\tau_{jk}\nu} d\nu \\ &= \sigma_s^2 b_j b_k \text{sinc}(\tau_{jk} \Delta\nu) e^{-i2\pi\tau_{jk}\nu_0}. \end{aligned} \quad (11)$$

By taking the bandwidth into consideration (and assuming a flat frequency response), this covariance matrix model differs from the narrowband model (see Equation (8)) with a sinc function that is dependent on the delay, τ_{jk} , and the bandwidth, $\Delta\nu$. As the bandwidth increases from a single frequency, the sinc function starts to decrease from unity, and the effect is that the covariances start to decorrelate. This causes the eigenvalue structure of the array covariance matrix to change. For a single-frequency

signal, there will only be one non-zero eigenvalue. For a non-zero-bandwidth signal, the covariance matrix will be of full rank, since it is an infinite sum of frequencies. As the bandwidth increases, the largest eigenvalue will decrease and the other eigenvalues will increase, as can be seen in Figure 2a (where, even though the largest eigenvalue appears constant due to the log scale of the figure, it is decreasing). However, most of the eigenvalues will be so small relative to the cosmic sources and the noise in the system that they can be approximated by zero. The effective rank of the RFI covariance matrix (no noise or cosmic sources) is then defined to be equal to the number of eigenvalues that are significant when compared to the eigenvalues of the covariance matrix that contains only the cosmic sources and noise.

The entire fractional bandwidth range used to generate Figure 2a would be considered narrowband in the traditional signal-processing sense. However, the power of some RFI sources is so high that it can be more than 70 dB above the noise, and even 60 dB above a bright radio source such as Cassiopeia A. The contribution of the RFI source to the second eigenvalue can therefore still be significant relative to that of the cosmic sources. Figure 2b shows a plot of the three largest eigenvalues from an observation using LOFAR high-band antenna station RS407 as a function of center frequency. The bandwidth used for the observation was 195 kHz, and the digital audio broadcasting signal could be clearly seen from 182.9 MHz to 184.4 MHz. The second eigenvalue for the digital audio broadcasting signal was at approximately -40 dB and agreed with the simulated results in Figure 2a. However, there was no agreement between the simulated and measured third eigenvalue. This was due to calibration errors and the frequency response not being perfectly flat.

5. Model Based on Zatman's Approximation

If a covariance matrix has an effective rank of two, it can be approximated by the sum of two discrete uncorrelated signals:

$$\mathbf{R} \approx \sigma_1^2 \mathbf{a}_1 \mathbf{a}_1^H + \sigma_2^2 \mathbf{a}_2 \mathbf{a}_2^H. \quad (12)$$

The closed-form solution for the eigenvalues of the system given in Equation (12) is [3, pp. 65]

$$\lambda_{1,2} = \frac{1}{2}(\sigma_1^2 + \sigma_2^2) \left[1 \pm \sqrt{1 - 4 \frac{\sigma_1^2 \sigma_2^2 (1 - |\mathbf{a}_1^H \mathbf{a}_2|^2)}{(\sigma_1^2 + \sigma_2^2)^2}} \right]. \quad (13)$$

In the model proposed by Zatman, the signals are required to have equal power ($\sigma_1^2 = \sigma_2^2 = \sigma^2$) [6]. The equal-power criterion is achieved when the discrete sources are arranged in such a way that the instantaneous frequency spectrum's mean and variance respectively correspond to the mean and variance of the non-zero-bandwidth signal. Consequently, the distance from the center frequency, ν_0 , is given by

$$\kappa = \frac{\Delta \nu}{2\sqrt{3}}. \quad (14)$$

The model in Equation (12) thus becomes

$$\begin{aligned} \mathbf{R} &\approx \sigma^2 \mathbf{a}(\nu_0 + \kappa) \mathbf{a}^H(\nu_0 + \kappa) + \sigma^2 \mathbf{a}(\nu_0 - \kappa) \mathbf{a}^H(\nu_0 - \kappa) \\ &= \sigma^2 (\mathbf{a}_1 \mathbf{a}_1^H + \mathbf{a}_2 \mathbf{a}_2^H). \end{aligned} \quad (15)$$

Zatman's approach is now generalized from a uniform linear array to an array of any shape using the normalized response vector in Equation (1) and the assumption that $\sigma_1^2 = \sigma_2^2 = \sigma^2$. Consequently, Equation (13) simplifies to

$$\lambda_{1,2} = \sigma^2 (1 \pm |\psi|), \quad (16)$$

where $\psi = \mathbf{a}_1^H \mathbf{a}_2$. In Figure 3a, the power spectral densities of the flat-frequency model as well as of the model based on Zatman's approximation are plotted. In the frequency domain, the model based on Zatman's approximation is represented by two frequency-shifted Dirac deltas. The total covariance matrix for the model based on Zatman's approximation is found by integrating over the entire bandwidth (see Equation (11) for the flat-frequency-model case):

$$\begin{aligned} \mathbf{R}_{jk} &\approx \frac{\sigma_s^2 b_j b_k}{2} \left[\int_{-\infty}^{\infty} \delta(\nu - \nu_0 + \kappa) e^{-i2\pi\tau_{jk}\nu} d\nu \right. \\ &\quad \left. + \int_{-\infty}^{\infty} \delta(\nu - \nu_0 - \kappa) e^{-i2\pi\tau_{jk}\nu} d\nu \right] \\ &= \sigma_s^2 b_j b_k \cos(\pi\tau_{jk}\Delta\nu/\sqrt{3}) e^{-i2\pi\tau_{jk}\nu_0}. \end{aligned} \quad (17)$$

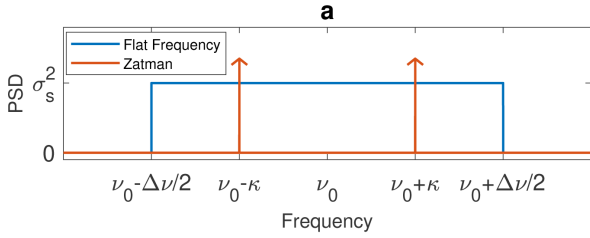


Figure 3a. The power spectral density (PSD) as a function of frequency. The flat-frequency model is represented by a square pulse, and the model based on Zatman's approximation is represented by two frequency-shifted Dirac deltas.

Where the flat-frequency-model causes a $\text{sinc}(\tau_{jk}\Delta\nu)$ decorrelating function to appear, the model based on Zatman's approximation results in a $\cos(\pi\tau_{jk}\Delta\nu/\sqrt{3})$ decorrelating function for the total covariance matrix (see Figure 3b for plots of the decorrelating functions). There is agreement between the models for the peak centered at $\Delta\nu = 0$. However, as the bandwidth increases, the Zatman decorrelating function oscillates, and the flat-frequency decorrelating function attenuates. At a bandwidth of $\Delta\nu = 1/\tau_{jk}$, the flat-frequency decorrelating function is zero. Using the LOFAR high-band antenna station RS407 longest baseline and assuming the longest delay possible yields $\Delta\nu = 7.65$ MHz, which is far larger than any LOFAR channel bandwidth. For the standard channel bandwidth of 195 kHz, the difference between the two models' decorrelating function (in the case of the longest possible delay) is only -1.52×10^{-7} . The model based on Zatman's approximation is therefore adequate for modeling LOFAR high-band antenna signals with a flat frequency response.

5.1 Worst-Case Scenario

Minimizing $|\psi|$ maximizes λ_2 , which is the worst-case scenario. Minimizing $|\psi|^2$ is also the same as minimizing $|\psi|$, since it is a positive function. After expanding and simplifying,

$$|\psi|^2 = \sum_{p=1}^{N_e} b_p^4 + \sum_{j=1}^{N_e-1} \sum_{k=j+1}^{N_e} 2b_j^2 b_k^2 \cos(4\pi\tau_{jk}\kappa). \quad (18)$$

We will make the following assumptions:

- The array is planar (that is, $z_{jk} = 0$).
- The RFI source lies in the far field (therefore use Equations (2) and (3)).
- The argument $4\pi\tau_{jk}\kappa \ll \pi/2$, therefore the Taylor expansion $\cos(x) \approx 1 - \frac{x^2}{2}$ can be used.

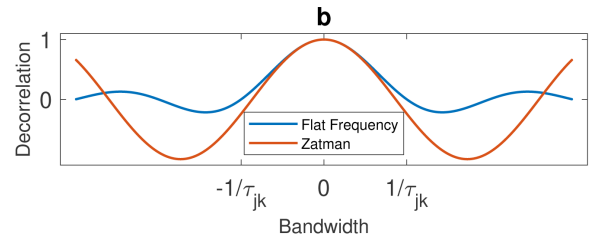


Figure 3b. The decorrelation as a function of bandwidth. The decorrelating function for the flat-frequency-model covariance matrix was $\text{sinc}(\tau_{jk}\Delta\nu)$, and for the model based on Zatman's approximation it was $\cos(\pi\tau_{jk}\Delta\nu/\sqrt{3})$.

Using these assumptions, Equation (18) simplifies to

$$\begin{aligned} |\psi|^2 &= 1 - \frac{16\pi^2\kappa^2}{N_e^2} \left(\sum_{j=1}^{N_e-1} \sum_{k=j+1}^{N_e} \tau_{jk}^2 \right) \\ &= 1 - \frac{16\pi^2\kappa^2}{N_e^2} (\alpha_1 l^2 + \alpha_2 lm + \alpha_3 m^2) \quad (19) \\ &= 1 - \frac{16\pi^2\kappa^2}{N_e^2} \zeta(l, m), \end{aligned}$$

where

$$\begin{aligned} \alpha_1 &= \sum_{j=1}^{N_e-1} \sum_{k=j+1}^{N_e} \frac{x_{jk}^2}{c^2}, \\ \alpha_2 &= 2 \left(\sum_{j=1}^{N_e-1} \sum_{k=j+1}^{N_e} \frac{x_{jk} y_{jk}}{c^2} \right), \\ \alpha_3 &= \sum_{j=1}^{N_e-1} \sum_{k=j+1}^{N_e} \frac{y_{jk}^2}{c^2}, \end{aligned}$$

$$\zeta(l, m) = \alpha_1 l^2 + \alpha_2 lm + \alpha_3 m^2.$$

To minimize $|\psi|^2$, the positive function $\zeta(l, m)$ must therefore be maximized. Substituting Equations (4) to (6) into ζ yields

$$\zeta(\theta, \phi) = \sin^2\theta(\alpha_1 \cos^2\phi + \alpha_2 \cos\phi \sin\phi + \alpha_3 \sin^2\phi). \quad (20)$$

Clearly, the positive function ζ is maximized when $\theta = \pi/2$. The partial derivative of ζ with respect to ϕ is

$$\frac{\delta\zeta}{\delta\phi} = \sin^2\theta(-2\alpha_1 \cos\phi \sin\phi - \alpha_2 \sin^2\phi + \alpha_2 \cos^2\phi + 2\alpha_3 \sin\phi \cos\phi) \quad (21)$$

$$= \sin^2\theta[(\alpha_3 - \alpha_1)\sin(2\phi) + \alpha_2 \cos(2\phi)].$$

Setting $\theta = \pi/2$ and $\frac{\delta\zeta}{\delta\phi} = 0$, ζ is maximized by

$$\phi = \frac{1}{2} \tan^{-1}\left(\frac{\alpha_2}{\alpha_1 - \alpha_3}\right) \quad (22)$$

if $\frac{\delta^2\zeta}{\delta\phi^2} < 0$, that is,

$$[(\alpha_3 - \alpha_1)\cos(2\phi) - \alpha_2 \sin(2\phi)] < 0. \quad (23)$$

By maximizing ζ , the arrival direction is found so that the mean delay for the RFI signal between the antennas is maximized, which then gives the largest second eigenvalue.

6. Appropriate Bandwidth for Spatial Filtering

Spatial nulling techniques work by modifying eigenvalues in the measured covariance matrix that are associated with the RFI subspace. For example, orthogonal projection makes those eigenvalues zero. As the number of eigenvalues that are modified increases, so does the loss in information [1]. The lowest-order filter that sufficiently suppresses the RFI is therefore desired. This criterion can be met by setting the channel bandwidth so that the second eigenvalue lies sufficiently below the noise floor,

$$\lambda_2 \ll \sigma_n^2 \left(1 + \sqrt{N_c/N_t}\right)^2, \quad (24)$$

where N_t is the number of samples used to estimate the array covariance matrix [1].

For a planar array, the required bandwidth can be calculated by substituting Equation (19) into the equation for the ratio λ_2/λ_1 (see Equation (16)) and solving for the bandwidth:

$$\Delta\nu = 2\sqrt{3} \sqrt{\left[1 - \left(\frac{1 - \lambda_2/\lambda_1}{1 + \lambda_2/\lambda_1}\right)^2\right] \frac{N_c^2}{16\pi^2\zeta(l, m)}}. \quad (25)$$

A suitable value for λ_2 can be determined by using Equation (24). An approximate estimate for λ_1 can be obtained from a covariance matrix constructed from a signal with the default array bandwidth by computing the eigenvalue decomposition and subtracting the noise power from the largest eigenvalue. Using the default bandwidth, which is usually larger than the bandwidth calculated in Equation (25), causes the estimate of λ_1 to be slightly lower, and has little effect on the ratio λ_2/λ_1 since $\lambda_1 \ll \lambda_2$. The l and m coordinates can either be the worst-case scenario (see Section 5.1) or the coordinates of the RFI, which are often known in the case of a digital audio broadcasting broadcast.

Increasing the bandwidth so that the second eigenvalue is above the noise and then using second-order spatial filtering will not sufficiently remove the RFI. The reason is that the third eigenvalue will then have a significant impact, because no array is perfectly calibrated and the frequency response is not completely flat, which causes the third eigenvalue to be substantially higher than predicted by the model (see Figures 2a and b). To increase the bandwidth that can be processed or the RFI suppression, the algorithms that are proposed in Section 8 construct a second-order filter that does not require the second eigenvalue to be above the noise.

7. Approximating RFI Vector Space

The RFI covariance matrix in Equation (15) can be rewritten in terms of its eigenvalue decomposition:

$$\mathbf{R} \approx \sigma^2 (\mathbf{a}_1 \mathbf{a}_1^H + \mathbf{a}_2 \mathbf{a}_2^H) = \lambda_1 \mathbf{v}_1 \mathbf{v}_1^H + \lambda_2 \mathbf{v}_2 \mathbf{v}_2^H, \quad (26)$$

which maximizes the power in the direction of \mathbf{v}_1 , with the remaining power contained in the direction of \mathbf{v}_2 . Both vectors are linear combinations of \mathbf{a}_1 and \mathbf{a}_2 ,

$$\mathbf{v}_{1,2} = \beta_{1,2} \mathbf{a}_1 + \gamma_{1,2} \mathbf{a}_2, \quad (27)$$

with the following properties:

- $\mathbf{v}_1^H \mathbf{v}_1 = \mathbf{v}_2^H \mathbf{v}_2 = 1$ (\mathbf{v}_1 and \mathbf{v}_2 are unit vectors),
- $\mathbf{v}_1^H \mathbf{v}_2 = \mathbf{v}_2^H \mathbf{v}_1 = 0$ (\mathbf{v}_1 and \mathbf{v}_2 are orthogonal).

Using the definition of an eigenvector and eigenvalue,

$$\begin{aligned} \mathbf{R}\mathbf{v} &\approx \sigma^2 (\mathbf{a}_1 \mathbf{a}_1^H + \mathbf{a}_2 \mathbf{a}_2^H) (\beta \mathbf{a}_1 + \gamma \mathbf{a}_2) \\ &= \sigma^2 (\beta \mathbf{a}_1 + \gamma \psi \mathbf{a}_1 + \beta \psi^* \mathbf{a}_2 + \gamma \mathbf{a}_2) \\ &= \lambda \mathbf{v} = \lambda \beta \mathbf{a}_1 + \lambda \gamma \mathbf{a}_2. \end{aligned}$$

Comparing the coefficients of \mathbf{a}_1 and \mathbf{a}_2 , respectively, yields

$$\lambda \beta = \sigma^2 (\beta + \gamma \psi), \quad (28)$$

$$\lambda \gamma = \sigma^2 (\beta \psi^* + \gamma). \quad (29)$$

Substituting $\lambda = \lambda_{1,2} = \sigma^2 (1 \pm |\psi|)$, $\beta = \beta_{1,2}$, and $\gamma = \gamma_{1,2}$ into Equations (28) and (29) yields

$$\beta_{1,2} = \pm \frac{\gamma_{1,2} \psi}{|\psi|}, \quad (30)$$

$$\gamma_{1,2} = \pm \frac{\beta_{1,2} \psi^*}{|\psi|}, \quad (31)$$

$$|\beta_{1,2}|^2 = |\gamma_{1,2}|^2. \quad (32)$$

Using the property that \mathbf{v} is a unit vector gives

$$\begin{aligned} \mathbf{v}^H \mathbf{v} = 1 &= (\beta^* \mathbf{a}_1^H + \gamma^* \mathbf{a}_2^H) (\beta \mathbf{a}_1 + \gamma \mathbf{a}_2) \\ &= |\beta|^2 + \beta^* \gamma \psi + \gamma^* \beta \psi^* + |\gamma|^2. \end{aligned} \quad (33)$$

Substituting Equations (31) and (32) yields

$$|\beta_{1,2}|^2 = \frac{1}{2(1 \pm |\psi|)}. \quad (34)$$

The phase of either β or γ can be arbitrarily chosen (see Equations (30) to (33)). There is also no phase relationship between β_1, γ_1 , and β_2, γ_2 , as can be seen by expanding $\mathbf{v}_1^H \mathbf{v}_2 = 0$. The phase of $\beta_{1,2}$ is fixed to 0, and thus $\beta_{1,2} = 1/\sqrt{2(1 \pm |\psi|)}$. Substituting Equation (31) into Equation (27) yields

$$\mathbf{v}_1 = \frac{1}{\sqrt{2(1+|\psi|)}} \left(\mathbf{a}_1 + \frac{\psi^*}{|\psi|} \mathbf{a}_2 \right), \quad (35)$$

$$\mathbf{v}_2 = \frac{1}{\sqrt{2(1-|\psi|)}} \left(\mathbf{a}_1 - \frac{\psi^*}{|\psi|} \mathbf{a}_2 \right). \quad (36)$$

To construct \mathbf{v}_2 from Equation (36), the direction of arrival of the RFI (which can be obtained by using algorithms such as MUSIC and ESPRIT) as well as the signal bandwidth are required.

8. Proposed RFI Mitigation Algorithms

Two new spatial RFI mitigation algorithms, based on subspace subtraction, are presented in this section. These algorithms are designed for non-narrowband RFI that is stationary, such as digital audio broadcasting broadcasts. The channel bandwidth should be selected so that the second eigenvalue of the sample covariance matrix, $\hat{\mathbf{R}}$, is lower or equal to the power of the cosmic sources being observed, and can be computed using Equation (25). The first algorithm is based on the flat-frequency-response model

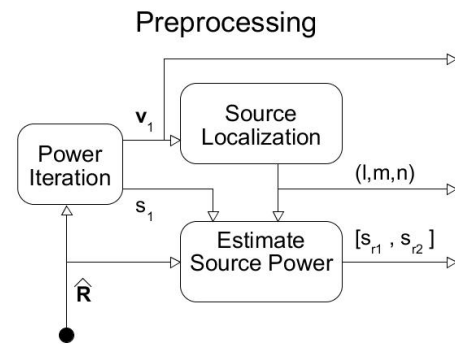


Figure 4. The activity diagram of the preprocessing stage.

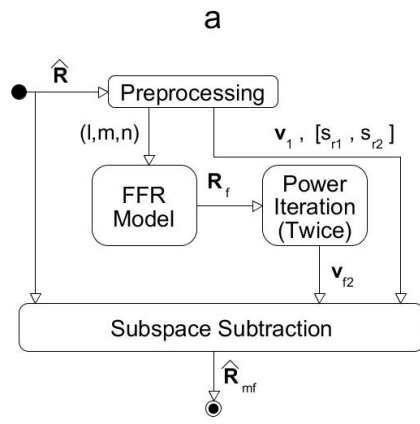


Figure 5a. The activity diagram for algorithm 1, which uses the flat-frequency model in Equation (11).

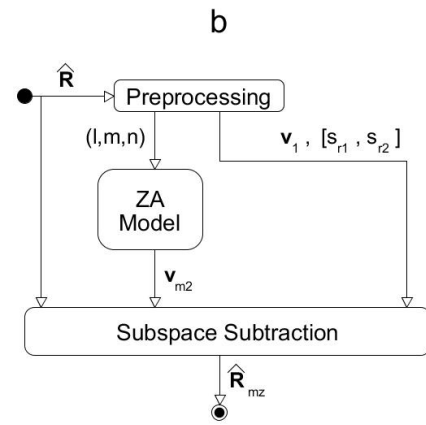


Figure 5b. The activity diagram for algorithm 2, which uses Zatman's approximation in Equation (36).

(see Equation (11)), and the second algorithm is based on Zatman's approximation to that model (see Equation (36)). The following preprocessing steps are required (see Figure 4 for an activity diagram of the preprocessing stage):

- Use the power-iteration method on $\hat{\mathbf{R}}$ to find the largest eigenvalue, s_1 , with the accompanying eigenvector, \mathbf{v}_1
- Obtain the location of the RFI source. For example, the location of digital audio broadcasting towers can be easily obtained and used as the initial guess for a fast iterative algorithm such as Minimum Error Convergence [8]. If no initial guess can be made, algorithms such as MUSIC or ESPRIT can be used [9, pp. 80-82].
- Estimates for the two largest eigenvalues of the RFI-only covariance matrix can be obtained by using the estimated location of the RFI and Equation (16):

$$s_{r1} = s_1 - \frac{\text{Tr}(\hat{\mathbf{R}}) - s_1}{N_e - 1}, \quad (37)$$

$$s_{r2} = s_{r1} \left(\frac{1 - |\psi|}{1 + |\psi|} \right). \quad (38)$$

Use these two new eigenvalue estimates to create the matrix $\mathbf{S}_r = \text{diag}([s_{r1}, s_{r2}]^T)$.

8.1 Algorithm 1

This is the flat-frequency-response-model-based algorithm (FF algorithm, see Figure 5a for the activity diagram):

- Calculate the normalized flat-frequency-covariance-matrix model of the RFI source \mathbf{R}_f , using Equation (11).

Note that this model covariance matrix does not include any noise, and that $\sigma_s^2 = 1$.

- Use the power-iteration method on \mathbf{R}_f to find the second-largest eigenvalue's eigenvector, \mathbf{v}_{2f} .
- Apply subspace subtraction to obtain the flat-frequency-model-based RFI-mitigated covariance matrix:

$$\hat{\mathbf{R}}_{mf} = \hat{\mathbf{R}} - [\mathbf{v}_1, \mathbf{v}_{2f}] \mathbf{S}_r [\mathbf{v}_1, \mathbf{v}_{2f}]^H. \quad (39)$$

8.2 Algorithm 2

This is the algorithm based on Zatman's approximation (ZA algorithm, see Figure 5b for the activity diagram):

- Calculate the model eigenvector \mathbf{v}_{2z} based on the normalized Zatman's approximation using Equation (36).
- Apply subspace subtraction to obtain the RFI-mitigated covariance matrix based on Zatman's approximation:

$$\hat{\mathbf{R}}_{mz} = \hat{\mathbf{R}} - [\mathbf{v}_1, \mathbf{v}_{2z}] \mathbf{S}_r [\mathbf{v}_1, \mathbf{v}_{2z}]^H. \quad (40)$$

9. Evaluation of RFI Mitigation Algorithms

To evaluate the performance of both proposed algorithms, an estimated covariance matrix was created by adding an estimated noise and cosmic source covariance matrix, $\hat{\mathbf{R}}_{nc}$, to an estimated RFI covariance matrix, $\hat{\mathbf{R}}_r$. The matrix $\hat{\mathbf{R}}_{nc}$ was obtained from a real observation done with LOFAR high-band antenna station RS407 where there

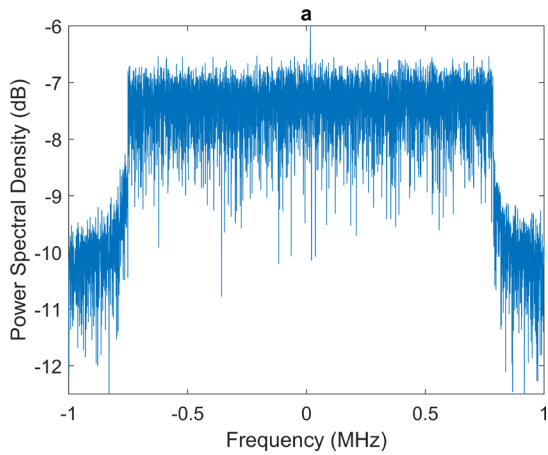


Figure 6a. The power spectrum of a digital audio broadcasting signal measured with a software-defined radio.

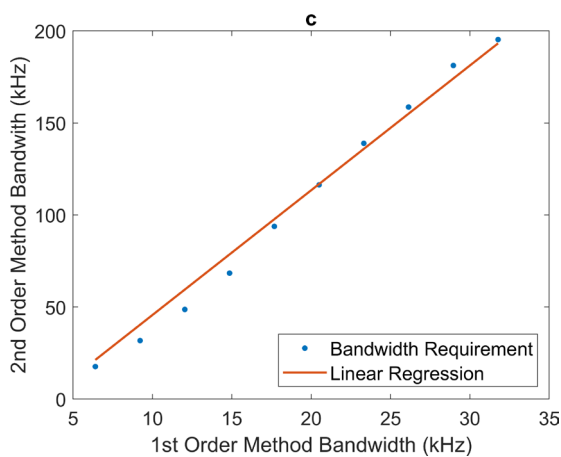


Figure 6c. A plot of the bandwidth of the second-order methods as a function of the bandwidth of the first-order method to achieve the same attenuation.

was no RFI present. A software-defined radio was used to record a digital audio broadcasting signal with the power spectrum shown in Figure 6a, which had a reasonably flat frequency spectrum. Finite-impulse-response filters were used to produce 70 signals with bandwidths ranging from 763 Hz to 195 kHz (typical values for LOFAR). Each filtered signal was used to generate a delayed signal for each antenna in the array. The delay was added by computing the fast Fourier transform of the filtered signal and multiplying each frequency component with the appropriate delay, and then computing the inverse fast Fourier transform. For each bandwidth, a $\hat{\mathbf{R}}_r$ covariance matrix was created by correlating the delayed signals for 1.5 s.

To measure the performance of the proposed algorithms, the Frobenius norm of the difference between the recovered covariance matrix, $\hat{\mathbf{R}}_m$, and matrix $\hat{\mathbf{R}}_{nc}$ was calculated:

$$\text{FN} = \sqrt{\sum_{j=1}^N \sum_{k=1}^N |\hat{\mathbf{R}}_{nc,jk} - \hat{\mathbf{R}}_{m,jk}|^2} \quad (41)$$

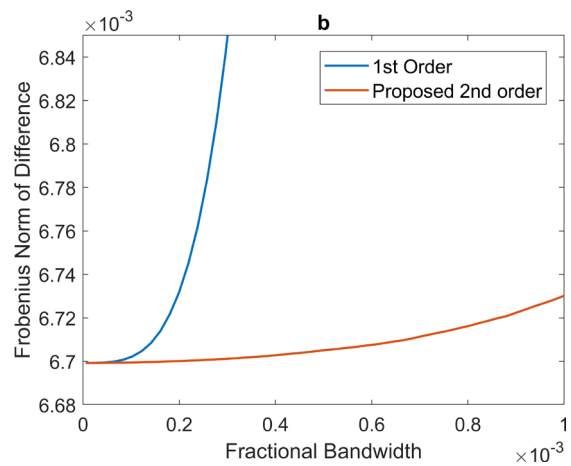


Figure 6b. The Frobenius norm of the difference between the recovered matrices using RFI mitigation methods and the noise and cosmic source covariance matrix as a function of fractional bandwidth. The first-order mitigation method makes use of single-frequency-subspace subtraction. The performance of the FF algorithm and the ZA algorithm were within 10^{-13} of each other, and are both represented by the proposed second-order line

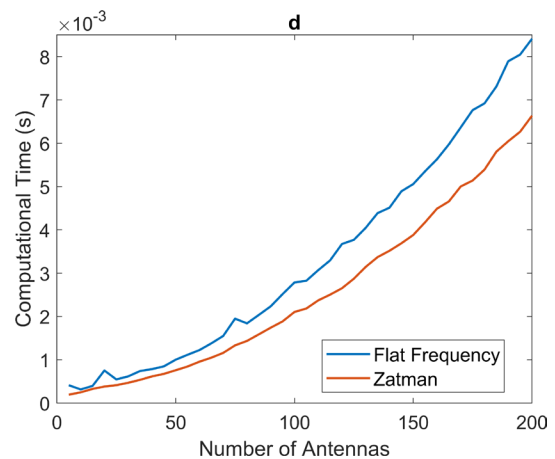


Figure 6d. The computational time of both proposed mitigation algorithms as a function of the number of antennas.

In Figure 6b, a plot is given of the Frobenius norm as a function of the fractional bandwidth. The difference in performance of the FF and the ZA algorithms was less than 10^{-13} , and both were represented by the proposed second-order line. The first-order line was the performance achieved by using single-frequency subspace subtraction. Close to zero fractional bandwidth, the performance of the first-order method and that of the second-order method was the same. As the bandwidth increased, so did the Frobenius norm for the first-order method, since the second eigenvalue became significant; however, the Frobenius norm for the second-order method showed very little increase. The minimum achievable Frobenius norm was 6.7×10^{-3} , and was due to the estimation errors in \mathbf{v}_1 and s_{r1} .

Channels with larger bandwidth can be processed using the second-order methods while achieving the same level of mitigation as the first-order method, which requires channels with smaller bandwidth. This is shown in Figure 6c, where the bandwidth required by the second-order method is given as a function of the bandwidth of the first-order method. Using a fitted straight line indicated an increase by approximately a factor of six in bandwidth that could be processed.

The FF algorithm and the ZA algorithm had the same performance for the bandwidths selected. Both algorithms have computational complexity $\mathcal{O}(N_e^2)$ (which includes the preprocessing step making use of the Minimum Error Convergence algorithm). However, the FF algorithm requires an additional calculation of an eigenvector, and the computational complexity of the FF algorithm's Equation (11) is $\mathcal{O}(N_e^2)$ compared to the ZA algorithm's Equation (36), which has computational complexity $\mathcal{O}(N_e)$. The quadratic growth of computational time as a function of the number of antennas is shown in Figure 6d. The ZA algorithm achieved a median speed-up of 1.3.

10. Conclusion

Strong, non-narrowband RFI cannot be modeled as a single point source, but rather as an infinite sum of sources that rapidly decrease in power. For traditional spatial filtering to work on powerful non-narrowband RFI it must be filtered into frequency channels that are sufficiently narrow so that for each frequency channel, the RFI source is a single point source. This greatly increases the computational cost. To reduce this cost, the FF and ZA algorithms were presented. They combine a non-narrowband signal model with a subspace-subtraction method and, in so doing, decrease the number of frequency channels that must be processed. The proposed algorithms are able to process approximately six times more bandwidth than conventional spatial-filtering methods. For bandwidths between 763 Hz and 195 kHz and a LOFAR high-band antenna-station layout, the performance of the proposed methods was similar. However, the ZA algorithm showed a speed-up of 1.3 relative to the FF algorithm.

11. Acknowledgements

This work is funded and supported by the South Africa Radio Astronomy Observatory, IBM, ASTRON, the Dutch Ministry of Economic Affairs, and the Province of Drenthe; the South African Research Chairs Initiative of the Department of Science and Technology, the National Research Foundation of South Africa, and the Netherlands Organisation for Scientific Research.

12. References

1. S. van der Tol and A. van der Veen, "Performance Analysis of Spatial Filtering of RF Interference in Radio Astronomy," *IEEE Transactions on Signal Processing*, **53**, 3, February 2005, pp. 896-910, doi:10.1109/TSP.2004.842177.
2. A. van der Veen, A. Leshem, and A. Boonstra, "Signal Processing for Radio Astronomical Arrays," Proceedings of the Sensor Array and Multichannel Signal Processing Workshop, July 2004, pp. 1-10, doi:10.1109/SAM.2004.1502901.
3. A. J. Boonstra, *Radio Frequency Interference Mitigation in Radio Astronomy*, PhD Thesis, Delft University of Technology, June 2005, uuid:caa1942c-4180-4a17-88db-cec359490aad.
4. M. P. van Haarlem, et al., "LOFAR: The Low Frequency Array," *Astronomy & Astrophysics*, **556**, A2, August 2013, pp. 1-53, doi:10.1051/0004-6361/201220873.
5. A. H. Bridle and F. R. Schwab, "Bandwidth and Time-Average Smearing," in G. B. Taylor, C. L. Carilli and R. A. Perley (eds.), *Synthesis Imaging in Radio Astronomy II*, **180**, 18, 1999, pp. 371-382, eISBN: 978-1-58381-516-8.
6. M. Zatman, "How Narrow is Narrowband?," *IEE Proceedings-Radar, Sonar and Navigation*, **145**, 2, April 1998, pp. 85-91, doi:10.1049/ip-rsn:19981670.
7. D. H. Johnson, and D. E. Dudgeon, *Array Signal Processing: Concepts and Techniques*, Upper Saddle River, NJ, Prentice-Hall, 1993, pp. 113-115.
8. J. W. Steeb, D. B. Davidson, and S. J. Wijnholds, "Computationally Efficient Near-Field Radio Frequency Source Localisation," 2017 XXXII Ind General Assembly and Scientific Symposium of the International Union of Radio Science (URSI GASS), August 2017, pp. 1-4, doi: 10.23919/URSIGASS.2017.8104498.
9. C. A. Balanis, and P. I. Ioannides, *Introduction to Smart Antennas*, Williston, VT, Morgan & Claypool Publishers, 2007, pp. 80-82.

Determining All Ambiguities in Direction of Arrival Measured By Radar Systems

Daniel Kastinen

Swedish Institute of Space Physics (IRF)
Box 812, SE-98128 Kiruna, Sweden
Umeå University
Department of Physics
SE-90187 Umeå, Sweden
E-mail: daniel.kastinen@irf.se

Abstract

There is an ambiguity problem when using radar systems to determine the position and motion of objects. This ambiguity manifests itself for certain sensor configurations when determining the direction of arrival (DOA) of an incoming electromagnetic plane wave onto the radar. Depending on the positions of the sensors in space, a radar system can respond the same way for several different plane-wave directions of arrival, thereby making it impossible to determine the true direction of arrival. We have therefore developed a mathematical framework and a practical method for finding all ambiguities in any multi-channel radar. We have used a set-intersection viewpoint to formulate an alternative form for the solutions to the ambiguity problem. The new formulation allows for an efficient implementation using the numerical Moore-Penrose inverse to find all ambiguities and approximate ambiguities. This definition led to the discovery of noise-induced ambiguities in theoretically ambiguity-free radars. Finally, we explore the possibility of using the sensor-gain patterns to resolve ambiguities and to restrict the elevation angle of a detection. This study originated in the need to resolve ambiguous meteor trajectories in data from the Middle and Upper Atmosphere Radar in Shigaraki, Japan. We have therefore used this radar as a practical example throughout the paper. Our results and methods can be used to classify ambiguities in any radar system, to design new radar systems, to improve trajectory estimation using statistical information, and to identify possibly faulty direction-of-arrival calculations and to correct them.

1. Introduction

Ever since Heinrich Hertz showed in 1886 that radio waves could be reflected from solid objects, the concept of radars have profoundly impacted science. The reflected radar signal, or echo, is an electromagnetic plane wave, and its direction of arrival (DOA) can be used to detect and discern position and motion. There are a plethora of methods

available today to determine the direction of arrival onto a multi-channel radar. However, the “ambiguity problem” sheds doubt on direction-of-arrival measurements [1, 2]. This doubt boils down to a single problem: that a signal output from a radar system could have been caused by waves from several different directions of arrival. Determining directions of arrival is critical in many research fields today. For example, in radar meteor science, direction-of-arrival measurements are used to calculate precise meteoroid trajectories and orbits [3]. The ambiguity problem is well known in the meteor community, and there are radar systems designed to minimize this problem [4, 5]. However, the problem persists due to reasons discussed in Section 4, and there is no standard way to address this problem or classify its severity.

This study originated in the need to resolve ambiguous meteor-head-echo directions of arrival in data from the Middle and Upper Atmosphere Radar (MU-radar) in Shigaraki, Japan, but the same techniques are also used to track satellites and space debris. Being able to trust these direction-of-arrival measurements is of vital importance if the data is to be used in simulations and consequent research, such as Monte Carlo-type simulations of meteor showers and their parent bodies [6].

We therefore have developed a mathematical framework and a practical method for finding all ambiguities and approximate ambiguities in any multi-channel radar system. We have also examined ambiguities induced by noise in theoretically ambiguity-free radars, such as the system reported in [4]. Finally, we explored the possibility of using the sensor-gain patterns to resolve ambiguities.

2. Mathematical Framework

2.1 Sensor-Response Models

We define the mathematical equivalent of a radar system by considering N antenna groups consisting of

n_j antennas each. These antennas have positions in space, denoted as \mathbf{h}_{jk} , where the group is indexed by j and the antenna is indexed by k . By combining the n_j signals from these antennas in each group, the radar system will output N signals, forming N sensors. We define the sensor positions as the geometric center, \mathbf{r}_j , of the antenna groups:

$$\mathbf{r}_j = \frac{1}{n_j} \sum_{k=1}^{n_j} \mathbf{h}_{jk}. \quad (1)$$

These N sensors will describe a measurement of an electromagnetic plane wave as a set of complex numbers, $\mathbf{x} \in \mathbb{C}^N$. An electromagnetic plane wave is described as

$$\Psi(\mathbf{r}, t, \mathbf{k}) = Ae^{i(\omega t - \langle \mathbf{k}, \mathbf{r} \rangle_{\mathbb{R}^3})}, \quad (2)$$

where ω is the angular frequency of the wave, \mathbf{k} is the wave vector, and $\langle \cdot, \cdot \rangle_{\mathbb{R}^3}$ is the inner product for the space \mathbb{R}^3 . The wave vector is in turn defined as

$$\mathbf{k}(\theta, \phi) = \frac{2\pi}{\lambda} \begin{bmatrix} \sin(\theta) \cos(\phi) \\ \cos(\theta) \cos(\phi) \\ \sin(\phi) \end{bmatrix}, \quad (3)$$

where an east-of-north azimuth, θ , and an elevation angle, ϕ , are used to define the direction of arrival. Here λ is the wavelength, which is considered to be constant. The time component of the wave will be omitted, as it makes no impact on future derivations.

We now have all the components needed to assemble a sensor-response model. A sensor-response model is used to extract information about the incoming wave by predicting how the sensor responds to a wave. The sensor-response model as a function of direction of arrival is

$$\begin{aligned} \mathbf{x}(\mathbf{k}) &= \begin{pmatrix} \Psi(\mathbf{r}_1, \mathbf{k}) \\ \vdots \\ \Psi(\mathbf{r}_N, \mathbf{k}) \end{pmatrix} \\ &= \begin{pmatrix} Ae^{-i\langle \mathbf{k}, \mathbf{r}_1 \rangle_{\mathbb{R}^3}} \\ \vdots \\ Ae^{-i\langle \mathbf{k}, \mathbf{r}_N \rangle_{\mathbb{R}^3}} \end{pmatrix} \\ &= \sum_{j=1}^N \hat{\mathbf{e}}_j Ae^{-i\langle \mathbf{k}, \mathbf{r}_j \rangle_{\mathbb{R}^3}} \end{aligned} \quad (4)$$

In Equation (4), the right-hand side uses index notation to define the vector, where $\hat{\mathbf{e}}_j$ is the standard orthonormal basis for the \mathbb{R}^N space.

2.2 Injective Condition

Ambiguities arise when a sensor-response model responds exactly the same way for different incoming waves, thus making it impossible to tell the events apart. If the sensor-response model has the property that for all the wave directions of arrival it never maps distinct directions of arrival to the same sensor response, then it is an injective function. The mathematical definition of this property is

$$\mathbf{f} : X \mapsto Y, \mathbf{f}(\mathbf{a}) = \mathbf{f}(\mathbf{b}) \Rightarrow \mathbf{a} = \mathbf{b} \quad \forall \mathbf{a}, \mathbf{b} \in X. \quad (5)$$

Applying this definition to our sensor-response model yields what we call the injective equation:

$$\mathbf{x}(\mathbf{k}_1) = \mathbf{x}(\mathbf{k}_2), \quad (6)$$

where $\mathbf{k}_1 = \mathbf{k}(\theta_1, \phi_1)$ and $\mathbf{k}_2 = \mathbf{k}(\theta_2, \phi_2)$. If there are solutions to this equation where $\mathbf{k}_1 \neq \mathbf{k}_2$, the function is non-injective. If we can prove that the only solutions are cases where $\mathbf{k}_1 = \mathbf{k}_2$, then the function is injective, and an injective function does not produce any ambiguities. By reducing Equation (6), we find

$$\begin{aligned} \mathbf{x}(\mathbf{k}_1) = \mathbf{x}(\mathbf{k}_2) &\Leftrightarrow \\ \Leftrightarrow \sum_{j=1}^N \hat{\mathbf{e}}_j \left(-i\langle \mathbf{k}_1, \mathbf{r}_j \rangle_{\mathbb{R}^3} \right) &= \sum_{j=1}^N \hat{\mathbf{e}}_j \left(-i\langle \mathbf{k}_2, \mathbf{r}_j \rangle_{\mathbb{R}^3} + 2\pi i I_j \right) \Leftrightarrow \\ \Leftrightarrow \sum_{j=1}^N \hat{\mathbf{e}}_j \left(\langle \mathbf{k}_2, \mathbf{r}_j \rangle_{\mathbb{R}^3} - \langle \mathbf{k}_1, \mathbf{r}_j \rangle_{\mathbb{R}^3} \right) &= \sum_{j=1}^N \hat{\mathbf{e}}_j 2\pi I_j \Leftrightarrow \\ \Leftrightarrow R\mathbf{k}_2 - R\mathbf{k}_1 = 2\pi\mathbf{I} &\Leftrightarrow \\ \Leftrightarrow R(\mathbf{k}_2 - \mathbf{k}_1) = 2\pi\mathbf{I}, \quad (7) \end{aligned}$$

where $\mathbf{I} \in \mathbb{Z}^N$ is an integer vector and R is a real-valued matrix of size $N \times 3$, i.e., N rows and 3 columns. The matrix R is defined with the sensor positions \mathbf{r}_j as row vectors \mathbf{r}_j^T , where T denotes the transpose. This derivation was first performed to find the uniqueness and linear independence of steering vectors in array space [1], although not from the injective-function viewpoint, but for the same reasons of describing ambiguity.

Using Equation (7), a theorem was formed so that no ambiguities can exist in a radar system [1]. The theorem is as follows: if at least four noncoplanar sensors labeled 1, 2, 3, and 4 exist such that $|\mathbf{r}_1 - \mathbf{r}_2| < \frac{\lambda}{2}$, $|\langle \hat{\mathbf{y}}, \mathbf{r}_1 - \mathbf{r}_3 \rangle_{\mathbb{R}^3}| < \frac{\lambda}{2}$, and $|\langle \hat{\mathbf{z}}, \mathbf{r}_1 - \mathbf{r}_4 \rangle_{\mathbb{R}^3}| < \frac{\lambda}{2}$, then the sensor array is ambiguity-free. Here $\hat{\mathbf{y}}$ and $\hat{\mathbf{z}}$ are basis vectors in \mathbb{R}^3 . This condition has been commonly used to classify radars as ambiguous or ambiguity-free. The condition has also been improved upon in a study of the rank-ambiguity issues in direction-of-arrival estimation [7], and has been used to design new radar systems without ambiguities while maximizing certain functions such as directional gain [8]. The above-described conditions are a result of simplifications, and thus exclude a lot of sensor configurations that are ambiguity-free. The conditions are also not useful for classifying ambiguities in existing radar systems, as they can only be true or false. In a study of high-altitude radar meteors observed at Jicamarca Radio Observatory, a numerical approach using phase additions of 2π was implemented to find ambiguities [9]. However, the approach only covered baseline pairs and a given source direction of arrival.

We have thus created a theoretical representation of the solution set, i.e., all ambiguities, that is easy to visualize and that can be practically calculated on a personal computer.

3. Solution

3.1 Theoretical Ambiguity Set

Solving Equation (7) is divided into two steps. The first step is to find the solution for all wave vector differences, $\mathbf{s} = \mathbf{k}(\theta_1, \phi_1) - \mathbf{k}(\theta_2, \phi_2)$. The second step is to translate the difference vector \mathbf{s} into pairs and sets of directions of arrival. Starting with the first step, inserting \mathbf{s} into Equation (7) gives

$$R\mathbf{s} = 2\pi\mathbf{I}. \quad (8)$$

In classical fashion, we shall first state the theorem describing the general solution to Equation (8) in terms of wave vector differences, \mathbf{s} , and then prove this theorem. Our proof also includes the geometrical intuition for this solution formulation.

3.1.1 Theorem 1

The solution set Ω of \mathbf{s} 's to Equation (8) can be found as a set of surface intersections

$$\Omega = \bigcap_{j=1}^N \left(\bigcup_{k=f_j^{\min}}^{f_j^{\max}} \mathbb{P}_{jk} \right) \quad \text{where} \quad f_j^{\max} = \left\lfloor 2 \frac{|\mathbf{r}_j|}{\lambda} \right\rfloor \quad \text{and} \quad f_j^{\min} = - \left\lfloor 2 \frac{|\mathbf{r}_j|}{\lambda} \right\rfloor$$

The surfaces that we union are circular plane sections, or disks, defined as

$$\mathbb{P}_{jk} = \left\{ \mathbf{s} \in \mathbb{R}^3 : |\mathbf{s}| \leq \frac{4\pi}{\lambda}, \langle \mathbf{s} + \mathbf{p}_{jk}, \mathbf{n}_j \rangle = 0 \right\},$$

where the plane normal is defined as $\mathbf{n}_j = \frac{\mathbf{r}_j}{|\mathbf{r}_j|}$ and the displacement point is defined as $\mathbf{p}_{jk} = \frac{k\lambda}{|\mathbf{r}_j|} \mathbf{n}_j$.

3.1.2 Proof of Theorem 1

To prove this theorem, we return to the inner-product form of Equation (7) and scale the variables:

$$\langle \mathbf{r}_j, \mathbf{s} \rangle = 2\pi\mathbf{I} \Leftrightarrow \langle \hat{\mathbf{r}}_j, \hat{\mathbf{s}} \rangle = \mathbf{I}, \quad (9)$$

where $\hat{\mathbf{r}}_j = \frac{\mathbf{r}_j}{\lambda}$ and $\hat{\mathbf{s}} = \frac{\lambda}{2\pi} \mathbf{s}$. The scaled definition of $\hat{\mathbf{s}}$ is the difference between two vectors on the unit 2-sphere. We know that this space can be defined as the 3-ball of radius 2, i.e., $\hat{\mathbf{s}} \in \mathbb{R}^3 : |\hat{\mathbf{s}}| \leq 2$. The condition that $|\hat{\mathbf{s}}| \leq 2$ is true even if we restrict the elevation angles by not allowing elevations below 0° . We then split $\hat{\mathbf{s}}$ into two components:

$$\hat{\mathbf{s}} = \hat{\mathbf{s}}_{\perp} + \hat{\mathbf{s}}_{\parallel}, \langle \hat{\mathbf{s}}_{\perp}, \hat{\mathbf{r}}_j \rangle = 0, \langle \hat{\mathbf{s}}_{\parallel}, \hat{\mathbf{r}}_j \rangle = \cos(\alpha) |\hat{\mathbf{s}}_{\parallel}| |\hat{\mathbf{r}}_j|, \quad (10)$$

where $\alpha \in \{0^\circ, 180^\circ\}$. Inserting this split into Equation (9) gives $\langle \hat{\mathbf{r}}_j, \hat{\mathbf{s}}_{\perp} + \hat{\mathbf{s}}_{\parallel} \rangle = \langle \hat{\mathbf{r}}_j, \hat{\mathbf{s}}_{\parallel} \rangle = \pm |\hat{\mathbf{s}}_{\parallel}| |\hat{\mathbf{r}}_j|$.

We then define a function $f_j(s) = s |\hat{\mathbf{r}}_j|$, where $s = \frac{\langle \hat{\mathbf{r}}_j, \hat{\mathbf{s}}_{\parallel} \rangle}{|\langle \hat{\mathbf{r}}_j, \hat{\mathbf{s}}_{\parallel} \rangle|} |\hat{\mathbf{s}}_{\parallel}|$.

Since $|\hat{\mathbf{s}}| \leq 2$, we may assume that s can take on all values $-2 \geq s \geq 2$, thus f_j is also smooth.

As f_j is smooth, the integer solutions to f_j are all integers between and including the maximum and minimum integer value of the function. These limiting integers are $f_j^{\max} = \left\lfloor 2 |\hat{\mathbf{r}}_j| \right\rfloor$ and $f_j^{\min} = - \left\lfloor 2 |\hat{\mathbf{r}}_j| \right\rfloor$. Since f_j is linear, all integer solutions are given by

$$s_k = \frac{k}{|\hat{\mathbf{r}}_j|} \quad \forall f_j^{\min} \leq k \leq f_j^{\max}, k \in \mathbb{Z}, \quad (11)$$

i.e., $f_j(s_k) = k$. As only the magnitude of the parallel component $\hat{\mathbf{s}}_{\parallel}$ is varied, $\hat{\mathbf{s}}_{\perp}$ is arbitrary while still returning the same integer value from f_j , as long as $|\hat{\mathbf{s}}| \leq 2$. As such, the integer solutions to Equation (9) form circular plane sections, or disks, of the form

$$\hat{\mathbf{s}} = \hat{\mathbf{s}}_{\perp} + \frac{k}{|\hat{\mathbf{r}}_j|} \hat{\mathbf{r}}_j \quad \forall \hat{\mathbf{s}}_{\perp} \in \mathbb{R}^3 : |\hat{\mathbf{s}}| \leq 2, f_j^{\min} \leq k \leq f_j^{\max}, k \in \mathbb{Z}. \quad (12)$$

For each k , we have a different disk where all $\hat{\mathbf{s}}$ vectors in that disk give an integer response, k , when input into f_j . These disks are all parallel, as they have the same normal vector, $\frac{\hat{\mathbf{r}}_j}{|\hat{\mathbf{r}}_j|}$, and they are not the same disk, since the displacement points, $\frac{k}{|\hat{\mathbf{r}}_j|} \hat{\mathbf{r}}_j$, along this normal are different.

Equation (12) describes the solution for one sensor, but for Equation (8) to have an N -dimensional integer output, all f_j 's must simultaneously output integers. This is only true where the disks of integer solutions all intersect at the same point. All integer solutions to Equation (8) are therefore found by taking the union over all the disks

describing integer solutions for one sensor, i.e., $\bigcup_{k=f_j^{\min}}^{f_j^{\max}} \mathbb{P}_{jk}$

The N -dimensional integer solution is then formed by all intersections between sensor solutions, i.e., the N sets of disks $\bigcap_{j=1}^N$.

An example illustration of disks of integer solutions and their intersections is shown in Figure 1.

3.2 Numerical Ambiguity Set

The advantage of using the viewpoint of plane intersections is that it can reduce the numerical algorithm to an algorithm that is often efficient. We first manipulate the result from Theorem 1 by using the property that set intersection is distributive over set union, i.e., $A \cap (S \cup T) = (A \cap S) \cup (A \cap T)$ for all sets A, S, T . Any two subsequent intersections, j and $j+1$, can then be written as

$$\begin{aligned} & \left(\bigcup_{k=f_j^{\min}}^{f_j^{\max}} \mathbb{P}_{jk} \right) \cap \left(\bigcup_{l=f_{j+1}^{\min}}^{f_{j+1}^{\max}} \mathbb{P}_{j+1l} \right) \\ &= \bigcup_{k=f_j^{\min}}^{f_j^{\max}} \bigcup_{l=f_{j+1}^{\min}}^{f_{j+1}^{\max}} \mathbb{P}_{jk} \cap \mathbb{P}_{j+1l}, \end{aligned} \quad (13)$$

and the set Ω can be rewritten as

$$\Omega = \bigcap_{j=1}^N \left(\bigcup_{k=f_j^{\min}}^{f_j^{\max}} \mathbb{P}_{jk} \right) = \bigcup_{k_1=f_1^{\min}}^{f_1^{\max}} \dots \bigcup_{k_N=f_N^{\min}}^{f_N^{\max}} \bigcap_{j=1}^N \mathbb{P}_{jk_j}. \quad (14)$$

Calculating all the terms $\bigcap_{j=1}^N \mathbb{P}_{jk_j}$ is impractical since it would require an N -plane intersection calculation for $\prod_{j=1}^N (f_j^{\max} - f_j^{\min})$ permutations.

For example, if $f_j^{\max} - f_j^{\min} = 5$ and $N = 25$, we would have $5^{25} \approx 3 \times 10^{17}$ permutations. However, for any set A , $\emptyset \cap A = \emptyset$. If any pair within $\mathbb{P}_{1k_1} \cap \dots \cap \mathbb{P}_{Nk_N}$ is the empty set, that entire term will thus be the empty set. We also know that for any set A , $\emptyset \cup A = A$. Every term containing two planes not intersecting can therefore be disregarded.

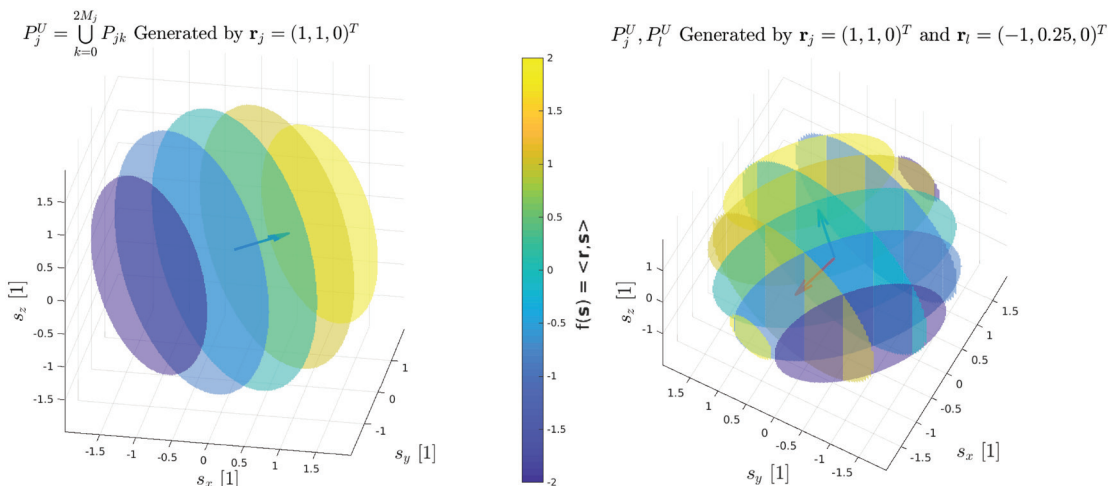


Figure 1. (l) The disks giving integer solutions to the equation $f(\hat{\mathbf{s}}) = \langle (1, 1, 0)^T, \hat{\mathbf{s}} \rangle$. The integers range between $\lfloor 2 \langle (1, 1, 0)^T, \hat{\mathbf{s}} \rangle \rfloor = \lfloor 2\sqrt{2} \rfloor = 2$ and $\lceil -2 \langle (1, 1, 0)^T, \hat{\mathbf{s}} \rangle \rceil = \lceil -2\sqrt{2} \rceil = -2$. **(r)** Intersections between two different sets of disks.

We will take advantage of the above-described property to exclude unnecessary calculations. To perform this exclusion, first define an N_J plane intersection as

$$\mathcal{I}_J = \bigcap_{j=1}^{N_J} \mathbb{P}_{Jk_j} \text{ where } J \text{ is an indexing set. } J \text{ is defined}$$

as $J = \{f_j^{\min} \leq k_j \leq f_j^{\max} : 1 \leq j \leq N_J, j \in \mathbb{Z}, k_j \in \mathbb{Z}\}$, i.e., a set

of N_J integer solutions for the first 1 through N_J sensors. \mathcal{I}_J can thus describe all terms and partial terms, where a full term is described by $N_J = N$. The intersection \mathcal{I}_J can be calculated with linear algebra by

$$\mathcal{I}_J = \left\{ \mathbf{s} \in \mathbb{R}^3 : W_J \mathbf{s} = \mathbf{b}_J \right\}, \quad (15)$$

where

$$W_J = \begin{pmatrix} \mathbf{n}_1^T \\ \mathbf{n}_2^T \\ \vdots \\ \mathbf{n}_{N_J}^T \end{pmatrix}, \mathbf{b}_J = \begin{pmatrix} -\langle \mathbf{n}_1, \mathbf{p}_{1k_1} \rangle \\ \vdots \\ -\langle \mathbf{n}_{N_J}, \mathbf{p}_{N_J k_{N_J}} \rangle \end{pmatrix}. \quad (16)$$

Here, the matrix W_J is of size $N_J \times 3$, i.e., the same number of rows as the number of intersecting planes. The vector $\mathbf{b}_J \in \mathbb{R}^{N_J}$ and the vectors \mathbf{n} and \mathbf{p} are defined as in Theorem 1. Since the matrix W_J is generally not square, to find the solution for \mathbf{s} we used the Moore-Penrose inverse. This inverse is denoted M^+ for the matrix M , and has been numerically implemented by using singular value decomposition. The output of applying the inverse M^+ on a input vector is a unique least-square fit to the set of linear equations. This method always thus outputs a solution regardless of whether a solution exists. Important for implementation is that this also implies that the numerical Moore-Penrose inverse always returns a point, even if the true solution is a set of points. For example, if the solution is a plane or a line, the numerical method will only return a point on this plane or line. This is compensated for in the implementation by examining the span of the intersecting planes' normal vectors. Due to the behavior of the numerical Moore-Penrose inverse, it is most practical not to directly calculate all the solutions, \mathbf{s} , in the algorithmic implementation. Instead, we only check for the existence of a solution, as this is all the information required in the iteration. The extraction of the solution set in terms of \mathbf{s} 's can then be handled after the algorithm completes. To check if $W_J \mathbf{s} = \mathbf{b}_J$ has solutions, we check the norm divergence of the solution, i.e., a solution exists if

$$\left| W_J W_J^+ \mathbf{b}_J - \mathbf{b}_J \right| < T, \quad (17)$$

where T denotes a tolerance for error. With this we construct an algorithm, assuming that $N \geq 3$, to evaluate all intersection terms, excluding terms we know will equal \emptyset in future calculations:

- For all permutations of k_1, k_2 so that

$$k_1 \in [f_1^{\min}, f_1^{\max}], k_2 \in [f_2^{\min}, f_2^{\max}]:$$

- Define J as $\{k_1, k_2\}$

- If $\left| W_J W_J^+ \mathbf{b}_J - \mathbf{b}_J \right| < T$ then save the indices k_1, k_2 in a list

- The list L_2 has length K_2 and describes all intersections for sensors 1 and 2

- For the remaining sensors perform the following loop with variable $3 \leq j \leq N$:

- Using all saved sets of k_1, \dots, k_{j-1} forming a list L_{j-1} of length K_{j-1} , create a new list of size on the form k_1, k_2, \dots, k_j where $k_j \in [f_j^{\min}, f_j^{\max}]$

- For each entry in the list:

* Define J as $\{k_1, k_2, \dots, k_j\}$

* If $\left| W_J W_J^+ \mathbf{b}_J - \mathbf{b}_J \right| < T$ then save the indices $k_1, k_2, \dots, k_{N-1}, k_N$ in a list L_j

- The last list L_N of saved index sets $k_1, k_2, \dots, k_{N-1}, k_N$ identifies all the solutions

Upon completion of the algorithm, we can give a numerical form of Ω , i.e., solutions to Equation (8), as

$$\Omega = \left\{ W_J^+ \mathbf{b}_J : J \in L_N \right\}, \quad (18)$$

where we then consider the situation of each Moore-Penrose inverse solution and extend the set appropriately, e.g., in the event of solutions being lines or planes.

If there are no common intersections, this algorithm can complete in $\prod_{j=1}^2 (f_j^{\max} - f_j^{\min})$ calculations. If there are common intersections, the algorithm is bounded below by

$$\prod_{j=1}^2 (f_j^{\max} - f_j^{\min}) + \sum_{j=3}^N (f_j^{\max} - f_j^{\min})$$

and above by

$$\prod_{j=1}^N (f_j^{\max} - f_j^{\min}).$$

In implementation, if one sensor position is defined as the origin, this has to be accounted for in the algorithm.

3.3 Ambiguities to DOAs

In the beginning of Section 3.1, the solution was split into two steps. The first step covered solving both analytically and numerically for a solution set to Equation (8). The second step consisted of converting the solutions from the space of \mathbf{s} to directions of arrival. There are two options: either find all $\mathbf{k}_1, \mathbf{k}_2$ that can compose $\mathbf{s} = \mathbf{k}_1 - \mathbf{k}_2$, or fix one wave vector \mathbf{k}_0 in $\mathbf{s}_0 = \mathbf{k}_0 - \mathbf{k}$. The first method will lead to a set of ambiguity pairs, $(\mathbf{k}_1, \mathbf{k}_2)$, while the second method will give a set of ambiguities for a fixed direction of arrival. As the second option is a more practical representation, this is our method of choice.

To find the set of ambiguities, first fix a direction of arrival, \mathbf{k}_0 , and then find all possible vectors $\mathbf{s}_0 = \mathbf{k}_0 - \mathbf{k}$. For example, if we consider only the wave vectors coming from above the horizon, all possible \mathbf{s}_0 will form a southern hemisphere centered at the chosen \mathbf{k}_0 . As all solutions Ω for Equation (8) are known from Theorem 1, all points on this surface \mathbf{s}_0 that coincide with Ω represent a distinct ambiguity for \mathbf{k}_0 . This set of ambiguities is defined as

$$\Omega(\mathbf{k}_0) = \{\mathbf{s}_0 \in \Omega : \mathbf{s}_0 = \mathbf{k}_0 - \mathbf{k} \forall \mathbf{k}\}. \quad (19)$$

As a practical example, we have taken the sensor configuration for the MU-radar in Japan [3] and calculated all ambiguities. Figures 2-4 show an illustration of the algorithm. Figure 2 shows the MU-radar sensor and antenna configuration. Figure 3 displays the solution set Ω , obtained by running the algorithm in Section 3.2. Figure 4 illustrates the plane intersections generating the red line highlighted in Figure 3. The tolerance was set to $T = 0.1$, and the title of Figure 4 shows the integer solution for this ambiguity, defined as $RW_J^+ \mathbf{b}_J = \mathbf{I}$. \mathbf{I} is not a perfect integer solution, but close enough to create an *approximate* ambiguity. This effect will be discussed further in the next section.

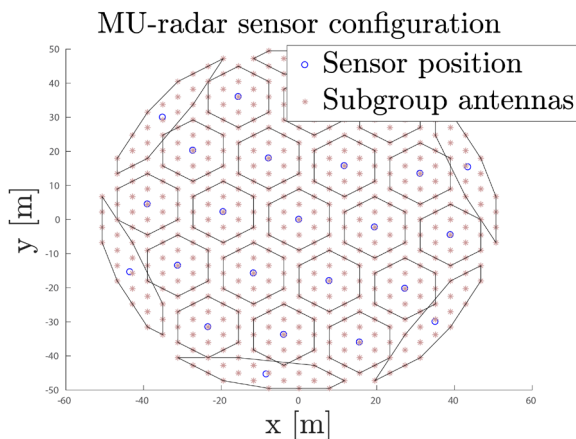


Figure 2. The MU-radar configuration. This is the input to the algorithm in Section 3.2, together with a tolerance

To validate the predicted ambiguities and as an example, we picked a direction of arrival, azimuth 120° and elevation 77.5° , as \mathbf{k}_0 , and found all intersections between the possible \mathbf{s}_0 's and solutions in Ω giving the set $\Omega(\mathbf{k}_0)$. Alongside the predicted ambiguities, the distance in \mathbb{C}^N between the sensor-response model for \mathbf{k}_0 and for all other \mathbf{k} 's were then calculated. This result is illustrated in Figure 5. The contours indicated local minima in distance ranging from 1 to 4. The rest of the direction-of-arrival space in the figure had an almost constant distance of 8. As seen in the figure, all predicted ambiguities (red crosses) resided at local minima. The prediction therefore held, even for approximate ambiguities (red crosses) resided at local minima. The prediction therefore held, even for approximate ambiguities.

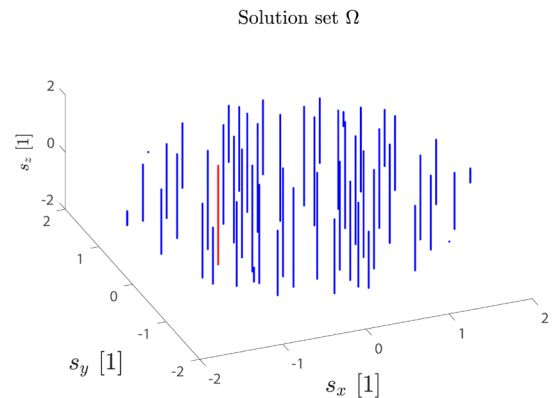


Figure 3. The solution set Ω from the algorithm in Section 3.2 when the MU-radar configuration from Figure 2 and a tolerance of $T = 0.1$ was used. The solutions marked in red were further explored in Figure 4.

$$\mathbf{I} = [-1.88, -1.03, -4.03, -2.01, -6.95, -5.01, -6.00, -3.00, -5.07, -3.98, -1.97, -0.98, 1.88, 1.03, 4.03, 2.01, 6.95, 5.01, 6.00, 3.00, 5.07, 3.98, 1.97, 0.98] \mu_{err} = 0.03$$

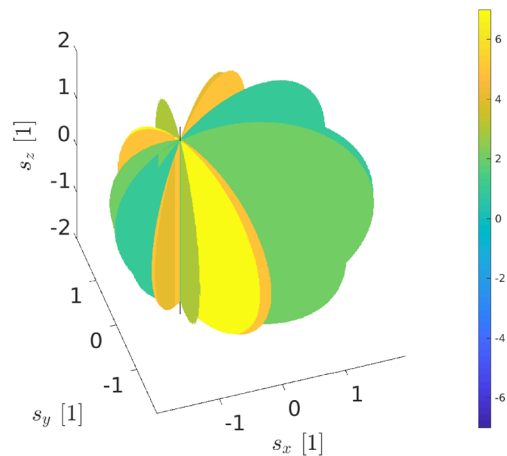


Figure 4. The plane intersections generating the red line highlighted in Figure 3. The title shows $RW_J^+ \mathbf{b}_J = \mathbf{I}$ and $\mu_{err} = \frac{1}{N} \sum_{i=1}^N |I_i - \text{round}(I_i)|$.

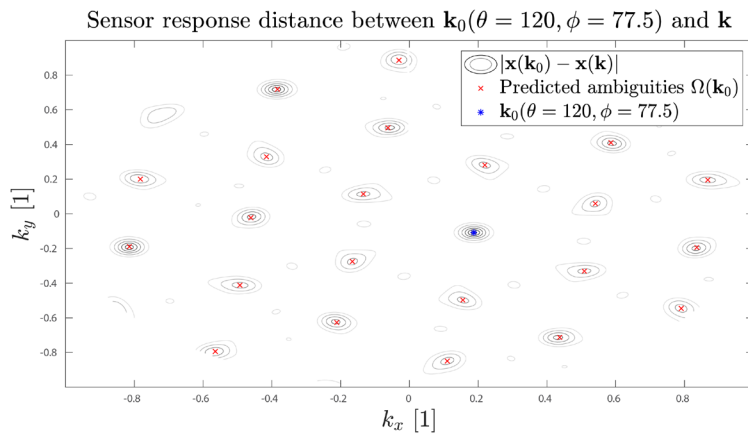


Figure 5. The red crosses indicate the set of ambiguities defined in Equation (19) for $\mathbf{k}_0(\theta = 120^\circ, \phi = 77.5^\circ)$, which is represented by the blue star. The contours show the distance in \mathbb{C}^N space between the sensor-response model for \mathbf{k}_0 and all other \mathbf{k} 's, i.e., $|\mathbf{x}(\mathbf{k}_0) - \mathbf{x}(\mathbf{k})|$. The contours indicate local minima in distance, ranging from 1 to 4. The rest of the direction-of-arrival space in the figure has an almost constant distance of 8. All predicted ambiguities reside at local minima.

4. Model-Matching Algorithms

The sensor-response model allows for model-matching algorithms to be applied. These algorithms usually try to minimize a distance between a detected signal, a point in \mathbb{C}^N , and the sensor-response space modeled by $\mathbf{x}(\mathbf{k}) \forall \mathbf{k}$. We discuss here some of the implications of our results for such algorithms.

4.1 Noise-Induced Ambiguity

When applying model-matching algorithms, two types of noise-induced ambiguities were discovered. The first kind is generated by the sensor-response model having approximately the same response for several very different waves. When these responses are similar, the noise can perturb the signal from one response to another, leading to misclassification of the direction of arrival. The fact that the responses are similar where a predicted ambiguity resides is illustrated in Figure 5. In this figure, none of the local minima reached zero since no intersections in Ω remained when the tolerance, T , was decreased towards the numerical accuracy of the computation. The MU-radar thus has no

theoretical ambiguities. There still are yet approximate ambiguities when $T = 0.1$, which is close enough for the noise to cause misclassifications. The second kind of noise-induced ambiguity is also due to noise perturbing the signal out from the model space. In this case, since the topology of the sensor-response space is nontrivial, such a perturbation may create many different “best matches,” none of which is representative of the original direction of arrival. This perturbation accounts for very small errors in direction of arrival when compared to the first kind of noise-induced ambiguity covered.

When analyzing a signal, it is impossible to disentangle noise-induced ambiguities, as we can only predict statistics of noise, not the specific values. However, if there are several measurements and the noise distribution is known, examining a distribution of directions of arrival can indicate what the true direction of arrival is. Using this knowledge, the trajectory calculation can be improved. For example, one can create better outlier analysis or achieve better statistics by moving outliers that are generated by ambiguities to their correct positions. The fitting process can also be improved when accounting for the sensor-response space topology.

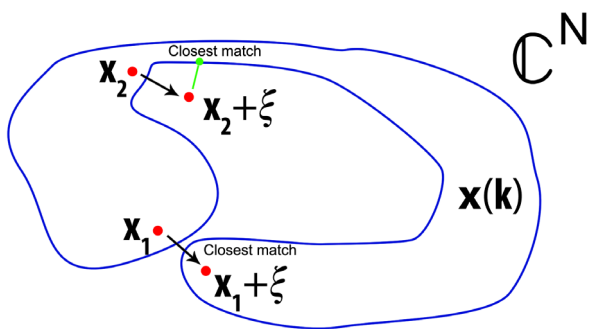


Figure 6. The geometrical interpretation of noise-induced ambiguities. The top example illustrates a non-perfect match in a closest-distance search. The bottom example illustrates the ambiguity introduced by noise in ambiguity-free antennas that have an approximate self-intersection.

Both types of noise-induced ambiguities are illustrated in Figure 6. The illustration does not do justice to the difference in size between \mathbb{C}^N and the sensor-response space generated by $\mathbf{x}(\mathbf{k})$, but it shows the situation that can occur due to perturbation. In the figure, \mathbf{x}_1 and \mathbf{x}_2 are detected signals, and ξ is the noise.

5. Resolving Ambiguities

Resolving ambiguities is generally impossible without additional information. Such additional information is possibly available in the form of gain patterns, if we are dealing with high-power large-aperture radars. These types of radars usually combine several antennas distributed in space into one single signal. We call these groups of antennas sub-arrays. How a sub-array responds to an electromagnetic plane wave when the signal from each antenna is summed is called the ideal gain pattern for the sub-array or sensor.

Input: gain modulated signal model
 Map: Difference between MUSIC result with and without gain

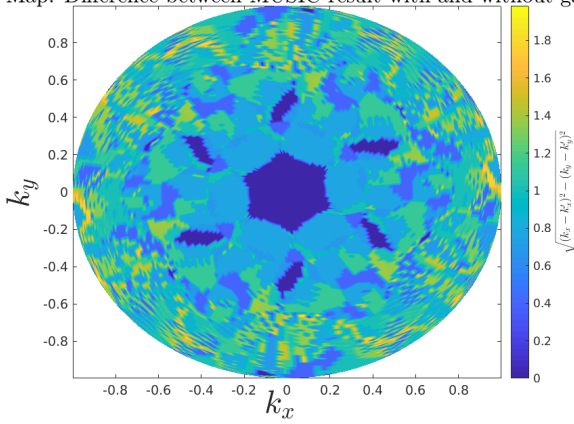


Figure 7. A synthetic signal generated using Equation (22). The first MUSIC algorithm, with output \mathbf{k} , used Equation (4) as a model, and the second MUSIC algorithm, with output \mathbf{k}' , used Equation (22). The color shows the magnitude of the plane-projected distance, $\sqrt{(k_x - k_{x'})^2 + (k_y - k_{y'})^2}$, between the two MUSIC-algorithm outputs.

5.1 Sub-Array Gain Pattern

The sub-array ideal gain pattern is defined as

$$\mathbf{r}_{jk} = \mathbf{h}_{jk} - \mathbf{r}_j, \quad (20)$$

$$\gamma_j(\mathbf{k}) = Y(\mathbf{k}) \sum_{k=1}^{n_j} e^{-i\langle \mathbf{k}, \mathbf{r}_{jk} \rangle_{\mathbb{R}^3}}, \quad (21)$$

where Y is the individual antenna's gain pattern, assuming all antennas are the same. This definition is directly derived from the geometric-center approximation. Modifying the sensor-response model in Equation (4) to account for the sensor-gain pattern, we get

$$\mathbf{y}(\mathbf{k}) = \gamma(\mathbf{k}) \odot \mathbf{x}(\mathbf{k}) = \gamma_j(\mathbf{k}) \Psi(\mathbf{r}_j, t, \mathbf{k}), \quad (22)$$

where \odot denotes the Hadamard product, or element-wise multiplication. This new sensor-response model will not have the same ambiguities as the function in Equation (4). If we apply the injective definition in Equation (5), we find

$$R(\mathbf{k}_2 - \mathbf{k}_1) = 2\pi\mathbf{I} - i\beta, \text{ where } \beta_j = \ln \left[\frac{\gamma_j(\mathbf{k}_2)}{\gamma_j(\mathbf{k}_1)} \right],$$

which to our knowledge has no simplification or efficient numerical solution. It is thus not feasible to replace the sensor-response model and repeat the work done in Section 3 for the new problem.

5.2 Using Gain to Resolve Ambiguities

Since it is impractical to solve for all ambiguities generated by Equation (22), we instead use gain alongside the model in Equation (4). To determine how well gain can resolve ambiguities, we swept \mathbf{k}_0 for all directions of arrival above the horizon. For each ambiguity in $\Omega(\mathbf{k}_0)$, we checked if the gain pattern could differentiate between the ambiguities. Having done this for the MU-radar configuration, as shown in Figure 2, we found that the closer to zenith the source signal \mathbf{k}_0 was, the better did the gain pattern differentiate between the ambiguities. If a signal originated near zenith, one should thus be able to use the gain pattern to distinguish between ambiguities. However, as gain is not a separate piece of information but embedded in the signal, it is difficult to practically use this information.

By instead using gain only to restrict the elevation of the signal, this information can be used. We found that for the MU-radar, the sensor-response models in Equation (4) and in Equation (22) converged in zenith. However, they substantially diverged with decreasing elevation. We also found that the distance between \mathbf{k}_0 and the ambiguities in $\Omega(\mathbf{k}_0)$ was far in direction of arrival space. This indicated a property that can be used to distinguish between a close-to-zenith detection and a far-from-zenith detection.

To test the above hypothesis, we used the model-matching algorithm MUSIC [2]. A signal was generated using Equation (22). Two MUSIC algorithms were then applied to this synthetic signal. The first MUSIC algorithm used Equation (4) as a model with output \mathbf{k} . The second MUSIC algorithm used Equation (22) as a model with output \mathbf{k}' . These two algorithms should have output different results if the two sensor-response models differed enough so that the closest match changed. The resulting map is displayed in Figure 7, where the color map shows the magnitude of the plane projected distance between the two results, $\sqrt{(k_x - k_{x'})^2 + (k_y - k_{y'})^2}$. Below $\approx 80^\circ$ elevation, the two algorithms started producing very different results, except in certain sidelobes where the result was again identical.

The test showed that if these two MUSIC algorithms were run on a detected signal and the results did not differ, the signal probably had a direction of arrival with elevation $> 80^\circ$. This shifting effect was true regardless if noise perturbed the signal from \mathbf{k}_0 to a direction of arrival from $\Omega(\mathbf{k}_0)$, as the modulation by the gain had not changed. These are the first steps toward a practical method to resolve ambiguities.

6. Conclusions

We have derived a theoretical representation of all direction-of-arrival ambiguities present in any multi-channel radar system. We have also developed a numerical algorithm that can calculate theoretical ambiguities and approximate ambiguities on a personal computer. We have found ambiguities that can originate from noise in otherwise ambiguity-free radar systems. The methods can be used to optimize new sensor configurations, as they provide both an exact identification of ambiguities given a sensor configuration and a measure of how close the configuration is to forming new ambiguities. We have started development towards a method to use the additional information of sub-array gain patterns to resolve ambiguities in model-matching algorithms. Together with statistical information, this information can be used to improve trajectory estimation, identify faulty direction-of-arrival calculations, and correct them.

7. Acknowledgements

The MU radar belongs to and is operated by the Research Institute of Sustainable Humanosphere, Kyoto University, Japan.

8. References

1. L. Godara and A. Cantoni, "Uniqueness and Linear Independence of Steering Vectors in Array Space," *The Journal of the Acoustical Society of America*, **70**, 2, August 1981, pp. 467-475.
2. R. Schmidt, "Multiple Emitter Location and Signal Parameter Estimation," *IEEE Transactions on Antennas and Propagation*, **34**, 3, 1986, pp. 276-280.
3. J. Kero, C. Szasz, T. Nakamura, T. Terasawa, H. Miyamoto, and K. Nishimura, "A Meteor Head Echo Analysis Algorithm for the Lower VHF Band," *Annales Geophysicae*, **30**, 4, 2012, pp. 639-659.
4. J. Jones, A. R. Webster, and W. K. Hocking, "An Improved Interferometer Design for Use with Meteor Radars," *Radio Science*, **33**, 1998, pp. 55-65.
5. W. K. Hocking, B. Fuller, and B. Vandeppeer, "Real-Time Determination of Meteor-Related Parameters Utilizing Modern Digital Technology," *Journal of Atmospheric and Solar-Terrestrial Physics*, **63**, 2001, pp. 155-169.
6. D. Kastinen and J. Kero, "A Monte Carlo-Type Simulation Toolbox for Solar System Small Body Dynamics: Application to the October Draconids," *Planetary and Space Science*, **143**, 2017, pp. 53-66.
7. Kah-Chye Tan, Say Song Goh, and Eng-Chye Tan, "A Study of the Rank-Ambiguity Issues in Direction-of-Arrival Estimation," *IEEE Transactions on Signal Processing*, **44**, 4, 1996, pp. 880-887.
8. H. Gazzah and K. Abed-Meraim, "Optimum Ambiguity-Free Directional and Omnidirectional Planar Antenna Arrays for DOA Estimation," *IEEE Transactions on Signal Processing*, **57**, 10, 2009, pp. 3942-3953.
9. B. Gao and J. Mathews, High-Altitude Radar Meteors Observed at Jicamarca Radio Observatory Using a Multibaseline Interferometric Technique. *Monthly Notices of the Royal Astronomical Society*, **452**, 4, 2015, pp. 4252-4262.

Design of a Narrow-band Single-Layer Chipless RFID Tag

*Ricardo Figueiredo^{1,2}, João Louro¹, Samuel Pereira^{1,2}, João Gonçalves¹,
and Nuno Borges Carvalho^{1,2}*

¹Universidade de Aveiro
Campus Universitário de Santiago
3810-193 Aveiro, Portugal
E-mail: ricardofigueiredo@ua.pt

²Instituto de Telecomunicações
3810-193 Aveiro, Portugal

Abstract

This paper presents the design of a narrowband single-layer chipless RFID tag. The design is based on a coplanar stripline C-section resonator with three-bit coding capacity.

1. Introduction

R RFID technology takes advantage of the radar principle for communication purposes. The radar principle can be stated in the following way: an electromagnetic (EM) wave incident on a conducting object will be reflected in accordance with the reflection coefficient that the conducting object presents to the traveling EM wave.

At its core, an RFID tag consists of an active device that dynamically changes the reflection coefficient of the reflecting object (the tag), changing the energy levels of the reflected electromagnetic wave. This change in energy level codes a bit, either as a logic “1” or a logic “0.” The bit can be detected by a nearby reader, thus establishing communication between the tag and reader.

Passive RFID tags also contain a power harvester to collect energy from the incident EM wave, to both power the tag’s active device and the reflected signal. This is called backscatter communication. This allows devices to operate without a battery, which is especially useful when a device doesn’t need to be in constant operation. This is the case for some sensors that perform periodic measurements, or when a device is in a place where battery replacement is impossible or complicated, as is the case for spatial applications.

The demand for passive RFID tags is ever-increasing with the rise of the Internet of Things (IoT). Such tags are seen as a green solution that greatly reduces the number of batteries and the power consumption required to build the envisioned IoT [1, 2]. Another advantage is the cost reduction compared with battery-powered solutions.

In chipless RFID technology, there are no active devices: only passive components are used. A resonator structure is designed so that a specific static electromagnetic signature (EMS) is coded into the reflected signal. This electromagnetic signature uniquely identifies the chipless RFID tag.

There are several techniques to encode an electromagnetic signature. Those most used are time-, phase-, and frequency-encoding techniques. In time-encoding techniques, a structure is designed including one or several delay lines that introduce specific temporal delays into the received signal. When the received signal is retransmitted with the temporal delays, these delays identify the tag. In phase-encoding techniques, the resonator structure is designed to introduce phase shifts onto the incident EM wave at specific frequencies. These phase shifts identify the tag. In frequency-encoding techniques, the resonator structure acts as band-stop filters, resonating at some frequencies and attenuating others. This creates a specific characteristic EM spectrum, the transfer function, which uniquely identifies the tag.

Depending on the type of encoding, a reader can be implemented to detect time delays, phase shifts, or spectrum characteristics introduced by the chipless tag. The detection is greatly simplified by the fact that the signals are static, and averaging mechanisms and other techniques [3] can be used to detect the very-low-power signals transmitted by chipless tags. Tag identification is based on correlation with previously measured tag characteristics. Depending on the tag, environmental characterization measurements might or might not be needed [3, 4]. Traditionally, the metric used to characterize the performance of a tag is the radar cross section (RCS) [5, 8].

Based on the electromagnetic signature of frequency-encoded tags, a new concept has emerged: RF-encoding particles (REPs) [8]. This concept states that every structure has a unique electromagnetic signature that can

be determined and used for encoding, i.e., every structure can be used as an RF-encoding particle. In [6], this concept was applied to letters that were characterized and used for encoding.

It is possible to embed sensing capabilities in chipless tags by adding materials sensitive to environmental properties to the resonator structure [7]. In these tags, it is possible to separate the electromagnetic signature due to the resonator's structure and the electromagnetic signature due to the sensing material. This means that it is possible to identify the tag that is performing the measurements.

When compared with traditional chipped passive RFID, chipless RFID technology is a lower-complexity solution that doesn't require active devices nor power harvesting to operate. This makes it a greener solution [8], because it requires less power and fewer components to operate. The need for fewer components, allied with the possibility of mass production using flexography, also drastically reduces the cost of chipless RFID, which is considered extremely low-cost RFID [8]. This, allied with the sensing capabilities, reveals the high potential of this technology, making chipless RFID extremely desirable for IoT solutions.

A more extensive overview of chipless RFID technology was presented in [8]. The following sections of this paper present the design steps for a frequency-encoded narrowband three-bit single-layer chipless RFID tag, based on a coplanar stripline C-section resonator. This design contrasts with traditional chipless tag designs that typically are broadband and usually struggle to be FCC compliant [4].

2. Design

This section presents the steps followed to design the chipless tag. It starts with the theoretical considerations for the design of the C-section resonator, and continues with the computational design and simulation optimization using *CST Studio Suite 2017*. Experimental results are then presented. This section ends with an analysis of the results, comparing the simulation with experimental results, and comparing this tag design with state-of-the-art designs.

2.1 Theory

The basis for the tag design is a C-section resonator. This structure consists of a coplanar stripline terminated in an open circuit at one end, and terminated in a short circuit at the other end [4], as is depicted in Figure 1. The C-section resonates at a single frequency band. To obtain an initial estimate of the resonance frequency, the simulation model presented in [4] was used. This model, expressed in Equation (1), is only valid for the frequency band 2 GHz to 5.5 GHz, and was considered for fixed gap and line-width values. L represents the slot length.

$$f_r = \frac{c}{4(L + 2.3)\sqrt{\epsilon_{eff}}} \quad (1)$$

Because the aim was to design a tag to operate near the 900 MHz band, where backscatter communications are regulated, adjustments in the C-section were made by simulation to design a tag for the desired frequency band. Changing the length of the slot, L , coarsely adjusted the resonance frequency, while changing the length of the short circuit, L_s , finely adjusted the resonance frequency. The gap between lines, g , and the width of the lines, w , changed the bandwidth of the resonance peaks [9].

To produce multiple resonance peaks, multiple C-section resonators were used, as was presented in [9]. However, instead of using multiple C-sections to obtain abrupt phase changes, the multiple C-sections were used to produce multiple resonance peaks with lower bandwidth, due to the abrupt phase changes caused by the multiple C-section resonators. This aided the narrowband tag design.

Another aspect of the design that helped in obtaining a narrowband tag was the selection of a lower central frequency, 950 MHz, where 100 MHz was a technologically achievable bandwidth for the backscattered signal. This might help in obtaining FCC compliance.

In the presented design, the dielectric used was single layer FR-4, with a relative permittivity of 4.4, a height of 1.6 mm, and a copper thickness of 35 μm . The use of this low-cost dielectric made the cost of the tags insignificant.

2.2 Simulation

A C-section structure was designed in *CST Studio Suite 2017* based on Equation (1) for the resonant frequency of 2.45 GHz. The initial values of g and w were 0.5 mm and 3 mm, respectively, as used in [4].

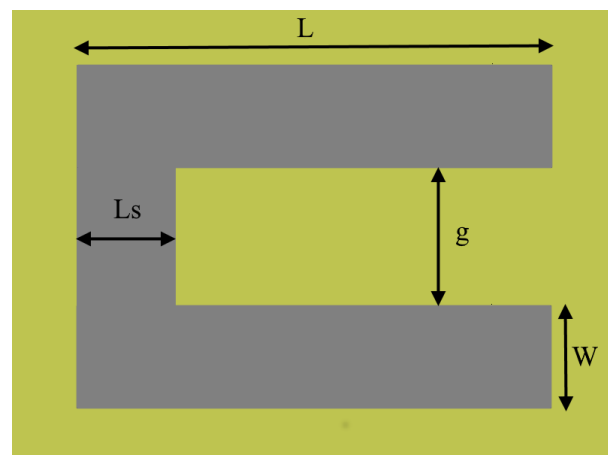


Figure 1. The C-section resonator.

Table 1. Optimum values for the narrowband resonance frequency centered at 950 MHz.

Parameter	Value [mm]
w	3
g	4.5
L	121

The length of the slot was then optimized to center the resonant frequency around 950 MHz. Afterward, g and w values were optimized to maximize the quality factor. The values of L , g , and w that centered the resonator around 950 MHz with narrower bandwidth are presented in Table 1.

The next step was to incorporate multiple C-sections on a single tag to obtain multiple resonance peaks. The distance between resonators was optimized to reduce coupling effects. The aim was to try to incorporate the maximum number of resonance peaks in a bandwidth of 50 MHz. After the first simulation results, it was considered reasonable to implement a system with three bits, i.e., three resonances, in a bandwidth of 60 MHz. The chosen resonance frequencies were 930 MHz, 950 MHz, and 980 MHz.

Table 2 shows short-circuit lengths, L_s , to center the resonance peaks at these frequencies. Figures 2 to 4 show the printed circuit board PCB layouts of the one-bit, two-bit, and three-bit tags. Figures 5 to 7 show the RCS simulation results of these tags.

Table 2. The short-circuit lengths for resonant frequencies at 920 MHz, 950 MHz, and 980 MHz.

Parameter	Value [mm]
L_{s920}	66.5
L_{s950}	68.3
L_{s980}	69.6

The simulation results led to the conclusion that it was possible to implement a chipless RFID system capable of coding three bits with a 60 MHz bandwidth centered around 950 MHz. The simulation results indicated that tag characterizations would be measurable, because between peaks there were at least 3 dB valleys.

2.3 Measurements

A monostatic RCS measurement setup was used to characterize the designed tags, as depicted in Figure 8. The vector network analyzer (VNA) used was Keysight's PNA-X network analyzer. The antenna used was a patch antenna centered around 880 MHz, the insertion loss of which is presented in Figure 9. The power transmitted by the vector network analyzer was 13.4 dBm. This high value was justified by the mismatch of the antenna used for the tags' operating frequency.



Figure 2. The one-bit tag printed circuit board: 920 MHz resonating frequency.

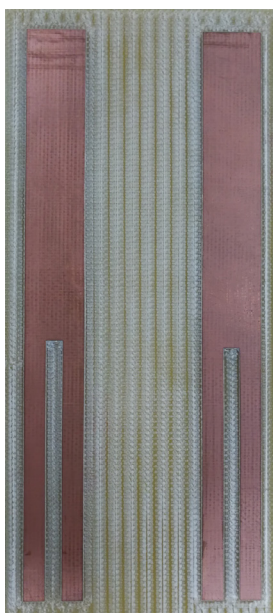


Figure 3. The two-bit tag printed circuit board: 920 MHz and 950 MHz resonating frequencies.

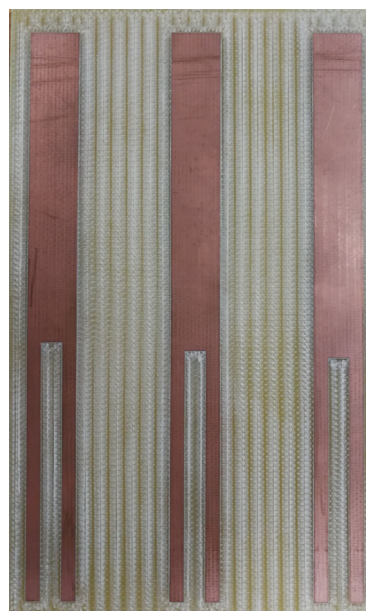


Figure 4. The three-bit tag printed circuit board: 920 MHz, 950 MHz, and 980 MHz resonating frequencies.

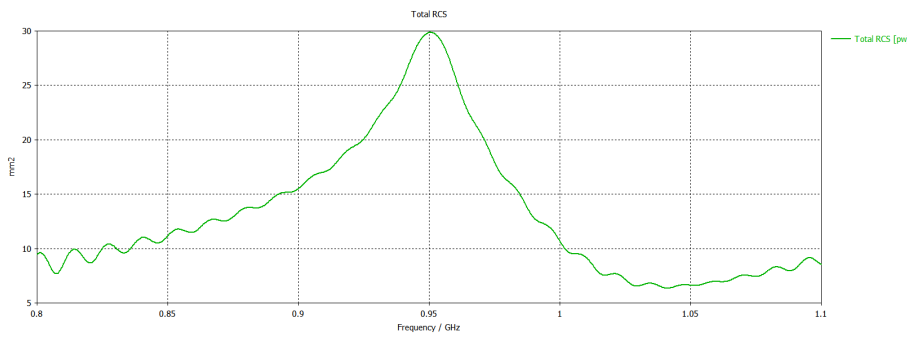


Figure 5. The one-bit tag’s radar cross section (RCS) simulation.

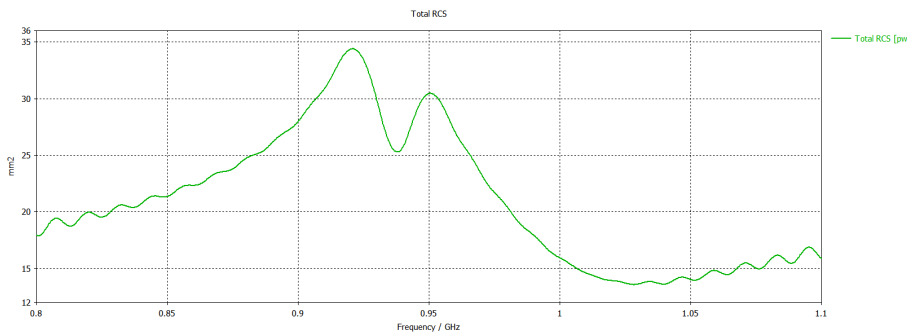


Figure 6. The two-bit tag’s radar cross section (RCS) simulation.

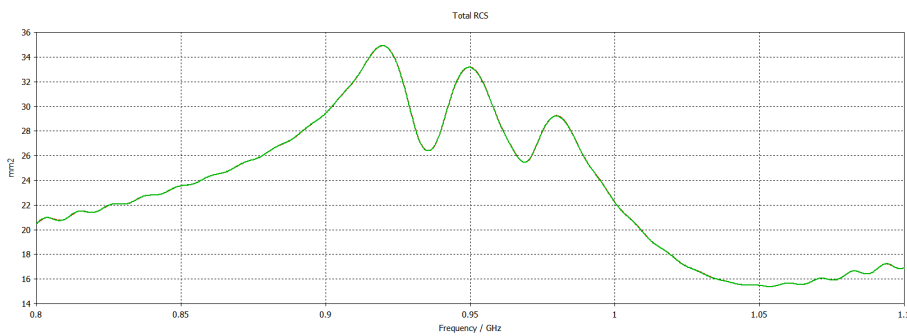


Figure 7. The three-bit tag’s radar cross section (RCS) simulation.

To extract the RCS from the S_{11} measurements, Equation (2) was used, which was based on Equation (5) from [4].

$$RCS_{tag} = \left[\frac{S_{11}^{tag} - S_{11}^{isolation}}{S_{11}^{reference} - S_{11}^{isolation}} \right]^2 RCS_{reference} \cdot (2)$$

The isolation measurement represented a measurement of the environment. The reference measurement represented a measurement of an object with known RCS: a metal plate was used, as described in [4]. This meant that both environmental and reference measurements were needed for calibration for characterizing these tags. The measurements were performed in a laboratory environment with the help of an absorbing background plane, to avoid multipath and the establishment of a standing wave, as depicted in Figure 10. The experimental results are presented in Figures 11, 12, and 13.

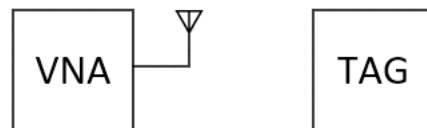


Figure 8. The monostatic radar cross section (RCS) measurement setup.

2.4 Performance Analysis

As can be seen in Figures 11-13, it was possible to characterize the designed tags. The correlation between measurements and simulation was high. The frequency shift when compared with simulation results was 5 MHz in a 950 MHz carrier, which corresponded to a shift of less than 1%. This confirmed that it was possible to design a three-bit chipless RFID tag with a bandwidth of 60 MHz centered at 950 MHz, and that the design method followed can be trusted to produce the expected results.

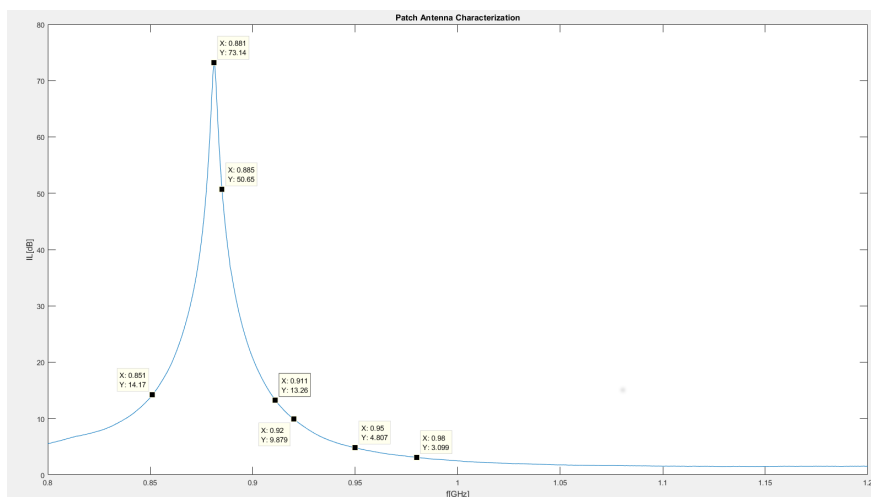


Figure 9. The patch antenna's insertion loss (IL).

As one can observe from Figure 9, the adaptation of the antenna used wasn't the best. However, it was the only directional antenna available in the lab operating around the selected frequency band. This caused some problems in the tag characterization, especially because more power needed to be transmitted by the PNA-X network analyzer to be able to characterize the tags. This was especially inconvenient in the measurement of the two-bit and three-bit tags where the received power out of band, near 920 MHz, was high due to antenna adaptation instead of an increase of reflected power. This slightly faded the evidence of the lower-frequency resonance, but the strong pattern of peak-valley, as described in [9], gave confidence that a resonance peak could be found at 920 MHz. More evidence of this was the measurement of the one-bit tag, where the absence of the 920 MHz resonance peak drastically changed the radar cross section (RCS) near that frequency band.

It should be observed that in between peaks and valleys, the measurement results always presented at least a 3 dB margin.

Some state-of-the-art tags were evaluated in terms of spatial and spectral efficiency in Figure 22 of [4]. In that figure, the most spatially efficient tag was capable of coding 3 bits/cm², while the most spectrally efficient tag was capable of coding 25 bits/GHz. The tags presented in this paper were capable of coding 0.028 bits/cm² and 50 bits/GHz. This meant that while the presented design was much larger than the state-of-the-art design, it could use spectrum more efficiently. This might be helpful, especially in implementing lower-complexity reading systems, which are the most complex part of implementing a chipless RFID system. Another advantage might relate to the ease of obtaining FCC compliance to approve future chipless RFID applications.



Figure 10. The experimental setup.

3. Future Work

In the future, it is important to characterize the tags using a better measuring antenna, and to repeat the process in an anechoic-chamber environment. The characterization in an anechoic chamber will allow for a better characterization, which then can be used to detect the tags in real-world environments without the need for environmental and reference measurements [3].

Another topic of investigation is different types of resonators. The focus of this investigation would be how other resonating structures could help in the miniaturization of the designed tags. The aim would be to achieve spatial efficiencies comparable with those presented in state-of-the-art tags, such as those in Figure 22 of [4], while maintaining the spectral efficiency of the presented design.

Another path of future investigation will focus on how can the use of narrowband chipless RFID tags simplify the reader architecture of chipless RFID systems.

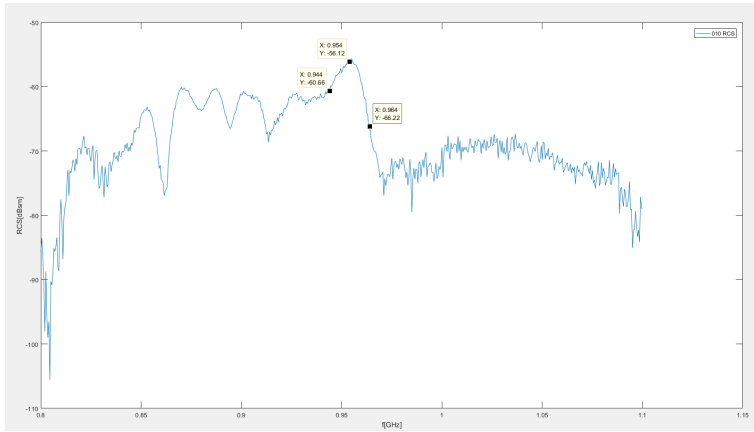


Figure 11. The one-bit tag's radar cross section (RCS) measurement.

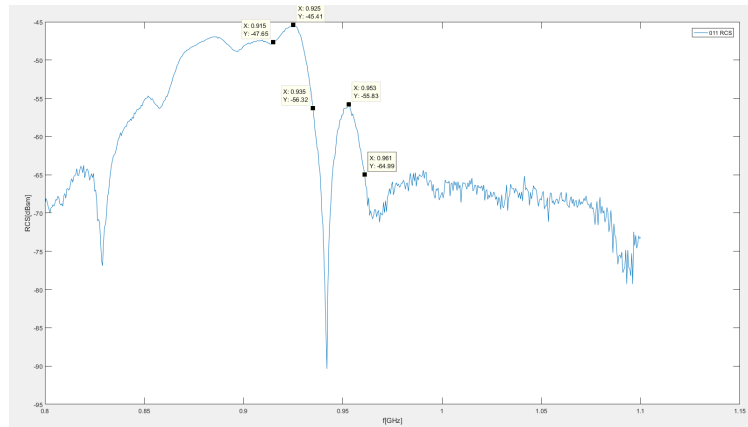


Figure 12. The two-bit tag's radar cross section (RCS) measurement.

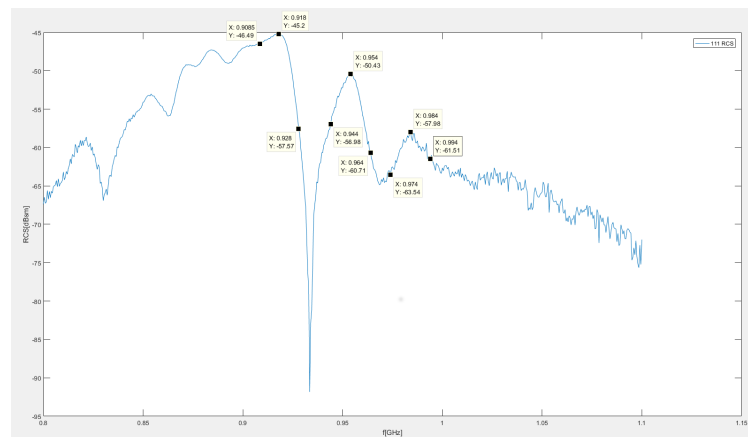


Figure 13. The three-bit tag's radar cross section (RCS) measurement.

4. Conclusion

In the work presented, a narrowband three-bit single-layer tag, based on C-section resonators, was proposed, simulated, and measured. The measurements validated the design.

It was proven that it was possible to realize all three bits of the logic system by demonstrating that both one-bit, two-bit, and three-bit simulation designs correlated with practical measurements.

The design presented is suitable for mass production using flexography because it is a single-layer design.

This design also had impressive spectral efficiency when compared to state-of-the-art designs. However, size reduction is extremely desirable, since the design had poor spatial efficiency.

5. Acknowledgements

This work was funded by FCT/MEC through national funds, and when applicable co-funded by the FEDER – PT2020 partnership agreement under the project UID/EEA/50008/2013

6. References

1. M. Friedli, L. Kaufmann, F. Paganini, and R. Kyburz, "Energy Efficiency of the Internet of Things: Technology and Energy Assessment Report," IEA 4E EDNA, April 2016.
2. Silicon Labs, "Battery Size Matters, Five Fundamental Considerations for Battery-Powered, Wireless IoT Sensor Product."
3. A. Vena, E. Perret, B. Sorli, and S. Tedjini, "Toward Reliable Readers for Chipless RFID Systems," 2014 XXXIth URSI General Assembly and Symposium (URSIGASS), August 2014, doi:10.1109/URSIGASS.2014.6929209.
4. A. Vena, E. Perret, and S. Tedjini, "Design of Compact and Auto-Compensated Single-Layer Chipless RFID Tag," *IEEE Transactions on Microwave Theory and Techniques*, **60**, 9, July 2012, pp. 2913-2924, doi:10.1109/TMTT.2012.2203927.
5. D. Kuester and Z. Popovic, "How Good Is Your Tag?: RFID Backscatter Metrics and Measurements," *IEEE Microwave Magazine*, **14**, 5, July 2013, pp. 47-55, 10.1109/MMM.2013.2259394.
6. S. Tedjini, O. Boularess, T. Andriamiharivolamena, H. Rmili, and T. Aguil, "A Novel Design of Chipless RFID Tags Based on Alphabets," IEEE MTT-S International Microwave Symposium, June 2017, pp. 1561-1563, doi:10.1109/MWSYM.2017.8058929.
7. S. Genovesi, F. Costa, M. Borgese, A. F. Dicandia, G. Manara, S. Tedjini, and E. Perret, "Enhanced Chipless RFID Tags for Sensors Design," IEEE International Symposium on Antennas and Propagation (APURSI), June/July 2016, pp. 1275-1276, doi:10.1109/APS.2016.7696345.
8. S. Tedjini, N. Karmakar, E. Perret, A. Vena, R. Koswatta, and R. E-Azim, "Hold the Chips: Chipless Technology, An Alternative Technique for RFID," *IEEE Microwave Magazine*, **14**, 5, July 2013, pp. 56-65, doi:10.1109/MMM.2013.2259393.
9. A. Vena, E. Perret, and S. Tedjini, "RFID Chipless Tag Based on Multiple Phase Shifters," IEEE International Microwave Symposium Digest (MTT), June 2011, doi:10.1109/MWSYM.2011.5972712.



13th International Congress on Artificial Materials for Novel Wave Phenomena

Metamaterials 2019

Rome, Italy, 16 – 21 September 2019

The *Thirteenth International Congress on Artificial Materials for Novel Wave Phenomena – Metamaterials 2019*, will comprise a **4-day Conference (16–19 September)**, and a **2-day Doctoral School (20–21 September)**. Organized by the *METAMORPHOSE VI AISBL* (www.metamorphose-vi.org), this Congress follows the success of *Metamaterials 2007-2018* and continues the traditions of the highly successful series of *International Conferences on Complex Media and Metamaterials (Bianisotropics)* and *Rome International Workshops on Metamaterials and Special Materials for Electromagnetic Applications and Telecommunications*. The Congress will provide a unique topical forum to share the latest results of the metamaterials research in Europe and worldwide. It will bring together the engineering, physics, applied mathematics and material science communities working on artificial materials and their applications in electromagnetism/optics, acoustics/mechanics, transport, and multi-physics.

Paper Submission

Papers should be 2-3 pages long and contain an abstract, a brief conclusion, and a main body where technical content and novelty of the work are clearly presented.

Papers should be submitted as camera-ready PDF files to the website:

<http://congress2019.metamorphose-vi.org>

Authors are requested to use the template provided on the Congress website when preparing their submission. Authors of accepted and presented papers will be given the option of publishing their work in IEEE Xplore subject to the manuscript compliance with the format and copyright requirements.

Committees

General Chair

Alessio Monti, Italy

Technical Program Committee Chair

Martin Wegener, Germany

Local Organizing Committee

Mirko Barbuto

Filiberto Bilotti

Angelica Viola Marini

Davide Ramaccia

Alessandro Toscano

Stefano Vellucci

Contact

contact@metamorphose-vi.org

Submission deadline

10 March 2019

Topics

We interpret metamaterials as rationally designed composites, the effective properties of which go beyond their bulk ingredients, qualitatively and/or quantitatively. **We accept papers in any combination out of the following 8 categories:**

Category 1 - Area

- Electromagnetic from DC to optical and beyond (including, e.g., metallic, dielectric, magnetic, and superconducting ingredients)
- Acoustic and mechanical (including, e.g., seismic)
- Transport (including, e.g., nanoelectronics, and thermal transport)
- Multi-physics

Category 2 - Geometry

- 1D, 2D, and 3D metamaterials and metasurfaces
- (1+1)D, (2+1)D, and (3+1)D space-time metamaterials and metasurfaces
- Individual meta-atoms
- Meta-systems (including, e.g., gradient metamaterials, metamaterials in architectures designed by coordinate transformations, as well as far-field and near-field imaging systems)

Category 3 - Arrangement

- Periodic
- Non-periodic

Category 4 - Frequency

- Static
- Dynamic (including wave propagation)

Category 5 - Type

- Passive
- Active

Category 6 - Status

- Fixed properties
- Tunable properties (including, e.g., modulators, switchable properties, software-defined, and adaptive properties)

Category 7 - Physical basis

- Classical (linear and nonlinear, including, e.g., multistable and programmable)
- Quantum

Category 8 - Technology Readiness Level

- Effective-medium theories and homogenization (including, e.g., high-frequency and high-contrast homogenization and spatial dispersion modelling)
- Design (including, e.g., analytical approaches, topology optimization, numerical methods, machine and deep learning, bio-inspiration)
- Fabrication and characterization (including, e.g., new manufacturing approaches, 3D additive manufacturing, parameter retrieval, reliability testing, and fatigue testing)
- Applications and commercialization (including, e.g., antennas, sensing, spectral and spatial filtering, civil engineering, marine engineering, biology, and earthquake protection)

In addition, we accept papers on composites, plasmonics, photonic crystals, phononic crystals, and invisibility cloaking if related to the scope of the congress in some way.

Et Cetera



Tayfun Akgül

Istanbul Technical University
Dept. of Electronics and Communications Engineering
Telecommunications Division
80626 Maslak Istanbul, Turkey
Tel: +90 212 285 3605; Fax: +90 212 285 3565
E-mail: tayfunakgul@itu.edu.tr



No,
I can't take
a selfie now.



t...



George Trichopoulos

Electrical, Computer & Energy Engineering ISTB4
555D

Arizona State University

781 E Terrace Road, Tempe, AZ, 85287 USA

Tel: +1 614 364 2090

E-mail: gtrichop@asu.edu

Four Pillars of Radio Astronomy: Mills, Christiansen, Wild, Bracewell by R. H. Frater, W. M. Goss, and H. W. Wendt, Springer, Astronomers' Universe Series, 2018, ISBN 978-3-319-65598-7; € 32.00.

After the initial detection of radio radiation from the center of our Galaxy (Milky Way) by K. G. Jansky in 1932, and the pioneering observations by G. Reber in the early 1940s, radio astronomy grew into an active field of research after the second World War. The development of radar offered the physicists and engineers suitable equipment for use in the observation of radio radiation from the sky. This was undertaken with great emphasis, notably in England and Australia and also in the USA. Based on van de Hulst's prediction of the spectral line of neutral atomic hydrogen at 21 cm wavelength, detection of this line became the goal of activity in The Netherlands.

Radio astronomy is only about 75 years old. While the pioneers of the first generation have all gone, a good number of their pupils and successors are still around, many at retirement age with ample time to reminisce about the development of their science. As a result, there is a growing library of books and essays covering the history of radio astronomy. Biographies of astronomers are regularly appearing, often written by their students and collaborators. The close personal contact between author and subject often gives these biographies a special cachet that makes for pleasant reading. The book under review falls in this category.

In Australia, a large group of radar experts inhabited the Radiophysics Laboratory (RPL) of the Commonwealth Scientific and Industrial Research Organisation (CSIRO). After the war, CSIRO returned to peacetime research. From this emerged a radio astronomy research group under the direction of E. G. "Taffy" Bowen, Chief of Radiophysics, and the scientific leadership of Joseph "Joe" Pawsey, which was the largest radio-astronomy laboratory in the world. Bowen and Pawsey fostered independence of the individual

researcher within an atmosphere of collegial collaboration. This was highly successful in a new area of science, where astronomy, physics, and diverse engineering solutions could be combined and developed. The book under review, *Four Pillars of Radio Astronomy*, tells the story of four men, Bernie Mills, Chris Christiansen, Paul Wild, and Ron Bracewell, who rose from the group to eminent positions in radio astronomy in Australia and beyond.

The book is part of the "Astronomers' Universe" series from Springer that aims to be attractive to non-expert astronomers and advanced "amateur astronomers." Indeed, *Four Pillars* does not contain mathematics. Instead, it is richly illustrated with photos and diagrams, all from the period covered by the narrative, roughly up to the mid-seventies. After an introductory chapter, the authors present an outline of radio astronomy and short descriptions of the pioneering work by Jansky and Reber. The activities of the Radiophysics Laboratory during the war are mentioned. The two key personalities, Bowen and Pawsey, who would establish and lead the radio astronomy group, are introduced. They were the founders and architects of the Australian radio-astronomy edifice upon which the protagonists of this book could erect their "pillars." At the end of this chapter, there is a very short mention of John Bolton, who in the reviewer's opinion was as much a pillar of Australian radio astronomy as the subjects of this book. Perhaps this omission is due more to the recent publication of a biography of Bolton by Peter Robertson than the authors' evaluation of Bolton's career.

The following four chapters are devoted to each of the four pillars. Summaries of early childhood and schooldays are followed by descriptions of university study. In the atmosphere of radiophysics, each could and did execute his research program and the development of instrumentation. It is repeatedly stressed that this happened in a highly collegial and communicative way. This close relationship within one institute came to an end in 1960, when CSIRO determined that it could not sufficiently support all groups for each to

remain competitive. Fortunately, the University of Sydney had the foresight of enabling two groups to move into well-supported professorial positions. Mills joined the Physics Department, and Christiansen went to the Department of Electrical Engineering. Paul Wild remained at CSIRO, while Bracewell had already left in 1955 for a professorship at Stanford University, in the USA.

Bernie Mills concentrated on surveying the sky in search of radio sources, with the aim of identifying those with optical objects. To reliably determine the celestial position of radio sources, Mills sought a way to create a narrow “pencil beam” without having to build a two-dimensional fully covered reflector. He found the solution in combining the signals from two perpendicular linear antennas respectively in the EW and NS directions. This design has become known as a “Mills Cross,” providing an angular resolution proportional to the length of the arms of the cross.

With the first version of his cross, Mills performed a survey of the southern sky at 85 MHz, and produced a catalog of more than 2200 sources. After his move to the Physics Department of the university, Mills was able to build a cross with one-mile arms, operating at 408 MHz, located near Canberra along the Molonglo river: the Molonglo Cross. The instrument has been upgraded twice, and is still in full operation.

Chris Christiansen was the leader of one of the solar-research groups. His aim was to obtain high-resolution radio pictures of the sun with 3 arcminutes resolution. To this end, two “grating arrays” were deployed, one in the NS direction, the other EW, each with 32 dishes. The sun was tracked during four hours per day, and the signals of the two arrays were cross-correlated and Fourier transformed by hand. This required weeks of tedious calculations to deliver a radio picture of the sun. This was the first application of “Earth-rotation synthesis,” which has been used by most later interferometric-array telescopes. A similar cross, called Chris Cross, was later built to map radio sources at 21 cm wavelength.

After “Doc” Ewen detected the spectral line of neutral hydrogen at 21 cm at Harvard University in April 1951, he sought confirmation of his discovery from the Dutch, who were close to completing their own experiment, and from the Australians. Chris and Jim Hindman jumped at the occasion, and constructed a makeshift receiver with which they confirmed the detection about three months later. In the description of this event, the authors ignored the contribution of the Dutch, who confirmed Ewen’s detection within six weeks, along with a first astronomical deduction concerning the rotation of the Galaxy. Actually, a very close collaboration between the Dutch and Australian groups followed (with Frank Kerr spending time in Holland), resulting, within a few years, in a map of the neutral hydrogen distribution in the Galaxy.

Chris frequently visited foreign institutes for longer periods and was also active in international organizations, particularly URSI, of which he was President from 1978-1981. These aspects are well covered, and present a lively description of Chris’ character and personality.

Paul Wild is a native Englishman of the Four Pillars. He spent time in Australia during his war duty. In 1947, he returned to Australia and joined the radio-astronomy group of Pawsey.

He worked on solar spectrographs and became “a solar man,” as he named himself. His theoretical knowledge and insight enabled him to provide physical interpretations for the different phenomena the sun produced in the radio regime. In 1959, he proposed the construction of a large radioheliograph that would produce a picture of the sun with an angular resolution of one arcminute and a time resolution of a few seconds. This instrument was built near Narrabri, and consisted of 96 dishes of 13.7 m diameter placed on a circle with 3 km diameter. From 1967 onwards, it produced daily observations of the sun of unsurpassed angular resolution on a time scale of seconds. It revolutionized the study of the radio sun. In 1971, Paul was promoted to Chief of Radiophysics of CSIRO. Next to radio astronomy, the division developed an aircraft landing system, *Interscan*, which was adopted internationally. In 1978, Paul Wild became chairman of a complete restructuring of CSIRO. It resulted in the construction of the Australian Compact Array (ACA) at the site of the decommissioned solar array. It was renamed the Paul Wild Observatory.

Ron Bracewell joined the RPL at CSIRO in 1943 as assistant to Joe Pawsey. In 1946, he went to Cambridge to study ionospheric physics under Ratcliffe. Upon obtaining his PhD in 1949, he returned to CSIRO and turned his attention to radio astronomy. He did not develop or build his “own” telescope, but involved himself in the scientific operation of the arrays run by Christiansen and Mills. In the early fifties, with some colleagues he wrote a number of seminal papers on the mathematics and practicalities of converting the observed data into “pictures” of the astronomical objects. Central in this work was the application of the Fourier transform. His 1965 book *The Fourier Transform* became an overnight classic. Pawsey involved him in the writing of the first textbook on radio astronomy (1955), in which his talent for clear exposition was obvious. He contributed a chapter of almost 100 pages, “Radio Astronomy Techniques,” to volume 54 of the *Handbuch der Physik* in 1962. He gave me a signed reprint of this booklet just as I was learning radio astronomy at NRAO: a precious gift.

Ron left Australia already in 1955 for Stanford in the USA, where he established a Radio Astronomy Institute with a solar spectroheliograph that produced daily pictures of the sun at 9 cm wavelength. In the late sixties, he built a five-element non-redundant synthesis array of 18-m

antennas, designed in-house, operating at 3 cm wavelength. He remained at Stanford for the rest of his life.

In Chapter 7, the authors summarize the influence of the Four Pillars beyond radio astronomy. They emphasize the collaborative and collegial way of the Pillars in the interaction among themselves and in the international arena, where they were active and mobile. Their work led to several industrial and commercial ventures, with the development of the Wi-Fi standard as the most visible. The Conclusion presents a condensed exposé of the style and influence of the four gentlemen. Several appendices complete the book, among them a short description of “what is a radio telescope” and a timeline of events covered in the book.

In summary, the book tells a highly readable story of four scientists/engineers who contributed to the development and high international standing of radio

astronomy in Australia. The narrative combines the character and achievements of the main protagonists within the organizational environment in which they worked. The book is abundantly filled with original photos and illustrations. I can recommend it to all radio astronomers that are old enough to have personally known the Four Pillars. It will be a good read to anyone with an interest in the development of science in post-war Australia, where wartime radar research was replaced by peacetime development of the new science of radio astronomy.

Jacob W. M. Baars
Max-Planck-Institut für Radioastronomie
Bonn, Germany
E-mail: jacobbaars@arcor.de

Correction

In [1], a term was omitted from Equation (6). The correct version of the equation is as follows:

$$\begin{aligned} \frac{dM}{dz} &= \frac{dp}{dz} \left(\frac{1.336 \times 10^7 w}{\theta^2 p^{0.572}} + \frac{399.54}{\theta p^{0.286}} \right) \\ &+ \frac{dw}{dz} \left(\frac{3.106 \times 10^7 P^{0.428}}{\theta^2} \right) \\ &- \frac{d\theta}{dz} \left(\frac{6.212 \times 10^7 w p^{0.428}}{\theta^3} + \frac{559.6 p^{0.714}}{\theta^2} \right) \\ &+ 0.157 \text{ m}^{-1}. \end{aligned} \quad (6)$$

The *Radio Science Bulletin* regrets the omission.

Reference

1. R. E. Marshall, V. R. Wiss, K. L. Horgan, W. D. Thornton, and J. K. Stapleton, “Flux-Conservation Technique for Blending Refractivity Profiles in the Marine Atmospheric Boundary Layer,” *Radio Science Bulletin*, No. 363, December 2017, pp. 39-51.



Randy L. Haupt
Colorado School of Mines
Brown Building 249
1510 Illinois Street, Golden,
CO 80401 USA
Tel: +1 (303) 273 3721
E-mail: rhaupt@mines.edu



Amy J. Shockley
E-mail: aj4317@gmail.com

The Owl: Follow Through Is Critical

Randy L. Haupt and Amy J. Shockley

One day while I was working at home, I noticed movement outside the window next to my desk. When I looked up, I saw a Great Horned Owl sitting on my porch. Wow! This bird was magnificent. Its huge eyes stared back at me. I took a picture through the window, and then decided to get a little closer to get an even better picture. I opened the door and looked around the corner. Of course, the owl saw me and carefully watched as I took its picture before retreating back inside. It sat there for a long time. I had trouble concentrating, and instead found myself watching the owl as it remarkably stared back at me.

I sent the picture to my wife, and she forwarded it to some friends at Penn State who are avid birders. They replied that the owl was very young, most likely only a month or so old. We enjoyed watching the owl for several days as it perched on various objects around our house. One night, I heard the owl screeching and some coyotes howling and making noise. The first thing that occurred to me was that the coyotes had gotten our owl! I almost ran outside to rescue the owl, but thought better of getting in the middle of wild animals fighting. The next morning, my wife and I saw the owl, and its wing was wounded. I stepped onto the porch to try to scare it into flying, but it just hopped around, clearly injured.

My wife called an organization called Birds of Prey, and left them my cell-phone number. About an hour later, they called me and asked me to send them a picture of the

owl. They explained that capturing a bird is very stressful, and is a last resort. I e-mailed them a picture, and they immediately called me back. They confirmed that the owl was very young. They also said that it needed immediate attention, so I was to capture the owl and bring it to their facility. I said, "You want me to do what?" The lady casually replied that I was to capture it in a box and bring it to them. I exclaimed, "I'm not capturing a wild animal that could eat me!" She calmed me down and said that it was my duty. She instructed me to get a cardboard box and place it over the bird before slipping a flat piece of cardboard underneath. She said that this would appropriately enclose the bird and allow me to transport it to their facility, where they could help it. I told her that the owl was not going to let me do that. She responded that the owl was young and injured, so it would be an easy task. I was not convinced. My wife told me to wait until she came home, and she would help me. I wondered if my insurance would cover injury or death by an owl.

I went outside and could not find the bird. Great! The owl must be OK, because it flew away. I don't have to risk my life catching it.

A few hours later, I rode my bike out to lunch to meet a colleague. When I returned, my neighbor and his son were in my yard. He announced, "You know that you have an injured owl in your yard. My son and I brought a cooler to catch him then take him to the Birds of Prey." Being an



Figure 1. The owl.

expert in owl-catching (at least in theory), I explained the proper way to catch an owl. In my expert opinion, putting it in a large plastic cooler with no ventilation was not a good idea.

After briefing my neighbors, we set out to capture the owl. The three of us ended up chasing the owl around my yard, trying to corral it into a cardboard box. The owl couldn't fly, but it did run pretty fast. Finally, I chased the owl towards my neighbor and he captured it with his box. This owl was not as cooperative as I was led to believe. We slid the cardboard underneath, made sure there was breathing holes, and duct-taped the box. A piece of cake when you are an expert. He and his son raced off to take the owl to the Birds of Prey facility.

Recognizing and communicating a problem feels heroic (calling Birds of Prey); however, many problems that we face require additional action and follow-through (catching the owl and bringing it to the Birds of Prey). I thought that reporting the problem to Birds of Prey would be the extent of my involvement in this rescue mission. After all, the phone call was a crucial cog in connecting the injured owl with the expert help it needed. I could have justified this simple action as serving my ethical obligation to help the owl, and blamed its looming fate on the inaction of the professionals I had notified. However, while that may have allowed me to sleep at night, it would not have helped the owl. It was clear that the only way to rescue the owl was for me to take on the responsibility of getting it to the Birds of Prey facility.

Seeing a task through to a final resolution can feel daunting, especially if you are ill-equipped or inexperienced. Creative problem solving and leveraging resources is key to approaching difficult situations (in this case, the potential life or death for the owl). I leveraged the expertise of the Birds of Prey to learn the proper technique to ensnare an owl, and received help from my neighbors for the execution. When our initial efforts were futile, not anticipating the ground speed of the owl, we regrouped and came up with a strategy that utilized our numbers to our advantage, allowing us to successfully capture the owl.

There are numerous examples of scenarios where people felt that they had fulfilled their obligation by simply bringing a problem to light. It is important to remember to empathize with those impacted by the situation, and take ownership in resolving the problem. Follow-through is important! Taking ownership does not mean that you need to be the sole contributor to the resolution, as there are knowledge and capacity restrictions in being able to do so. It instead requires tenacity, resourcefulness, and creativity. I did follow up on the fate of the owl, and if you are curious to know the outcome, bring it up the next time you see me. If you have owl problems, call an expert – not me.



Özgür Ergül

Department of Electrical and Electronics Engineering
Middle East Technical University
TR-06800, Ankara, Turkey
E-mail: ozergul@metu.edu.tr

SOLBOX-12

Hande İbili, Barışcan Karaoşmanođlu, and Özgür Ergül

Department of Electrical and Electronics Engineering
Middle East Technical University
TR-06800, Ankara, Turkey
E-mail: ozergul@metu.edu.tr

1. Introduction

In three-dimensional electromagnetic solvers, extreme values for electrical parameters typically lead to instability, inaccuracy, and/or inefficiency issues. Despite using the term “extreme,” such relatively large or small values of conductivity, permittivity, permeability, wavenumber, intrinsic impedance, and other electrical parameters are commonly observed in natural cases. Computational electromagnetic solvers adapt themselves to handle challenging cases by replacing exact models with approximate models, while minimizing the modeling error due to these transformations. For example, most metals with high conductivity values are assumed to be perfectly conducting, especially if the considered structure is comparable to the wavelength. This is very common for practical devices, such as antennas, metamaterials, filters, etc., at radio and microwave frequencies. In some cases – e.g., when the overall structure is small in terms of a wavelength – even a full-wave solver may not be required to analyze the underlying phenomena. Examples are circuit theory based on lumped elements and transmission-line modeling. On the other side, penetrable models are commonly used to represent dielectric and magnetic materials, when their electrical parameters (specifically, permittivity and permeability) have numerically “reasonable” values that facilitate their full-wave solutions without a fundamental

issue. As the electrical parameters become extreme and other conditions (sizes, excitations, geometric properties) are satisfied, numerical approximations may again become useful, leading to the well-known implementations such as those based on impedance boundary conditions and physical optics.

New structures and devices in the state-of-the-art technology often require very accurate simulations with extreme values for electromagnetic parameters. One well-known regime involves the plasmonic behaviors of some metals at optical frequencies [1]. In the frequency domain, traditional solvers can be extended to accurately handle such exotic cases by employing complex permittivity values with negative real parts [2-13]. As the frequency drops, the real part of the permittivity is increasingly negative (becoming extreme), while it becomes unnecessary to enforce the plasmonic modeling (and hence to use extreme permittivity values) due to quickly decaying waves inside objects. Nevertheless, there is no obvious boundary between plasmonic modeling and perfectly conducting (limit) modeling and, more importantly, a suitable model at a given frequency may actually depend on the structure and the considered application [14]. Similar issues occur when dealing with detailed metallic structures, such as circuits when the skin effect cannot be ignored and metallic losses must be included (even if they are large) in

their electromagnetic analysis [15]. In all these cases, we obviously need very reliable numerical solvers based on generalized formulations and algorithms that automatically converge into suitable forms for given conditions without externally enforcing risky approximations described above.

However, what happens when extreme electrical parameters must be fully included in an electromagnetic analysis? In the context of the surface integral equations in the frequency domain, the wavenumber that contains medium parameters is used in the Green's function, i.e., the kernel of the equations. The value of the wavenumber hence determines how fast the Green's function decays and how much it is oscillatory. These properties should be considered together with the interaction distances that depend on the metric size of the structure under investigation. However, even when the wavenumber is well balanced with metric distances such that numerical issues do not arise from the Green's function itself, absolute values of permittivity, permeability, and/or their ratio as the intrinsic impedance, may strongly affect the stability of solutions. This is because integral-equation (and similar) formulations are mostly designed (for example, numerically balanced) for reasonable values of these quantities [16].

In this issue of Solution Box, a set of frequency-domain scattering problems involving spherical particles is presented. Neither the geometry nor the size in terms of wavelength is the challenge in these problems. Instead, some hypothetically extreme values for the permittivity are considered, such that numerical issues may arise in the conventional solvers. Sample solutions using a specialized integral-equation formulation are also presented as references for candidate solutions by using other implementations developed by the readers. As usual, we are looking for alternative solutions, which are probably more accurate, stable, and/or efficient than presented here. Please also consider sending your solutions for the earlier problems (SOLBOX-01 to SOLBOX-11) to present your work in this column.

2. Problems

2.1 Problem SOLBOX-12 (by Hande İbili, Barışcan Karaosmanoğlu, and Özgür Ergül)

The SOLBOX-12 problem includes scattering problems involving spherical particles of diameter $1.0 \mu\text{m}$ at 10 THz and 1 THz, i.e., when the diameter was $\lambda/30$ and $\lambda/300$ where λ was the wavelength in vacuum. Each sphere was located at the origin (in vacuum) and illuminated by a plane wave (1 V/m) propagating in the z direction. For numerical solutions with surface integral equations, discretization was applied by using 50 nm triangles for 10 THz and 30 nm triangles for 1 THz, leading to totals of 2720 and 7722 triangles, respectively. For the relative

complex permittivity of the sphere in the frequency domain, the following hypothetical values were considered:

Positive real part: $(20000+2i)$, $(20000+200i)$, $(20000+20000i)$, $(2+20000i)$, $(200+20000i)$

Negative real part: $(-20000+2i)$, $(-20000+200i)$, $(-20000+20000i)$, $(-2+20000i)$, $(-200+20000i)$

As a remarkable example, the relative complex permittivity values for pure silver at 10 THz and 1 THz are approximately $(-17000+20000i)$ and $(-30000+340000i)$, respectively, so that the values above were not simply academic trials. As the results of simulations, scattering characteristics (e.g., equivalent currents, near-zone fields, and/or far-zone fields) were required to be found.

3. Solution to Problem SOLBOX-12

3.1 Solution Summary

Solver type (e.g., noncommercial, commercial): Noncommercial research-based code developed at CEMMETU, Ankara, Turkey

Solution core algorithm or method: Frequency-domain Method of Moments

Programming language or environment (if applicable): *MATLAB + MEX*

Computer properties and used resources: 2.5 GHz Intel Xeon E5-2680v3 processors (using single core)

Total time required to produce the results shown Total time required to produce the results shown (categories: < 1 sec, < 10 sec, < 1 min, < 10 min, < 1 hour, < 10 hours, < 1 day, < 10 days, > 10 days): < 1 hour for each problem

3.2 Short Description of the Numerical Solutions

The scattering problems listed under SOLBOX-12 were solved by using an iterative Method of Moments. The problems were formulated with a modified combined tangential formulation (MCTF) [17] that was known to be stable for large (and particularly negative) permittivity values. The MCTF was discretized by using the Rao-Wilton-Glisson (RWG) functions. Electromagnetic interactions (matrix elements) were computed via Gaussian quadrature formulas combined with standard singularity-extraction methods. All solutions were performed by using the Generalized Minimal Residual (GMRES) method, while the target residual error was selected as 0.0001.

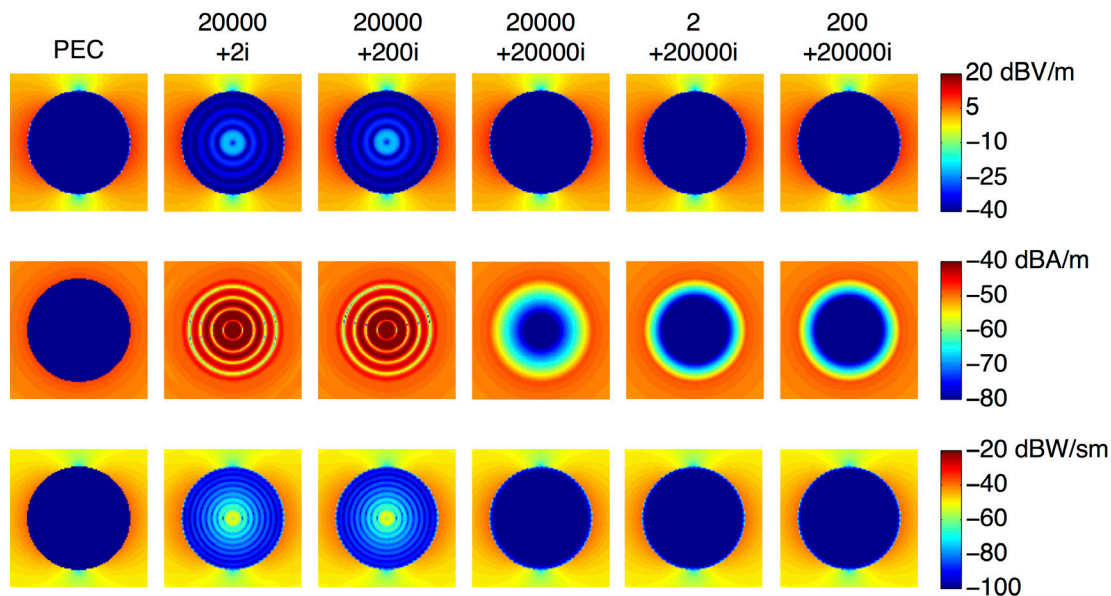


Figure 1. The solutions of the scattering problems (SOLBOX-12) involving spheres with positive values for the real part of the relative permittivity (values are shown on the top) at 10 THz. The electric-field intensity (first row), the magnetic-field intensity (second row), and the power density (third row) were plotted in the vicinity of the spheres.

3.3 Results

Figure 1 presents the results for the scattering problems involving the spheres with positive real permittivity values. As an additional solution, we also considered the case of a perfectly electrically conducting (PEC) sphere. The electric field intensity (first row), the magnetic field intensity (second row), and the power density (third row)

were plotted in the vicinities of the spheres on the cross-sectional (x - y) plane. The dynamic ranges were $[-40, 20]$ dBV/m, $[-80, 40]$ dBA/m, and $[-100, -20]$ dBW/sm, respectively (also for the other results). Despite that the outer intensity and density values were similar to each other for different cases (permittivity values), the internal quantities were quite different from each other. We also had the following observations:

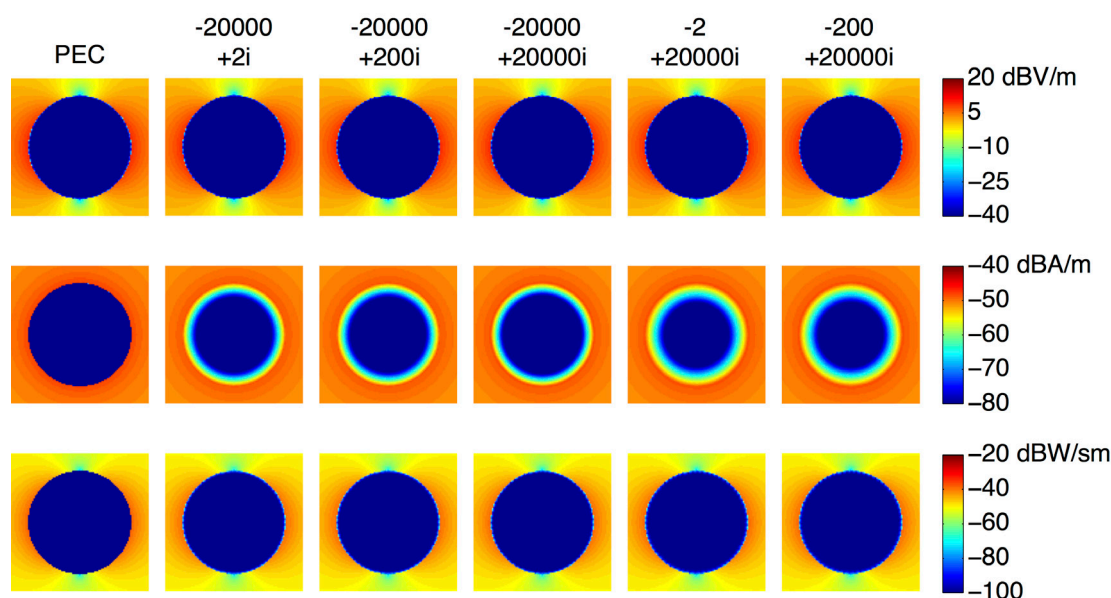


Figure 2. The solutions of the scattering problems (SOLBOX-12) involving spheres with negative values for the real part of the relative permittivity (values shown on the top) at 10 THz. The electric-field intensity (first row), the magnetic-field intensity (second row), and the power density (third row) were plotted in the vicinity of the spheres.

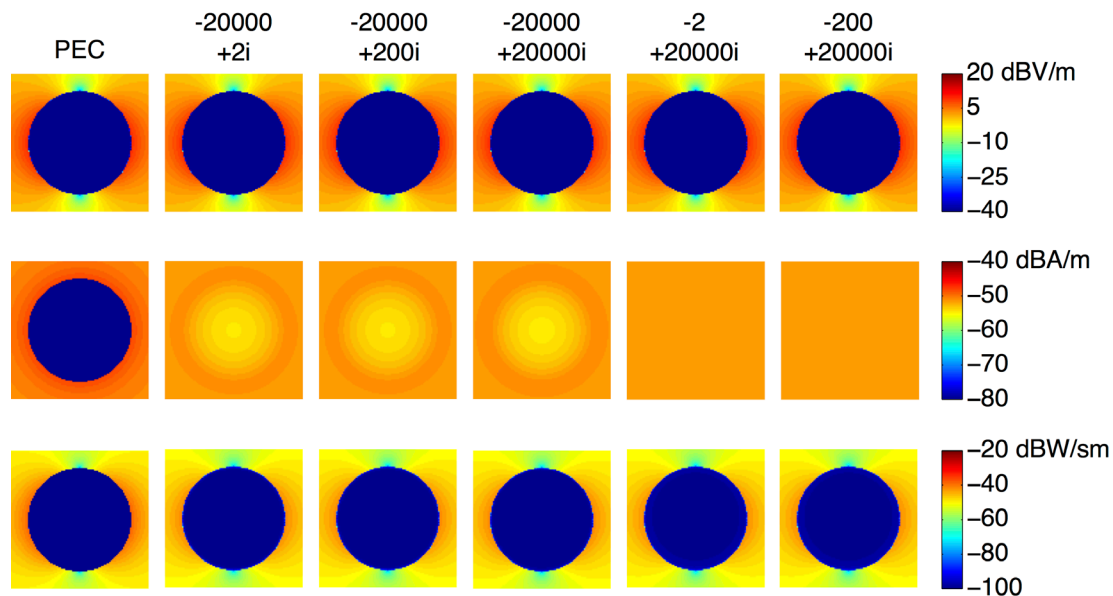


Figure 3. The solutions of the scattering problems (SOLBOX-12) involving spheres with negative values for the real part of the relative permittivity (shown on the top) at 1 THz. The electric-field intensity (first row), the magnetic-field intensity (second row), and the power density (third row) were plotted in the vicinity of the spheres.

For all cases, the electric-field intensity was relatively small inside the spheres. This was as opposed to the behaviors of the magnetic-field intensity and the power density, which were particularly large in the first two cases (20000+2i and 20000+200i). Here, “large” and “small” are defined by considering outer fields.

In the first two cases, oscillatory behaviors were also observed in the intensity and density distributions, which seemed to be related to the relatively large values for the real part of the wavenumber. On the other side, for the last three cases, decaying characteristics were mainly observed due to the large values for the imaginary part of the wavenumber. Nevertheless, even for the relative permittivity of (200+20000i), a remarkable level of magnetic-field intensity was observed inside the sphere, showing that the PEC model was actually inaccurate, at least considering the near-zone characteristics.

Figure 2 next presents the results when the real part of the permittivity was negative at 10 THz. We noted that negative real permittivity led to an increased imaginary part of the wavenumber, leading to a fast decay of fields, even more than did metallic losses. The magnetic-field intensity was more confined in the vicinity of the surfaces in first three cases, i.e., when the real part was -20000. Interestingly, despite the magnetic-field intensity significantly depending on the permittivity, the electric-field intensity was almost the same (and very small) for all cases, including the PEC case. In fact, the decay rate was the same for the electric-field intensity and the magnetic-field intensity. However, very small intrinsic impedance values further suppressed the electric-field intensity, making it vanishingly zero in

all cases. This also led to vanishingly small power-density values, making the penetrable particles behave like PEC.

Figure 3 depicts the cases when the real permittivity took negative values while the frequency was 1 THz. Decreasing the frequency, the spheres became electrically smaller. Consequently, in the last two cases, there was not any visible decay in the magnetic-field intensity due to the very small electrical size of the spheres in comparison to the skin depth. Specifically, the particles became magnetically invisible. Some variation was still seen in the first three cases, since the magnetic-field intensity decayed very quickly with the distance for the given permittivity values in these cases. In all results, the electric-field intensity (and hence the power density) was again vanishingly zero inside the spheres due to the very small intrinsic impedance values.

4. References

1. P. B. Johnson and R.-W. Christy, “Optical Constants of the Noble Metals,” *Phys. Rev. B*, **6**, 12, December 1972, pp. 4370-4379.
2. U. Hohenester and J. Krenn, “Surface Plasmon Resonances of Single and Coupled Metallic Nanoparticles: A Boundary Integral Method Approach,” *Phys. Rev. B.*, **72**, 195429, November 2005.
3. T. Sondergaard, “Modeling of Plasmonic Nanostructures: Green’s Function Integral Equation Methods,” *Phys. Status Solidi B.*, **244**, 10, October 2007, pp. 3448-3462.

4. A. M. Kern and O. F. J. Martin, "Surface Integral Formulation for 3D Simulations of Plasmonic and High Permittivity Nanostructures," *J. Opt. Soc. Am. A.*, **26**, 4, April 2009, pp. 732-740.
5. B. Gallinet and O. F. J. Martin, "Scattering on Plasmonic Nanostructures Arrays Modeled with a Surface Integral Formulation," *Photonics and Nanostructures – Fundamentals and Applications*, **8**, 4, September 2010, pp. 278-284.
6. R. Rodriguez-Oliveros and J.A. Sanchez-Gil, "Localized Surface-Plasmon Resonances on Single and Coupled Nanoparticles Through Surface Integral Equations for Flexible Surfaces," *Opt. Exp.*, **16**, 13, June 2011, pp. 12208-12219.
7. Ö. Ergül, "Parallel Implementation of MLFMA for Homogeneous Objects with Various Material Properties," *Prog. Electromagn. Res.*, **121**, November 2011, pp. 505-520.
8. Ö. Ergül, "Fast and Accurate Analysis of Homogenized Metamaterials with the Surface Integral Equations and the Multilevel Fast Multipole Algorithm," *IEEE Antennas Wireless Propag. Lett.*, **10**, November 2011, pp. 1286-1289.
9. M. G. Araujo, J. M. Taboada, D. M. Solis, J. Rivero, L. Landesa, and F. Obelleiro, "Comparison of Surface Integral Equation Formulations for Electromagnetic Analysis of Plasmonic Nanoscatterers," *Opt. Exp.*, **20**, 8, April 2012, pp. 9161-9171.
10. D. M. Solis, J. M. Taboada, and F. Obelleiro, "Surface Integral Equation Method of Moments with Multiregion Basis Functions Applied to Plasmonics," *IEEE Trans. Antennas Propag.*, **63**, 5, May 2015, pp. 2141-2152.
11. H. Gomez-Sousa, O. Rubinos-Lopez, and J.A. Martinez-Lorenzo, "Comparison of Iterative Solvers for Electromagnetic Analysis of Plasmonic Nanostructures Using Multiple Surface Integral Equation Formulations," *J. Electromagn. Waves Appl.*, **30**, 4, February 2016, pp. 456-472.
12. B. Karaosmanoğlu, A. Yılmaz, U. M. Gür, and Ö. Ergül, "Solutions of Plasmonic Structures Using the Multilevel Fast Multipole Algorithm," *Int. J. RF Microwave Comput.-Aided. Eng.*, **26**, 4, May 2016, pp. 335-341.
13. A. Çekinmez, B. Karaosmanoğlu, and Ö. Ergül, "Integral-equation Formulations of Plasmonic Problems in the Visible Spectrum and Beyond," in *Dynamical Systems – Analytical and Computational Techniques*, M. Reyhanoglu (ed.), London, InTech, 2017, pp. 191-214.
14. B. Karaosmanoglu and Ö. Ergül, "Accuracy of the Surface Integral-Equation Formulations for Large Negative Permittivity Values," *Proc. Progress in Electromagnetics Research Symp. (PIERS)*, 2017, pp. 926-933.
15. T. Xia, H. Gan, M. Wei, W. C. Chew, H. Braunsch, Z. Qian, K. Aygün, and A. Aydiner, "An Integral Equation Modeling of Lossy Conductors with the Enhanced Augmented Electric Field Integral Equation," *IEEE Trans. Antennas Propagat.*, **65**, 8, August 2017, pp. 4181-4190.
16. M. Taskinen and P. Ylä-Oijala, "Current and Charge Integral Equation Formulation," *IEEE Trans. Antennas Propagat.*, **54**, 1, January 2006, pp. 58-67.
17. B. Karaosmanoğlu, A. Yılmaz, and Ö. Ergül, "Accurate and Efficient Analysis of Plasmonic Structures Using Surface Integral Equations," *IEEE Trans. Antennas Propag.*, **65**, 6, June 2017, pp. 3049-3057.



European School of Antennas 2018



ANTENNAS FOR SPACE APPLICATIONS

ESTEC - Noordwijk, March 12-16
Coordinator: L. Salghetti

MICROWAVE IMAGING AND DIAGNOSTICS

UMED-UNITN, Madonna di Campiglio, March 19-23
Coordinators: A. Massa, T. Isernia

RADAR 2020

KIT - Karlsruhe, May 7-11
Coordinator: W. Wiesbeck

CHARACTERISTIC MODES: THEORY AND APPLICATIONS

UPV-Valencia May 14-18
Coordinators, M. Ferrando, P Hazdra,

ADVANCED MATHEMATICS FOR ANTENNA ANALYSIS

UNIZAG - Dubrovnik, May 21-25
Coordinators: Z. Sipus, S. Maci

TERAHERTZ TECHNOLOGY AND APPLICATIONS

UPC - Barcelona, May 28-June 1
Coordinators: L. Jofre, A. Raisanen, N. Lombar

COMPACT ANTENNAS FOR SENSOR SYSTEMS

UPC - Barcelona, June 4-8
Coordinators: L. Jofre, A. Skrivervik

ADVANCED MATERIALS FOR ANTENNAS

LBORO-NCSR Athens, June 18-22
Coor: Y. Vardaxoglou, A. Alexandridis

MILLIMETER WAVE ANTENNAS

UR1 - Rennes, July 2-6
Coordinators: A. Sharaiha, O. Lafond

ARRAYS AND REFLECTARRAYS

UCL - Louvain La Neuve, Sept. 3-7
Coordinator: C. Craeye

ADVANCED COMPUTATIONAL EM

POLITO, Torino, Sept. 10 - 14
Coordinators: F. Andriulli, G. Vecchi

ANTENNA SYSTEM INTEGRATION AND PACKAGING

KUL, Leuven- September 17-21
Coord. G. Vandebosch, U. Johansen, in cooperation with the MSCA H2020 Project SILIKA

SHORT RANGE RADIO PROPAGATION

UNIBO - Bologna, September 24-28
Coordinators: T. Kuerner, C. Oestges, F. Fuschini

ENERGY HARVESTING AND WIRELESS POWER TRANSFER FOR RFID AND WIRELESS SENSOR NETWORKS

HWU, Edinburgh- October 8-12
Coord. G. Goussetis, A. Georgiadis

Joined EuMA-ESOA Course

5G PHASED ARRAYS

TuDelft, NL, 25-29 June 2018
Coordinator: Alexander Yarovoy

ESoA Board



ESoA Coordinator Prof. Stefano Maci
Dept. of Information Engineering and Mathematics
University of Siena, 53100 - Siena (Italy)
E-mail: macis@ing.unisi.it

www.esoa-web.org



<http://www.facebook.com/europeanschoolofantennas>



James C. Lin
University of Illinois at Chicago
851 South Morgan Street, M/C 154
Chicago, IL 60607-7053 USA
E-mail: lin@uic.edu

DARPA's RadioBio and Recent US Bioelectromagnetic Research Programs

The U.S. Defense Advanced Research Projects Agency (DARPA) issued a request for proposals (RFP) in the spring of 2017 by announcing its new research initiative: Radiobio—What role does electromagnetic signaling have in biological systems? [1, 2] The stated goal of this project was to “determine if purposeful signaling via electromagnetic waves between biological systems exists, and, if it does, determine what information is being transferred.”

While it is not obvious how many proposals were received, indications are that by the end of 2017, several classified and unclassified projects were awarded DARPA grants under the RadioBio program. The RFP called for clearly identified, hypothesized communication channel(s) with specific predictions and experimental tests that would be undertaken to definitively prove each hypothesis.

The goal of Radiobio is at once innovative and intriguing, especially given DARPA's well-earned reputation of creating breakthrough technologies for national security and beyond. The well-known Internet project is an obvious case in point.

To ascertain, study, and comprehend the roles electromagnetic fields and waves possibly play in the intricate biology of living cellular organisms are of not only fundamental scientific importance, they also conjure up practical and technological values. The possibilities and potential applications in data transfer, information delivery, and communication for command and control are

enormous, once the bioelectromagnetic mechanisms for weak cell-to-cell signaling and communication in living organisms are harnessed.

The challenge of RadioBio is simple and complex at the same time.

It is simple, because living biological cells have long been documented to emit electromagnetic fields and waves. Their signals are detectable non-invasively, near the cell, or at a close distance via suitable sensors and instrumentation.

It is largely known that macroscopically, organized cells are capable of generating and emitting detectable electromagnetic signals in the noisy, cluttered environment of living bodies. Indeed, they have been routinely, non-invasively, and successfully applied to assist medical diagnoses and, for some, in therapeutic interventions. The abundant examples include electrocardiography (ECG) and magnetocardiography (MCG) from the heart, electroencephalography (EEG) and magnetoencephalography (MEG) from the brain, electromyography (EMG) from neuromuscular tissues, and electroretinography (ERG) from the eye, to name a few. These signals, relied upon in modern medical practices, are enabled by the electromagnetic fields and waves emitted by living cells, tissues, or organs. They are detectable from the surface of the human body using specific sensors and electronic instrumentation.

In cardiology, minimally invasive endocardioelectrophysiology of the myocardium is also often performed to help assess sources of cardiac arrhythmias inside the heart. Moreover, in many biomedical research laboratories, miniature penetrating and patch-clamp microelectrodes are regularly employed to record currents from the efflux and influx of biochemical ions, both intracellularly and extracellularly [3].

However, the spectra of the recordings mentioned above are typically low, well below 1 kHz: definitely not in the radio-frequency (RF) region above 3 kHz, the RF band commonly used for wireless communications. These types of low-frequency signals are capable of only supporting very limited information content for wireless-communication purposes.

This is not to imply that they are incapable of transmitting meaningful or purposeful messages using low-frequency signals that are well below the frequency bands commonly used for wireless communication. In fact, even a low-frequency signal with only one bit of information may convey a meaningful message in a purposefully designed wireless-communication system under specialized circumstances, for special purposes or operational requirements.

The complexity arises not merely from the fact that direct measurements of electromagnetic radiation of kHz to THz signals from a single cell or cluster of living cells close-in or far away have yet to be reported. There is a total lack of knowledge of any communication-relevant electromagnetic channel between biological cells or systems, or what biologically significant information may be transferred intracellularly or extracellularly.

Properties and behaviors of ion channels located at cell membranes are basic subjects presented in textbooks on physiology. They describe the critical roles ion channels play in regulating the life process of living biological cells, and by extension, in the functioning of higher organs and structures. Some explicit examples include the voltage-gated ion channels with their exquisite sensitivity to the transmembrane potential difference [4], and the mechanically gated ion channels with their unique sensitivity to mechanical deformations, stretches, and movements of the cells [5]. The phenomena of biochemical ionic exchanges through channels at cell membranes, ligands, or neurotransmitters through synaptic junctions in neural cells, in particular, are thus well established.

Exchange of biochemical ions via channels for cell membranes, ligands, or neurotransmitters at synaptic junctions represent movements of electronic charge-carrying ions (or charge flow). The flow of electrons forms what is referred to as electric currents. The flow of electrons (electric current) generates electromagnetic radiation by what is known as Ampere's law (a constitutive part of the classic Maxwell's theory of electromagnetism)

[6]. The emitted and received electromagnetic waves may embed or encode information or signaling for cell-to-cell communication. They may play a role in intracellular and/or extracellular communication under normal or physiologically stressed conditions. These electromagnetic fields and waves should be amenable to noninvasive detection. The detected electromagnetic fields and waves would thus be obviously purposeful, and they might also be playing some essential roles in signaling and communication alongside biochemical ions.

One project could be to design and execute controlled laboratory cell-biology experiments using isolated cells and cell clusters in culture: for example, isolated, identifiable, and viable snail esophageal neurons and neuron pairs. The snail neuronal cell preparation is selected for enhanced repeatability of results and its ability to maintain cell viability over an extended period of time at room temperature [7, 8]. These experiments could be followed up with other single cells and cell clusters in culture. The cells in culture potentially may transmit and receive signals via electromagnetic fields and waves.

Of course, it would be important to conduct computational bioelectromagnetic modeling to assess electronic signaling behaviors of as many intracellular and extracellular components as practical. The aim would be to specify unique features, signal levels, and bandwidths from ionic current flow and concomitant electromagnetic radiation. The aim would be to define electromagnetic effects that are purposeful, as opposed to just a side effect of ionic exchanges.

The working hypothesis could be characterization of a kHz to MHz communication channel derived from acquired data and precisely known facts, such as time constants from microelectrode-recorded electrophysiological signals and their fading behavior. Development of sensitivity-enhanced passive microsensors, nanoscale biosensors, graphene antennas, and instrumentation with proper bandwidth and sensitivity to noninvasively detect anticipated weak fields in extracellular space.

Actually, announcement of the RadioBio program is a big deal for the bioelectromagnetics discipline. Among other subjects in biology, engineering, and medicine, bioelectromagnetics research explores the effects of electric, magnetic, and electromagnetic fields and waves on living things. The discipline embraces a broad range of topics, the central theme of which falls within the interaction and application of electromagnetic fields and waves in biological systems including plants, seeds, mammalian cells, isolated tissues and organs in animals and humans, over a wide frequency range, which spans static fields to terahertz waves.

For the better part of a quarter century, the number of cellular devices and the variety of uses of wireless electromagnetic fields – including RF and microwaves for

security, well-being, medical, and real-world applications, literally, in every aspect of modern life –has grown exponentially. In contrast, funding for bioelectromagnetics research has steadily decreased to a trickle, whether by the government or the public sector. The wireless and cellular telecommunications industry has become complacent, and has had nearly free reign to develop and deploy cellular mobile phones and wireless RF devices and services as they see fit, with little regard for the biological effects and health implications of RF/microwave exposure and the considerable amount of unnecessary RF/microwave radiation to which people are being exposed all day long. The US government seems to have all but abandoned the Radiation Control for Health and Safety Act of 1968 and the preceding deliberations that led to the establishment of the Act [9].

However, there is an exception. The US Federal Food and Drug Administration (FDA) should be applauded for having initiated, and the National Institutes of Environmental Health Sciences (NIEHS) and the National Toxicology Program (NTP) praised, for having sponsored and conducted the recently completed US\$25M+ research on cell-phone RF radiation and cancer-causing studies in laboratory rodents [10-13].

Among the handful of bioelectromagnetics research projects, another visible and important role the US government has taken up in recent years is the Multidisciplinary University Research Initiative (MURI) grant program of the US Air Force Office of Scientific Research (AFOSR). This ongoing program supports fundamental, cutting-edge research that crosses traditional science and engineering boundaries. Its focus is on in-depth mechanistic research of the interaction of nanosecond pulsed electric fields (nsPEF) with living organisms, and the development of targeted stimulation procedures and processes [14].

The importance of the US government's role in sponsoring and conducting such research programs can not and should not be overlooked in this vital area of science, human health, and safety research investigations. The alternative may be to leave the matter entirely to the cell-phone industry (or perhaps, the military-industry complex) with free reign for RF biological effects research. That would be a scary scenario, since we are being continually exposed to more and more varieties of RF and microwave radiation 24 hours per day, seven days per week, and 52 weeks per year.

References

1. "Radiobio – What Role Does Electromagnetic Signaling Have in Biological Systems? Available at <https://www.darpa.mil/news-events/2017-02-07>.
2. DARPA DSO Opportunities Web site at <http://www.darpa.mil/work-with-us/opportunities?>.
3. T. G. Smith, H. Lecar, and S. J. Redman (eds.), *Voltage and Patch Clamping with Microelectrodes*, New York, Springer, 2013.
4. D. Purves, G. J. Augustine, D. Fitzpatrick, L. C. Katz, A. Samuel LaMantia, J. O. McNamara, and S. M. Williams (eds.), *Neuroscience, Second Edition*, Sunderland, MA, Sinauer Associates, 2001.
5. S. S. Ranade and R. Syeda, "Mechanically Activated Ion Channels," *Neuron*, **87**, 6, September 23, 2015, pp. 1162-119.
6. J. C. Lin, "Coupling of Electromagnetic Fields into Biological Systems," in J. C. Lin (ed.), *Electromagnetic Fields in Biological Systems*, Boca Raton, FL, CRC Taylor/Francis, 2011, pp. 1-57.
7. S. Arber and J. C. Lin, "Microwave-Induced Changes in Nerve Cells: Effects of Modulation and Temperature," *Bioelectromagnetics*, **6**, 1985, pp. 257-270.
8. S. Arber and J. C. Lin, "Extracellular Calcium and Microwave Enhancement of Conductance in Snail Neurons," *Radiation Environm. Biophysics*, **24**, 1985, pp. 149-156.
9. Radiation Control for Health and Safety Act of 1968, US Congress, Washington DC, 1968.
10. NTP Draft Reports, Public Comments, and Related Information: TR Peer Review Panel, <https://ntp.niehs.nih.gov/about/org/sep/trpanel/meetings/docs/2018/march/index.html>; last accessed April 26, 2018.
11. M. E. Wyde, T. L. Horn, M. H. Capstick, J. M. Ladbury, G. Koepke, P. F. Wilson, G. E. Kissling, M. D. Stout, N. Kuster, R. L. Melnick, J. Gauger, J. R. Bucher, and D. L. McCormick, "Effect of Cell Phone Radiofrequency Radiation on Body Temperature in Rodents: Pilot Studies of the National Toxicology Program's Reverberation Chamber Exposure System." *Bioelectromagnetics*, **39**, 2018, pp. 190-199.
12. J. C. Lin, "Clear Evidence of Cell Phone RF Radiation Cancer Risk," *IEEE Microwave Magazine*, **19**, 6, 2018, pp. 16-24.
13. J. C. Lin, "The NTP Cell Phone Radio Frequency Radiation Health Effects Project," *IEEE Microwave Magazine*, **18**, 1, 2017, pp. 15-17.
14. "Nanoelectropulse-Induced Electromechanical Signaling and Control of Biological Systems," <https://community.apan.org/wg/afosr/w/researchareas/22964/nanoelectropulse-induced-electromechanical-signaling-and-control-of-biological-systems/>; last accessed September 16, 2018.



Asta Pellinen-Wannberg
Umeå University, Department of Physics and
Swedish Institute of Space Physics
S-90187 Umeå, Sweden
Tel: +46 90 786 7492
E-mail: asta.pellinen-wannberg@umu.se

Introduction by the Associate Editor

This time, I present Dr. Ivana Kolmasova, who works at the Institute of Atmospheric Physics of the Czech Academy of Sciences as well as at the Charles University in Prague. I have met Ivana at several radio science meetings and been impressed by her technical approach to topics. After

reading her story, I understood where this deep knowledge was based. After an exam in electrical engineering, Ivana worked for years developing scientific instruments for various satellites. This must have taught her much about practical plasma physics, and given a very good background for finalizing a PhD in two and one-half years. She now participates in many exciting future solar-system missions. Here comes her story.

From Engineering to Physics

Ivana Kolmašová

Department of Space Physics
Institute of Atmospheric Physics
The Czech Academy of Sciences
Prague, Czechia
Faculty of Mathematics and Physics
Charles University
Prague, Czechia
E-mail: iko@ufa.cas.cz

I never dreamed about being a scientist. As a child, I watched my father, a nuclear physicist, immersed in scientific data analysis, calculating or plotting spectra. I rarely saw him read anything else than scientific papers or textbooks. All this seemed terribly boring to me. So, during my high-school studies, I eventually first wanted to become a fashion designer, then a librarian, then a doctor, and then a physical-education teacher. For various reasons, I left these teenage dreams piece-by-piece behind me. As I also liked mathematics and physics, I finally decided to study electrical engineering. After graduating from the university, my original plan was to work as an engineer in a hospital, taking care of medical instrumentation.

Suddenly, I then was offered a job in a team of engineers and technicians who were at that time assembling the second

Czechoslovak satellite Magion2. As a fresh electrical engineer, I participated in the finalization of the development of a scientific instrument dedicated for measurements of properties of ionospheric and magnetospheric plasmas. I was designing printed-circuit boards, I did a lot of hand soldering, and I spent hours and hours in testing the instrument's performance. Two years later, I breathlessly watched the launch of the Intercosmos24 satellite with the Czechoslovak sub-satellite Magion 2 attached, hesitating to see if the quality of my hand soldering was sufficient to survive the vibrations to which the electronics were exposed during the launch. A few weeks later, I was happy to learn that the instrumentation was nominally working.

As my life went on, I very much enjoyed time spent in maternity leave with my three children and, eventually,

time when I worked only part-time. I spent substantial parts of my days driving kids around (school, music lessons, swimming competitions, and all the other different places to which my kids needed to be driven). I nevertheless tried to stay in touch with my job, participating in various engineering tasks related to spacecraft instrumentation, and in the development and maintenance of instrumentation dedicated to ground-based ionospheric research.

After some time, the kids grew up and didn't need their devoted driver so often. A new impulse came to my professional career: we started to develop a receiver for the TARANIS mission (Tool for the Analysis of RADIations from lightNING and Sprites). This was a scientific micro-satellite of the French space agency, CNES. This receiver (IME-HF: "Instrument de Mesure du champElectrique Haute Fréquence") was dedicated to recording waveform measurements of fluctuating electric fields in the frequency range from a few kHz up to 37 MHz. The main scientific aims were to identify possible wave signatures associated with transient luminous phenomena occurring above thunderstorms, and to characterize lightning flashes from their high-frequency electromagnetic signatures. I became a member of the development team. As a technical manager of this receiver, I attended many meetings, I wrote tons of documents, and I spent many hours on testing the performance of the instrument in close contact with physicists from our group. During that time, we also had to face several serious problems, including the manufacturing failure in the flight-model printed-circuit board. We fortunately succeeded to remanufacture and test a new flight model in a very limited time. Nowadays, this receiver is finally being assembled and tested at the spacecraft level in order to be prepared for the 2019 launch.

The work on the development of the IME-HF receiver dedicated to lightning observations from space turned my attention to atmospheric electricity, and to the science of lightning and thunderstorms. When we tested the prototype of our TARANIS instrument using electromagnetic signals generated by natural lightning, we found that in spite of the fact that the nature of lightning has been known for more than 250 years, not everything was explained. Many questions, especially these that are related to lightning initiation, still remain unanswered. This was a moment when, pushed by curiosity and by my physicist colleagues, I started to think about shifting my focus from engineering to physics.

After twenty-five years of engineering work, I thus went back to school and started my PhD program in plasma physics. My adult children sometimes drove me to school, and all that time they were respectfully watching my efforts. Unlike me, they always believed that I would be able to complete my study. With the encouragement of my colleagues and my family, I finished the PhD program in two and one-half years, and started a scientific part of my career.

At present, I try to do both scientific data analysis, and engineering tasks that I didn't want to totally abandon.

In the scientific part of my work, I now predominantly analyze recordings from ground-based stations dedicated for broadband electromagnetic-field measurements of lightning-related signals. I also analyze other lightning-generated signals, such as whistlers, in data recorded by electromagnetic-wave receivers placed onboard Earth-orbiting spacecraft missions. Finally, I recently had an opportunity to analyze electromagnetic-wave records obtained during close approaches of the Juno spacecraft to the planet Jupiter. I have visually inspected more than 100,000 spectrograms. This resulted in a dataset of more than 2000 lightning whistlers, the largest collection of Jovian lightning-related signals up to now.

My engineering work now mainly includes so-called "product assurance and quality assurance activities," connected with the development of our instrumentation for the future spacecraft missions to Jupiter (JUICE/ESA), Mars (ExoMars2020/ESA-Roskosmos), and toward the sun (Solar Orbiter/ESA).

Conclusion and Take-Away Message

I have never regretted my decision to study radio electronics and to join the team developing spacecraft instrumentation. I enjoyed studying and working in a primarily male environment. I have never had particular problems with this environment, and I don't really feel the need for somebody spending time on dissecting gender issues on my behalf. I also feel that positive discrimination of females might have counterproductive effects. I don't want to be selected nor unselected for a job because of gender. Consequently, I do not see any need for a special column for female radio scientists in this magazine. My suggestion therefore would be to open this column to any radio scientist, female or male, who, in a weak moment, agrees to describe their careers.

Figure 1. Ivana Kolmašová





INTERNATIONAL SYMPOSIUM ON ELECTROMAGNETIC THEORY (EMTS 2019)

May 27-31, 2019, San Diego, CA, USA

First Call For Papers

The International Symposium on Electromagnetic Theory (EMTS 2019) will be held May 27-31, 2019, in San Diego, CA, USA. It is organized by Commission B (Fields and Waves) of the International Union of Radio Science (URSI), and is financially cosponsored by the United States National Committee for URSI (USNC-URSI) and the IEEE Antennas and Propagation Society (IEEE AP-S). EMTS 2019 is the 23rd event in the triennial series of international EMT symposia, which has a long history since 1953. Its scope covers all areas of electromagnetic theory and its applications. It is the major scientific event of Commission B, along with the URSI General Assembly and Scientific Symposium, Atlantic Radio Science Conference (AT-RASC), and Asia Pacific Radio Science Conference (AP-RASC). The venue is the hotel Westin San Diego, which is minutes from downtown activities including the San Diego Zoo, Balboa Park and its numerous museums, and the Gaslamp district for dining and nightlife. San Diego is the eighth largest city in USA, and is often referred to as "America's Finest City." Known for its great hotels, beautiful weather, pristine beaches, friendly people, and a plethora of entertainment, San Diego is a favorite destination for visitors across the globe. The San Diego airport is conveniently close to our symposium venue, so transportation to the conference will be quick and easy.

Welcome to San Diego in May 2019! The conference will offer plenary talks by distinguished speakers, regular oral and poster sessions, and a one-day school for young scientists (May 27), focusing on a topic in electromagnetics. A number of Young Scientist Awards will be offered, covering the registration fee and accommodation during the conference. In addition, business meetings, receptions, and a conference banquet will be organized. EMTS 2019 will focus on electromagnetic fields and their applications. Contributions on any aspect of the scope of Commission B are solicited. Some suggested topics are listed below. Special-session topics will be listed later on the Web site. All submissions (two to four pages in IEEE two-column format) will be reviewed by the Commission B Technical Advisory Board. Accepted and presented papers may be submitted to IEEE Xplore.

Important dates

- Paper submission site opens: July 15, 2018
- Deadline for paper submission: **October 22, 2018**
- Notification of acceptance: January 10, 2019
- Early-bird and author registration ends: March 30, 2019

Contact: Technical Program: Kazuya Kobayashi <kazuya@tamacc.chuo-u.ac.jp>
Local Organizing Committee: Sembiam Rengarajan <srengarajan@csun.edu>

Suggested Topics

1. Electromagnetic theory

- Analytical and semi-analytical methods
- Mathematical modeling
- Canonical problems
- Scattering and diffraction
- Inverse scattering and imaging

2. Computational methods

- Integral equation methods
- Partial differential equation methods
- High-frequency and hybrid methods
- Fast solvers and high-order methods
- Time-domain techniques
- Computational algorithms

3. Materials and wave-material interaction

- Metamaterials and metasurfaces
- Plasmonics and nanoelectromagnetics
- Electromagnetic bandgaps and other periodic structures

- Optical devices
- EMC and EMI
- Bioelectromagnetics

4. Antennas and propagation

- Antenna theory
- Antenna measurements
- Multi-band and wideband antennas
- Antenna arrays and MIMOs
- Wireless communication systems
- Guided waves and structures
- Random media and rough surfaces
- Millimeter wave/5G propagation
- Millimeter-wave antennas
- MIMO for 5G communication

5. Other topics

- History of electromagnetics
- Education in electromagnetics

www.emts2019.org

March 2018

Gi4DM 2018

Kyrenia, Turkish Republic of Northern Cyprus, 14-18 March 2018

Contact: K2 Conference and Event Management Kosuyolu Mh. Ali Nazime Sk. No: 45 Kosuyolu 34718 Kadikoy / Istanbul Phone: +90 (216) 428 95 51 - Fax: +90 (216) 428 95 91 E-mail: gi4dm@k2-events.com, <http://www.gi4dm2018.org>

8th VERSIM Workshop

Apatity, Russia, 19-23 March 2018

Contact: Dr. Andrei Demekhov andrei@appl.sci-nnov.ru
http://www.iugg.org/IAGA/iaga_ursi/versim/

Geolocation and navigation in space and time

The URSI-France 2018 Workshop

Paris, France, 28-29 March 2018

Contact: <http://ursi-france.org/>

May 2018

Baltic URSI Symposium (part of Microwave Week 2018)

Poznan, Poland, 14-16 May 2018

Contact: Prof. Dr. Andrzej Napieralski, Baltic URSI Symposium 2018 Chairman & Dr Przemyslaw Sekalski,
<http://mrw2018.org/ursi2018/national-ursi-2018-topics/>

AT-RASC 2018

Second URSI Atlantic Radio Science Conference

Gran Canaria, Spain, 28 May – 1 June 2018

Contact: Prof. Peter Van Daele, URSI Secretariat, Ghent University – INTEC, Technologiepark-Zwijnaarde 15, B-9052 Gent, Belgium, Fax: +32 9-264 4288, E-mail address: E-mail: peter.vandaele@ugent.be, <http://www.at-rasc.com>

July 2018

COSPAR 2018

42nd Scientific Assembly of the Committee on Space Research (COSPAR) and Associated Events

Pasadena, CA, USA, 14 - 22 July 2018

Contact: COSPAR Secretariat (cospar@cosparhq.cnes.fr)
<http://www.cospar-assembly.org>

August 2018

Metamaterials 2018

12th International Congress on Artificial Materials for Novel Wave Phenomena

Espoo, Finland, 27-30 August 2018

Contact: <http://congress2018.metamorphose-vi.org>

September 2018

ICEAA 2018 - IEEE APWC 2018 - FEM 2018

Cartagena de Indias, Colombia

Contact: iceaa18@iceaa.polito.it, <http://www.iceaa-offshore.org>

October 2018

COMPENG

2018 IEEE Workshop on Complexity in Engineering

Florence, Italy, 10-12 October 2018

Contact: compeng2018@ino.cnr.it, <http://compeng2018.ieeesezioneitalia.it/>

RADIO 2018

IEEE Radio and Antenna Days of the Indian Ocean 2018

Mauritius, 15-18 October 2018

Contact: <http://www.radiosociety.org/radio2018/>

ISAP 2018

2018 International Symposium on Antennas and Propagation

Busan, Korea, 23-26 October 2018

Contact: <http://isap2018.org/>

November 2018

APMC

Asia-Pacific Microwave Conference 2018

Kyoto, Japan, 6-9 November 2018

Contact: <http://www.apmc2018.org/>

LAPC 2018

Loughborough Antennas and Propagation Conference

Loughborough, United Kingdom, 12-13 November 2018

Contact: Poppy Seamarks, Tel: +44 (0)1438 767 304,

Fax: +44 (0)1438 765 659, Email: lapc@theiet.org

<https://events.theiet.org/lapc/>

January 2019

USNC-URSI NRSM 2019

USNC-URSI National Radio Science Meeting

Boulder, CO, USA, 9-12 January 2019

Contact: Dr. Sembiam R. Rengarajan, Department of ECE, California State University, Northridge, CA 91330-8346, USA, Fax: 818-677-7062, E-mail: srengarajan@csun.edu; Logistics: Christina Patarino, E-mail: christina.patarino@colorado.edu, Fax: 303-492-5959, <https://nrsmboulder.org/>

March 2019

C&RS “Smarter World”

18th Research Colloquium on Radio Science and Communications for a Smarter World

Dublin, Ireland, 8-9 March 2019

Contact: Dr. C. Brennan (Organising Cttee Chair)

[http://www.ursi2016.org/content/meetings/mc/Ireland-2017-CRS Smarter World CFP.pdf](http://www.ursi2016.org/content/meetings/mc/Ireland-2017-CRS_Smarter_World_CFP.pdf)

AP-RASC 2019

2019 URSI Asia-Pacific Radio Science Conference

New Delhi, India, 9-15 March 2019

Contact: Prof. Amitava Sen Gupta, E-mail: sengupto53@yahoo.com, <http://aprasc2019.com>

May 2019

EMTS 2019

2019 URSI Commission B International Symposium on Electromagnetic Theory

San Diego, CA, USA, 27-31 May 2019

Contact: Prof. Sembiam R. Rengarajan, California State University, Northridge, CA, USA, Fax +1 818 677 7062, E-mail: srengarajan@csun.edu, <http://www.emts2019.org>

November 2019

COSPAR 2019

4th Symposium of the Committee on Space Research (COSPAR): Small Satellites for Sustainable Science and Development

Herzliya, Israel, 4-8 November 2019

Contact : COSPAR Secretariat, 2 place Maurice Quentin, 75039 Paris Cedex 01, France, Tel: +33 1 44 76 75 10, Fax: +33 1 44 76 74 37, E-mail: cospar@cosparhq.cnes.fr <http://www.cospar2019.org>

August 2020

COSPAR 2020

43rd Scientific Assembly of the Committee on Space Research (COSPAR) and Associated Events

Sydney, Australia, 15-23 August 2020

Contact : COSPAR Secretariat, 2 place Maurice Quentin, 75039 Paris Cedex 01, France, Tel: +33 1 44 76 75 10, Fax: +33 1 44 76 74 37, E-mail: cospar@cosparhq.cnes.fr <http://www.cospar2020.org>

URSI GASS 2020

Rome, Italy, 29 August - 5 September 2020

Contact: URSI Secretariat, c/o INTEC, Tech Lane Ghent Science Park - Campus A, Technologiepark-Zwijnaarde 15, B-9052 Gent, Belgium, E-mail gass@ursi.org, <http://www.ursi2020.org>

May 2021

AT-RASC 2021

Third URSI Atlantic Radio Science Conference

Gran Canaria, Spain, 23-28 May 2021

Contact: Prof. Peter Van Daele, URSI Secretariat, Ghent University – INTEC, Technologiepark-Zwijnaarde 15, B-9052 Gent, Belgium, Fax: +32 9-264 4288, E-mail: peter.vandaele@ugent.be, <http://www.at-rasc.com>

A detailed list of meetings is available on the URSI website at <http://www.ursi.org/events.php>

URSI cannot be held responsible for any errors contained in this list of meetings

Information for Authors

Content

The *Radio Science Bulletin* is published four times per year by the Radio Science Press on behalf of URSI, the International Union of Radio Science. The content of the *Bulletin* falls into three categories: peer-reviewed scientific papers, correspondence items (short technical notes, letters to the editor, reports on meetings, and reviews), and general and administrative information issued by the URSI Secretariat. Scientific papers may be invited (such as papers in the *Reviews of Radio Science* series, from the Commissions of URSI) or contributed. Papers may include original contributions, but should preferably also be of a sufficiently tutorial or review nature to be of interest to a wide range of radio scientists. The *Radio Science Bulletin* is indexed and abstracted by INSPEC.

Scientific papers are subjected to peer review. The content should be original and should not duplicate information or material that has been previously published (if use is made of previously published material, this must be identified to the Editor at the time of submission). Submission of a manuscript constitutes an implicit statement by the author(s) that it has not been submitted, accepted for publication, published, or copyrighted elsewhere, unless stated differently by the author(s) at time of submission. Accepted material will not be returned unless requested by the author(s) at time of submission.

Submissions

Material submitted for publication in the scientific section of the *Bulletin* should be addressed to the Editor, whereas administrative material is handled directly with the Secretariat. Submission in electronic format according to the instructions below is preferred. There are typically no page charges for contributions following the guidelines. No free reprints are provided.

Style and Format

There are no set limits on the length of papers, but they typically range from three to 15 published pages including figures. The official languages of URSI are French and English: contributions in either language are acceptable. No specific style for the manuscript is required as the final layout of the material is done by the URSI Secretariat. Manuscripts should generally be prepared in one column for printing on one side of the paper, with as little use of automatic formatting features of word processors as possible. A complete style guide for the *Reviews of Radio Science* can be downloaded from <http://www.ips.gov.au/IPSHosted/NCRS/reviews/>. The style instructions in this can be followed for all other *Bulletin* contributions, as well. The name, affiliation, address, telephone and fax numbers, and e-mail address for all authors must be included with

All papers accepted for publication are subject to editing to provide uniformity of style and clarity of language. The publication schedule does not usually permit providing galleys to the author.

Figure captions should be on a separate page in proper style; see the above guide or any issue for examples. All lettering on figures must be of sufficient size to be at least 9 pt in size after reduction to column width. Each illustration should be identified on the back or at the bottom of the sheet with the figure number and name of author(s). If possible, the figures should also be provided in electronic format. TIF is preferred, although other formats are possible as well: please contact the Editor. Electronic versions of figures *must* be of sufficient resolution to permit good quality in print. As a rough guideline, when sized to column width, line art should have a minimum resolution of 300 dpi; color photographs should have a minimum resolution of 150 dpi with a color depth of 24 bits. 72 dpi images intended for the Web are generally *not* acceptable. Contact the Editor for further information.

Electronic Submission

A version of Microsoft *Word* is the preferred format for submissions. Submissions in versions of T_EX can be accepted in some circumstances: please contact the Editor before submitting. *A paper copy of all electronic submissions must be mailed to the Editor, including originals of all figures.* Please do *not* include figures in the same file as the text of a contribution. Electronic files can be sent to the Editor in three ways: (1) By sending a floppy diskette or CD-R; (2) By attachment to an e-mail message to the Editor (the maximum size for attachments *after* MIME encoding is about 7 MB); (3) By e-mailing the Editor instructions for downloading the material from an ftp site.

Review Process

The review process usually requires about three months. Authors may be asked to modify the manuscript if it is not accepted in its original form. The elapsed time between receipt of a manuscript and publication is usually less than twelve months.

Copyright

Submission of a contribution to the *Radio Science Bulletin* will be interpreted as assignment and release of copyright and any and all other rights to the Radio Science Press, acting as agent and trustee for URSI. Submission for publication implicitly indicates the author(s) agreement with such assignment, and certification that publication will not violate any other copyrights or other rights associated with the submitted material.

Become An Individual Member of URSI

The URSI Board of Officers is pleased to announce the establishment of Individual Fellowship (FURSI), Individual Membership (MURSI), and Individual Associate Membership (AMURSI). By joining URSI, Individual Associate Members, Individual Members, and Fellows secure recognition with their peers, are better connected to URSI Headquarters, and are better connected to their National Committees. Each can then better provide support to the other. Other benefits include discounted registration fees at URSI conferences (beginning with the 2018 URSI AT RASC) and at some conferences cosponsored by URSI (beginning with some conferences run by IEEE AP-S), a certificate of membership, and e-mail notification of the availability of the electronic edition of the URSI *Radio Science Bulletin*.

Fellowship is by invitation only. Membership and Associate Membership can be applied for through the online forms available at www.ursi.org/membership.php, or at www.ursi.org